Processes and records of coastal sediment dispersal in contrasting deltaic systems

Emily F. Eidam

A dissertation
submitted in partial fulfillment of the
requirements for the degree of

Doctor of Philosophy

University of Washington

2017

Reading Committee:

Andrea S. Ogston, Chair

Charles A. Nittrouer, Chair

Jonathan A. Warrick

Program Authorized to Offer Degree:
School of Oceanography

University of Washington

Abstract

Processes and records of coastal sediment dispersal in contrasting deltaic systems

Emily F. Eidam

Co-Chairs of the Supervisory Committee:
Professor Andrea S. Ogston
Oceanography

Professor Charles A. Nittrouer
Oceanography

Rivers are responsible for most sediment delivery to the ocean, and at the river-ocean transition, a complex set of processes and pathways shape the ultimate fate of particulates. Conceptual and numerical models of fluvial-marine dispersal have become increasingly sophisticated through several decades of observational and modeling studies. However, many key processes remain poorly constrained, such as particle clearance from river plumes and episodic sediment-gravity flows, and connections between these types of discrete processes to subaqueous-delta evolution. This study investigates sediment-dispersal processes and their products in two deltaic systems: the small mountainous Elwha River delta (Washington State), and the large Mekong River delta (Vietnam).

Sediment clearance from buoyant river plumes is complicated by flocculation dynamics, which remain difficult to quantify. One option for characterizing sediment-clearance rates is estimation of an "effective settling velocity" (w_e), i.e., a single settling velocity which describes the clearance rate of all flocculated and unflocculated sediment in a plume. This study tests the validity and key assumptions of a published 1D clearance model for w_e using measurements from the small Elwha River plume during and after a dam removal project. The difference between effective settling velocity (w_e) and total effective settling velocity ($w_{e'}$)

is also explored, based on previous studies suggesting that $w_{e'}$ is the sum of w_e (representing gravitational settling) and an additional term representing enhanced removal at the base of a plume.

Four variations of the 1D clearance model are applied, using both point and depth-integrated measurements of suspended sediment concentrations, as well as estimated and modeled plume-water residence times. For depth-integrated measurements and modeled residence times, $w_{e'}$ are ∼0.13–3.5 mm/s, and are greater than w_e values obtained from point measurements (∼0.041–0.33 mm/s). The depth-integrated results are interpreted to be a reasonable approximation of $w_{e'}$ based on measured grain-size distributions and the scale of the plume. The differences between $w_{e'}$ and w_e are attributed to concentration gradients and turbulence-induced removal of sediment at the base of the plume within a few kilometers of the river.

During extreme sediment-loading events, near-bed sediment-gravity flows may dominate dispersal pathways, rather than buoyant surface plumes. These events occur episodically, and thus their mechanics are not well-constrained due to sparse in situ measurements. Instruments deployed near the Elwha River mouth for ∼3.5 y during dam removal recorded a gravity flow associated with a river flood. The event lasted ∼10 h and resulted in rapid deposition of >15 cm of sand within a few hundred meters of the mouth, and was interpreted to be a hyperpycnal plume or hyperpycnal flow. After a few hours, the flow deteriorated through rapid deposition of sand and vertical mixing of muddy water. The extinction dynamics were characteristic of a hydraulic jump and lofting plume at the base of the steep delta front, resulting in a neutrally buoyant plume filling most of the water column. The muddy-sand deposit was entirely eroded within three weeks, leaving little record of the event. The sandy composition, short runout distance, and rapid extinction of the gravity flow highlight the challenges to forming and maintaining hyperpycnal flows. Post-event erosion of the deposit suggests that in similarly energetic environments, such events may be under-represented in

the stratigraphic record.

In contrasting large-river systems, sediment dispersal processes tend to be modulated by seasonal shifts in river discharge and ocean energy, rather than by storms and other extreme events. These seasonal processes coupled with abundant sediment supply generate subaqueous deltas near many of the world's largest rivers. The geometry of these subaqueous deposits is generally controlled by wave and current energy, which produce a topset-foreset transition (or "rollover point" between zones of moderate and rapid accumulation) at 25–40-m water depth. Instrument measurements, cores, and a simplistic wave model are used to evaluate morphodynamics of the subaqueous Mekong Delta, which has an unusually shallow rollover at 4–6 m depth. Results suggest that the foreset experiences rapid accumulation and exhibits internal structures characteristic of many subaqueous deltas. However, based on the wave model, the foreset is not energy-limited and does not exhibit a classic subaqueous-delta-front stress refuge. During the high-discharge season, sediment is delivered to the topset and foreset, but further seaward dispersal is limited by landward return flow under the plume and regional circulation patterns. During the windy monsoon season, landward currents driven by regional circulation (at greater depths) and by winds (at shallow depths) serve to retain sediment near shore. Thus, persistent landward sediment fluxes in both seasons likely help shape the subaqueous delta, allowing a shallow topset to exist, despite sufficient transport energy to erode muds and fine sands during much of the year. These results highlight the importance of considering both transport energy and transport direction (leading to sediment convergence) when interpreting the evolution of large subaqueous deltas.

TABLE OF CONTENTS

LIST OF FIGURES

LIST OF TABLES

ACKNOWLEDGMENTS

This work would not have been possible without the patience, support, and generosity of my two wonderful advisors, Andrea Ogston and Chuck Nittrouer. I can't thank them enough for providing constant opportunities to be engaged in every stage of the research process, from proposals to publications. Their dedication to science, education, and collaboration set an excellent example and was an inspiration to continue exploring our dynamic coasts.

I also thank the members of the UW Sediment Dynamics lab for their tireless field support: Aaron Fricke, Dan Nowacki, Rip Hale, Kristen Lee Webster, Katie Boldt, Daniel Culling, Hannah Glover, and Robin Banner. Special thanks go to Aaron for providing a wealth of programming advice, and Kristen and Daniel for being great office mates.

The Elwha fieldwork was made possible by the R/V Barnes crew, including Ray McQuin, Bob Goodman, Ken Pinnell, whose dedication to field efforts was greatly appreciated. Dave Thoreson, Randy Fabro, and Tor Bjorklund also provided great shop assistance.

I also thank the talented undergraduate research apprentices from the Friday Harbor classes, whose contagious enthusiasm was the highlight of the Elwha Delta project and motivation to pursue a career involving teaching. Additional thanks go to Brianna Sweeney, Kevin Simans, Jenny Renee, Morgan Mackaay, Ben Reynolds, Liz Ewings, and Caity Fisher for their help processing samples.

Many colleagues generously supported the Elwha and Mekong research efforts with their time and wisdom, including Ian Miller, Steve Rubin, Jon Warrick, Andrew Stevens, Rich Nguyen, Dave DeMaster, Paul Liu, Jennifer Glass, Deb Nittrouer, and Thanh Nguyen. This research would not have been possible without them. I also appreciate Jon Warrick, Jim Thomson, and Steve Emerson for lending guidance as committee members.

Finally, I appreciate my family's constant encouragement, and writing breaks to the mountains and city with friends Marie Salmi and Katie Dobkowski.

Chapter 1
INTRODUCTION

Rivers are the exchange agent between land and sea, and transport eroded fragments of continents to marine sinks. At the coast, sediments take diverse pathways through the water column to proximal or distal sinks. Pathways are determined by characteristics of particle settling, ambient currents, wave energy, bathymetry, and coastal morphology, and can be as simple as vertical settling from a plume to the bed, or as complex as wave-supported fluid muds formed on the shelf weeks after initial delivery. While several decades of intensive observational studies and complex modeling efforts have transformed our understanding of these coastal dispersal systems, much remains to learned, for example, about the mechanics of particle settling, environmental controls on episodic sediment-delivery events, and even the morphodynamics of some of the largest subaqueous deltas. By advancing conceptual models of particle dynamics, dispersal process, and morphologic feedbacks, quantitative models of coastal dynamics can be improved to better serve communities and ecosystems.

1.1 Quantification of particle clearance from surface plumes

In many coastal dispersal systems, the first point of entry for fluvial sediment is a buoyant surface plume (Wright, 1977). The rate of sediment export from a plume can significantly impact the location of sediment deposition on the seabed (e.g., Milligan et al., 2007), as well as impact water-quality parameters such as light and nutrient availability (e.g., Dagg et al., 2004). Export rates—or clearance rates—from plumes are variable among systems, and even within systems. Discrete particles settle at different speeds dictated by their mass and diameter as well as fluid properties, and flocs, i.e., aggregates of single grains and sometimes organic matter, settle according to a far more complex set of parameters (e.g., Winterwerp,

2002) that have yet to be fully understood. When fine-grained sediments are included in coastal hydrodynamic models, settling velocities are typically represented by a few values or a single value (commonly 1 mm/s), in the absence of detailed field measurements or well-parameterized settling velocities for diverse environments.

Recently, a few observational studies have proposed characterizing an "effective settling velocity" (w_e) for a plume using a 1D or 2D clearance model. This effective settling velocity represents the mean clearance rate of all particles, including flocs and single grains. This approach has been applied successfully to a few plumes from both large and small rivers, as well as an estuary (e.g., Hill et al., 2000; van Maren and Hoekstra, 2005; Nowacki et al., 2012; Shi and Zhou, 2004). Because it requires relatively simple measurements, it offers an attractive means of characterizing sediment clearance within a given system, in lieu of assuming a single or a few representative settling velocities for modeling efforts. However, it has not been widely validated in diverse environments, nor well tested in the nearfield zone of highly dynamic, small-scale plumes. Plumes emanating from small mountainous rivers (SMRs) are an important stage in sediment delivery; many SMRs discharge the majority of their annual sediment load during a few discrete storm events (Milliman and Meade, 1983), leading to rapid sediment export through buoyant surface plumes, and even the formation of negatively buoyant sediment-gravity flows.

In Chapter 2, a simple 1D model proposed by Hill et al. (2000) is applied to measurements from the Elwha River plume, in a tidal strait in Washington State. The Elwha River offers a good case study in small-scale plume dynamics and rapid sediment export, because the plume is tidally forced (Warrick and Stevens, 2011) and has been the initial stage of dispersal for several million tonnes of fine-grained sediment during a multi-year dam removal project (e.g., Warrick et al., 2015). Profiles of salinity and suspended-sediment concentrations (SSCs), together with simple velocity estimates and modeled residence times, are used to test assumptions implicit to the 1D clearance model and evaluate magnitudes of w_e for this very dynamic, small-scale system.

1.2 Hydrodynamics and sediment transport in a coarse-grained hyperpycnal flow

During extreme fluvial sediment-loading events, river water may become denser than seawater, and form a plunging negatively buoyant (or "hyperpycnal") plume (e.g., Bates, 1953; Geyer et al., 2004). Though episodic and difficult to predict, these events are considered to be important mechanisms of cross-shelf sediment transfer. They can carry large amounts of sediment great distances, and in some environments, deliver a record of terrestrial events to mid-shelf flood deposits.

Because hyperpycnal plumes occur sporadically, in situ observations are sparse and their mechanics in diverse natural systems are not fully understood. During the removal of two dams on the Elwha River from 2011 to 2014, fluvial erosion of reservoir sediments frequently generated SSCs of >5 g/L (USGS, 2017). One to two instrumented tripods were deployed for more than three years near the river mouth, and recorded a gravity-flow event in Mar 2014, as discussed in Chapter 3. This event deposited >15 cm of muddy sand within a few hundred meters of the river mouth. Acoustic and optical measurements of boundary-layer hydrodynamics and sediment transport are used to evaluate hydrodynamics and sediment transport during the event. The results lend insight into the duration, extinction mechanisms, and sediment-carrying capacities of hyperpycnal flows, especially those comprising abundant sand. The subsequent rapid erosion of the event deposit highlights the competency of tidal currents to erase even coarse-grained records of terrestrial delivery events.

1.3 Sediment dispersal processes and morphodynamic feedbacks of a large-scale delta

In contrast to small-river dispersal systems where rapid plume clearance and hyperpycnal flows are key transport processes (especially during floods), large-river dispersal systems generate broad, low-concentration surface plumes and large muddy deltas under the influence of seasonal (rather than storm-induced) fluctuations in fluvial sediment supply and ocean energy. These large deltaic systems are often classified as fluvial-, wave-, or tide-dominated,

and many form large subaqueous deltas (e.g., Goodbred and Saito, 2011). These subaqueous deltas are characterized by sigmoidal-shaped sediment packages (or "clinoforms") comprising a gently sloping "topset" and steeply sloping "foreset." The geometry is thought to be dictated by waves and currents: sediments are mobilized and transported across the topset, which lies above the "fairweather wave-current base," and then deposited on the deeper, lower-energy foreset, a "stress refuge." For many large-river deltas, the topset-foreset transition (or "rollover point") lies at 25–40 m water depth, owing to regional wave climates and current patterns (e.g., Walsh et al., 2004).

The subaqueous Mekong River delta is relatively unique among modern, active large-river deltas in that the rollover point lies at ∼4-6 m water depth, despite the influence of an energetic, seasonal windy monsoon. The sediment-dispersal processes responsible for this morphology are not well understood. In Chapter 4, the results of two surveys conducted on the Mekong Delta in September 2014 and March 2015 are used to evaluate sediment transport processes and century-scale deposits, in order to begin unraveling the morphodynamics of the subaqueous-delta clinoform. Measurements from an instrumented tripod system, a ship-based acoustic velocity sensor, and water-column profiles are analyzed for seasonal variations in sediment flux patterns. Accumulation rates and sediment-texture variations determined from gravity cores are also used to fit the dynamical measurements into a longer-timescale context. Finally, simplistic modeling of wave energy is used to evaluate annual trends in transport energy in the absence of long time-series measurements. Results suggest that the Mekong dispersal system is not energy-limited, but rather strongly influenced by transport directions, and resulting flux convergence. Directionality in this system is controlled by patterns of river discharge, regional currents, and wind-driven currents that change throughout the year. The results highlight the importance of considering both magnitude and direction of transport energy when interpreting present and past delta morphodynamics.

Chapter 2

SEDIMENT CLEARANCE RATES FROM A SMALL TIDALLY FORCED RIVER PLUME [1]

2.1 Introduction

River-borne sediment typically enters the coastal ocean in surface plumes (Wright, 1977). This sediment generally comprises fine-grained silts and clays (<63 μm), which readily aggregate into fast-settling microflocs and macroflocs via chemical and biological processes (Gibbs, 1985; Eisma, 1986, 1993). Mixed populations of single grains and flocs then settle from plumes into subsurface dispersal systems, at rates determined by floc mass, density, shape, and other properties (van Leussen, 1988; Burban et al., 1989; Winterwerp, 2002).

Plume-transported sediment impacts coastal light attenuation, nutrient delivery, and productivity, and eventually settles and becomes incorporated into seabed deposits (Dagg et al., 2004; Geyer et al., 2004). Measurements and predictions of plume-sediment clearance rates allow for better characterizations of coastal habitat impacts and the location of seabed deposits. Estimates of clearance rates are confounded by aggregation processes, however. Floc properties vary widely among and within environments, flocs are fragile and difficult to sample, and flocs formed in laboratory studies do not always exhibit the same properties as those formed in situ (e.g., Khelifa and Hill, 2006; Mantovanelli and Ridd, 2006; Curran et al., 2003). Ideally, sediment clearance rates would be calculated from measured parameters like floc settling velocities, floc fractions (the mass fraction of plume sediment contained in flocs), and mass distributions of single grains. But despite decades of investigations and an extensive body of literature on flocculation dynamics, many uncertainties remain about the

[1] This chapter is formatted for journal submission as: Eidam, E.F., Ogston, A.S., Stevens, A.W., Warrick, J.A., and Nittrouer, C.A., Sediment clearance rates from a small tidally forced river plume.

best observational tools and parameterizations for flocs, given their diverse forms and fragile structures (e.g., Mantovanelli and Ridd, 2006).

In order to quantify and model sediment clearance patterns despite the complications imposed by flocs, some studies have proposed estimating an effective settling velocity. This parameter, w_e, is a single speed which describes the removal of all particles from a suspension, including flocs and single grains of different sizes (e.g., Hill et al., 2000; Curran et al., 2002; Nowacki et al., 2012). In practice, w_e has been calculated using a simple 1D clearance model based on salinity and suspended-sediment profiles (and an estimate of plume speed; e.g., Hill et al., 2000), or from a control-volume method based on salinity, suspended-sediment, velocity, and turbulence profiles (e.g., Nowacki et al., 2012).

Based on these studies, w_e is a promising parameterization of plume clearance; however, it has not been widely validated for diverse systems, and uncertainties remain about the best calculation approach. Hill et al. (2000) applied the 1D clearance model to point measurements of salinity and SSC from the Eel River plume, at distances up to 30 km from the mouth, during floods. Calculated w_e values were $\sim$0.1 mm/s, less than the nominal 1 mm/s settling velocity expected for flocs (w_f). This discrepancy was assumed to be the result of a partially flocculated suspension, i.e., a mixture of fast-settling flocs and slow-settling single grains. Similar w_e values of 0.07-0.14 mm/s were obtained for the Herbert River plume (Australia) at distances of 2-12 km from shore (Wu et al., 2006). It should be noted that in the 1D method, plume properties are sampled at a single depth within the plume, based on the assumption of a well-mixed plume.

Nowacki et al. (2012) applied an alternative control-volume method to profile measurements from the Columbia River plume, at distances of 4–10 km from the mouth, and found w_e values of $\sim$4–10 mm/s—i.e., larger than those found from 1D-model case studies and commonly cited w_f values. Their results were generally interpreted to represent gravitational settling and turbulence-induced removal at the base of the plume. Rouhnia and Strom (2017) evaluated w_e using a flume study; like Nowacki et al. (2012), they found $w_e > w_f$, and concluded that the total effective settling velocities (herein denoted $w_{e'}$ comprised gravitational

and turbulence components. The contribution of turbulence-induced removal at the plume base could be overlooked by the simpler 1D method, wherein measurements are collected at a single depth, and gradients in SSC plus removal processes at the base of the plume are neglected.

In field studies by Hill et al. (2000), Wu et al. (2006), and Nowacki et al. (2012), w_e (or $w_{e'}$) was estimated >2 km from the river mouth. Quantifying and predicting w_e at these distances is useful, since large plumes can provide broad zones of elevated productivity at their frontal boundaries and disperse sediment over great distances (e.g., Dagg et al., 2004; Lohrenz et al., 1999). Quantifying clearance rates for the nearfield zone of small-scale plumes (e.g., <2 km from the mouth) is also also useful, especially for plumes emanating from high-yield, small mountainous rivers (SMRs). Many SMRs deliver the majority of their annual sediment load during a few discrete storm events (Milliman and Meade, 1983), and plumes from SMRs like the Santa Clara River (CA) and Elwha River (WA) can lose the majority of their sediment within ∼1 km of the river mouth (Warrick et al., 2004; Warrick and Stevens, 2011). During extreme sediment loading events, it is also thought that rapid sedimentation from these types of small-river plumes may lead to the formation of hyperpycnal flows (e.g., Parsons et al., 2001). Thus, extending studies of w_e to the nearfield zones of very dynamic, small-scale plumes may aid models of coastal sedimentation during small-river flood events.

In order to test the effectiveness of the 1D clearance model, which is the more logistically feasible of the two methods noted above, measurements were collected from the Elwha River plume between 2012 and 2016. The Elwha River was the site of a major dam removal project from 2011 to 2014, and experienced elevated sediment loads for several years (Magirl et al., 2015). Thus, the system offered strong signals of sediment clearance (i.e., a high-concentration plume with small spatial scale), especially during rain and snowmelt events. Seven plume surveys were conducted during moderate to high wintertime river discharges, and measurements were used to evaluate w_e and $w_{e'}$. Primary goals were to:

1. Evaluate w_e using the original formulation of the 1D clearance model given in Hill et

al. (2000) for comparison of Eel River and Elwha River values;

2. Evaluate $w_{e'}$ using depth-integrated plume concentrations, similar to the Nowacki et al. (2012) method but in a simplified 1-D reference frame, in order to test assumptions about plume mixing implicit to the 1D model;

3. Test the 1D clearance model using travel times based on plume speed and distance, as well as modeled travel times, to evalute its efficacy in small plumes with complex streamlines; and

4. Evaluate possible environmental controls on $w_{e'}$ by comparing values from different surveys to parameters like river discharge and wind speed.

Results suggest that the 1D model is a useful characterization of effective settling velocities. Calculations must be approached with care, however, since the use of point measurements versus depth-integrated measurements yield different estimates of effective settling velocities (i.e., w_e versus $w_{e'}$). These results serve to validate use of the 1D model, and offer insights for obtaining reliable results.

2.2 Regional setting

The Elwha River is a 72-km-long small mountainous river in Washington State, USA (Figure 2.1) with mean annual discharge of ∼40 m^3/s at USGS site 12045500 (Curran et al., 2009). Typical winter and spring discharge peaks can reach ∼200–300 m^3/s due to rainstorms and snowmelt (USGS, 2017). The river discharges from the Olympic Mountains to the Strait of Juan de Fuca, a tidal strait where semi-diurnal peak currents can exceed 1 m/s (Fissel and Huggett, 1976; Eidam et al., 2016). Transient eddies form east and west of the river mouth according to the tidal phase (Gelfenbaum et al., 2009; Warrick and Stevens, 2011; Gelfenbaum et al., 2015).

During 2011–2014, two century-old hydroelectric dams at river kilometers 5.6 and 13.8 were deconstructed, exposing ∼30 million tonnes of impounded gravel, sand, silt, and clay

(Randle et al., 2015). From fall 2011 to fall 2013, >3 million tonnes of fine-grained sediments were exported by the river to the coast (Warrick et al., 2015), and fluvial SSC commonly exceeded 5 g/L (Curran et al., 2014; Magirl et al., 2015). During quarterly ship-based surveys, maximum measured plume SSCs were >1 g/L (Eidam et al., 2016), one to two orders of magnitude greater than measured baseline values (Webster, 2014).

The nearfield zone of the plume—within 1 km of the mouth—has been classified as a "small-scale" or "narrow" buoyant plume (per Garvine, 1995) with average speeds of 0.2–0.5 m/s and freshwater residence times of 0.5–1.5 h for a river discharge of 60 m^3/s (Warrick and Stevens, 2011). Strong, asymmetric tidal currents deflect the plume eastward twice as often

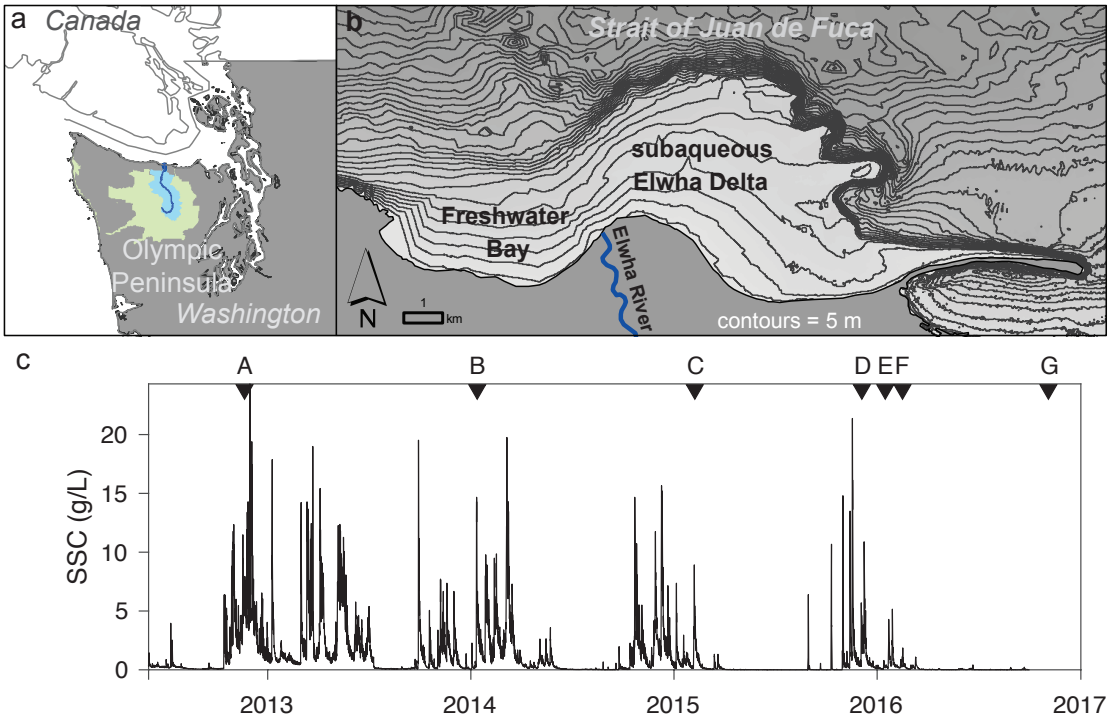

Figure 2.1: Study area and river sediment flux. a) Location of the Elwha River in the Olympic Mountains. b) Modern subaerial and relict subaqueous Elwha River deltas, bounded by Freshwater Bay to the west and a spit (Ediz Hook) to the east. c) River sediment flux (USGS, 2017) and survey times. (Bathymetry data were accessed from www.ocean.washington.edu/data/pugetsound)

as westward, and the coastal topography (Figure 2.1) influences plume dynamics. Given measured plume thicknesses of 1–3 m and a nominal assumed settling velocity of ∼1 mm/s, ≥50% of fine-grained sediment is estimated to settle from the plume within 1 km of the river mouth (Warrick and Stevens, 2011). In this study, we examine in greater detail the mechanics and patterns of sediment export within the first 1–2 km of the plume, in order to better understand how sediment is transferred and test the validity of the 1D clearance model.

2.3 Methods

2.3.1 Field measurements and lab processing

Plume transects were sampled during seven cruises (A–G) between 2012 and 2016 (Figure 2.2; Table 2.1). All cruises were conducted in winter, and five were conducted during river flows >110 m^3/s. Profiles of salinity, temperature, depth, and SSC were measured at stations spaced 70–500 m apart using one of two small conductivity, temperature, and depth (CTD) sensors with peripheral optical backscatter sensor (OBS). Surface water samples of 0.5–1.0 L were collected in conjunction with CTD/OBS measurements; samples were filtered through prepared 0.45 μm nitrocellulose filters, which were then dried, desiccated, and weighed to obtain suspended-sediment concentrations (SSCs). These surface-water SSC values were plotted against surface-water OBS measurements to obtain a linear calibration equation for each OBS (Figure 2.3). For the older OBS (used in surveys A, B, and C), a two-part calibration was obtained for high (≥ 0.1 g/L) and low (<0.1 g/L) SSCs.

Transect locations varied based on the location of the river mouth and the location of the plume during a given tidal phase (Figure 2.2c, d). The location of the river mouth changed between surveys because of the evolution of a new, coarse-grained river-mouth deposit during dam removal (see Figure 2.2a; Gelfenbaum et al., 2015). During survey G, a simple drifter (a GPS receiver in a waterproof box) was deployed at several locations during a half-hour time period to obtain estimates of plume speed.

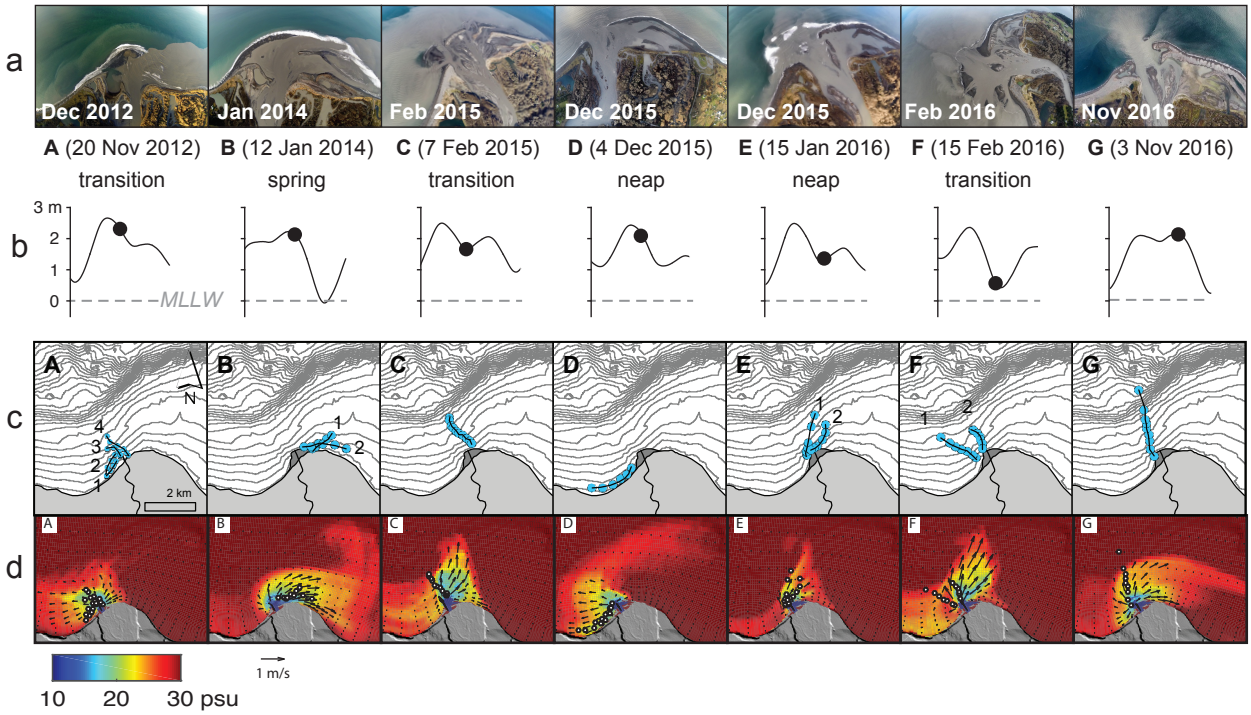

Figure 2.2: Coastal properties associated with surveys. a) Aerial photos of river-mouth locations within 1 month of each survey (Tom Roorda and CWI, www.coastalwatershedinstitute.org). b) Tidal water-level elevations for each survey day (dots denote survey times). c) Transects and station locations. d) Modeled plume salinity field during each survey.

Table 2.1: Survey parameters and environmental conditions. For CTD/OBS and grain-size measurements, Xs denote times of collection.

Table 1. Survey parameters and environmental conditions. "Mean 24-h" values were averaged from noon of the day preceding the survey to noon the day of the survey.

	A	B	C	D	E	F	G
Date	20 Nov 2012	14 Jan 2014	7 Feb 2015	4 Dec 2015	4 Jan 2016	15 Feb 2016	3 Nov 2016
Mean 24-h Q_R*	160 m^3/s	100 m^3/s	270 m^3/s	130 m^3/s	40 m^3/s	110 m^3/s	130 m^3/s
Mean 24-h SSC	6.5 g/L^+	3.8 g/L^+	5.5 g/L^+	3.5 g/L^+	0.15 g/L^+	0.50 g/L^+	0.18 g/L*
Mean wave ht	0.24-0.28 m	0.49 m	-	0.48 m	0.12-0.13 m	0.27-0.35 m	0.17 m
CTD/OBS	X	X	X	X	X	X	X
Grain-size samp.	-	X	X	-	-	-	-
Tides	Transition	Spring	Transition	Neap	Neap	Transition	Spring
Water level	Falling	High slack	Falling	Falling	Low slack	Low slack	High slack

* USGS, 2017

$^+$ Provisional USGS data from C. Magirl, personal communication

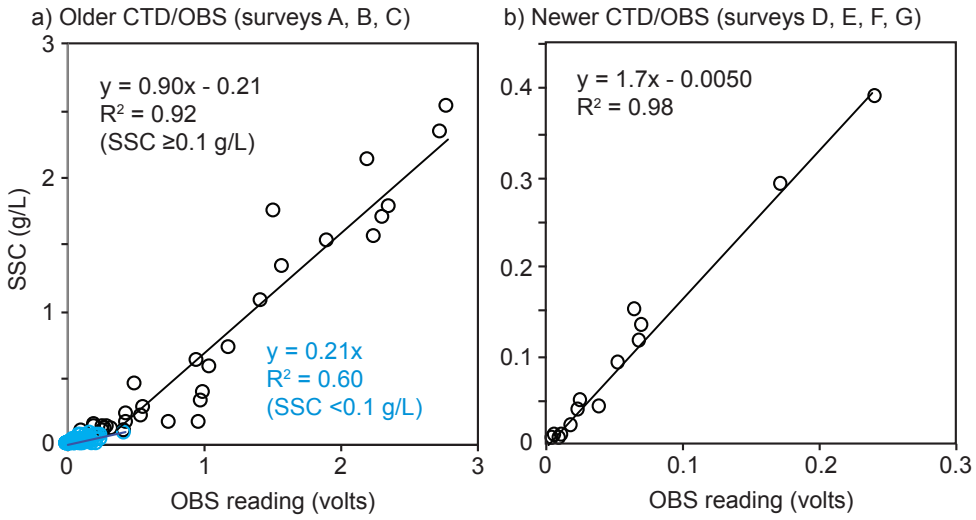

Figure 2.3: OBS calibration data. a) Calibration for older OBS/CTD package; calibration equations were determined for low (<0.1 g/L) and high (≥ 0.1 g/L) concentrations. b) Calibration for newer OBS/CTD package.

Disaggregated grain-size distributions were measured from large-volume (1–15 L) water samples collected during cruises B and C at a subset of stations. Water samples were reduced to <60 ml volume in the lab by repeatedly allowing the suspended sediment to settle for at least a week in a 1-L cylinder, and then siphoning to remove clear fluid. The remaining sediment-water mixtures were brought to 60 ml volume with 0.05% $NaPO_3$, and sonicated to break flocs. Samples were mixed with 40 ml of glycerin and scanned twice in a Micromeritics Sedigraph x-ray particle-size analyzer to obtain disaggregated grain-size distributions from 1 μm to 125 μm diameter. Samples were then dried and weighed to obtain mass concentrations. The two Sedigraph scans were averaged, and the mean data were binned into whole-phi increments to obtain final grain-size distributions ranging from ≥5 ϕ (≥31 μm) to ≤10 ϕ (≤1 μm). Data from the coarse end of the size spectrum were noisy, and thus results from coarse silt to very fine sand (31 μm to 125 μm) were combined into a single size class (≥5 ϕ).

Weighted-mean single-grain settling velocities ($\overline{w_{si}}$) were calculated from large-volume water-sample grain-size distributions as follows:

$$\overline{w_{si}} = \sum f_{si} w_{si} \tag{2.1}$$

where w_{si} is the Stokes' settling velocity for each whole-phi size class i, and f_{si} is the mass fraction of disaggregated sediment measured in that size class.

River-discharge and turbidity data were obtained from USGS sensors located at stations 12045500 (McDonald Bridge) and 12046260 (Diversion Structure), respectively (Curran et al., 2014; USGS, 2017). Provisional suspended-sediment concentrations and suspended-sediment loads (Table 2.1, Figure 2.1c) were obtained from USGS (C. Magirl, personal communication). Reported fluvial discharges and SSCs (Table 2.1) represent 24-h averages from noon on the day preceding the survey to noon on the day of the survey. Tidal water-level data (Figure 2.2b) and mean wind speeds were obtained from NOAA station 9444090 (Port Angeles; NOAA, 2016a) for the period of each survey. Mean wave heights coinciding with each transect were obtained from a pressure sensor mounted on a boundary-layer tripod frame near the river mouth (surveys A, B, and C) or in Freshwater Bay (surveys D, E, F, G); see Eidam et al., 2016 for a description.

Mass fractions of sediment and freshwater in the plume (M_s/M_{total} and M_{fw}/M_{total}) were calculated from SSCs, sediment density, salinities, and water densities. M_{total} was calculated as the sum of the freshwater, saltwater, and sediment fractions of the total mass in a unit volume. Sediment density was assumed to be 2650 kg/m^3. Water densities were computed from the measured temperature and salinity profiles using standard equations of state (Nayar et al., 2016; Sharqawy et al., 2010).

2.3.2 Effective settling velocity calculations

Revisions to the 1D clearance model

Sediment clearance from plumes is often assumed to follow an exponential decay model (e.g., Syvitski et al., 1988; Bursik, 1995):

$$\frac{dI}{dt} = -\lambda I \tag{2.2}$$

where I is the sediment-removal rate from the base of the plume (kg/m^2), λ is a removal-rate constant (1/s), and t is time (s). Given that $I = I_0$ at $t = 0$, the equation can be integrated and re-written as:

$$I = I_0 e^{-\lambda t} \tag{2.3}$$

The sediment-removal rate (I, kg/m^2) multiplied by the removal-rate constant (λ, $1/s$) equals the flux of sediment out of the plume, which can also be expressed as the suspended-sedment concentration (C, kg/m^3) times a vertical settling velocity (w_s, m/s). Based on this relationship, Eq. 2.3 can be re-written in terms of concentration and settling velocity (e.g., Hill et al., 2000):

$$C(x) = C_0 e^{-(w_e/hu)x} \tag{2.4}$$

where *C(x)* is the concentration at an along-plume distance x from the river mouth, C_0 is the initial concentration at the river mouth, u is the plume speed, and h is the depth at which *C(x)* is measured.

By taking the natural logarithm of both sides, Hill et al. (2000) expressed Eq. 2.4 as a 1D clearance model:

$$ln(C^*(x)) = \big(-\frac{w_e}{hu}\big)x + ln(C_0) \tag{2.5}$$

(in the form $y = mx + b$). Because *C(x)* can decrease both by particle removal and by saltwater entrainment (dilution), and only particle removal is of interest, a dilution-corrected concentration $C^*(x)$ is used in place of *C(x)*:

$$C^*(x) = C(x)\frac{S_{max}}{S_{max} - S(x)} \tag{2.6}$$

where S_{max} is the ambient salinity below the plume, and *S(x)* is the salinity measured at the location of *C(x)*. In practice, Eq. 2.5 is applied by plotting the natural logarithm of $C^*(x)$ versus distance from the river mouth (x) for every station, and determining w_e from the slope of the line of best-fit (i.e., $w_e = mhu$).

The 1D clearance model (Eq. 2.5) relies on several key assumptions. First, the plume must be well-mixed (i.e., have a uniform concentration profile), since concentrations are measured at a single depth h. Second, sediment losses must occur through gravitational settling. Potential mechanisms of enhanced removal at the base of the plume like convective sedimentation and turbulence-induced removal (e.g., McCool and Parsons, 2004; Nowacki et al., 2012) are ignored, since point measurements within the plume are used, rather than profiles of SSC that extend to the plume base. Third, the plume is assumed to be in steady-state, i.e., not spreading, thinning, or decelerating, and parcels of plume water are assumed to follow a linear path (or streamline) from the river mouth to the measurement site. In other words, measurements from a constant depth (h) represent an unstretched parcel of water moving in a Lagrangian reference frame, and the elapsed time (or residence time, t) from the river mouth to each station can be determined from $t = x/u$.

These assumptions are often violated in plumes, however, especially in the nearfield zone where saltwater entrainment, spreading, and deceleration may occur (e.g., Garvine, 1982). In theory, measurement errors related to the first two assumptions (uniform concentration gradients and only one mechanism of removal) could be reduced by incorporating elements of a simple sediment conservation equation (e.g., Nowacki et al., 2012):

$$\frac{\partial C}{\partial t} + u\frac{\partial C}{\partial x} + v\frac{\partial C}{\partial y} + w\frac{\partial C}{\partial z} = w_s\frac{\partial C}{\partial z} + \frac{\partial}{\partial z}\left(K_s\frac{\partial C}{\partial z}\right) \tag{2.7}$$

This equation represents the change in concentration with time, sediment flux in the x-, y- and z-directions, gravitational settling flux, and turbulent sediment flux, respectively. Nowacki et al. (2012) integrated Eq. 2.7 to obtain a control-volume equation that expressed the gradient in plume concentration in terms of the total vertical sediment flux times the plume width. By considering a plume of unit width and constant speed, their control-volume

equation can be simplified and re-written as:

$$u\frac{\partial}{\partial x}\Big[\int_{h}^{0} C dz\Big] = \overline{C_h} w_{e'} \tag{2.8}$$

where $w_{e'}$ denotes the total effective settling velocity, and $\overline{C_h}$ represents the depth-integrated mean plume concentration. The quantity $w_{e'}$ includes contributions from both gravitational settling and turbulent removal of sediment at the base of the plume (see Nowacki et al., 2012; Rouhnia and Strom, 2017).

In the simplified reference frame of Eq. 2.8, the change in plume concentration is balanced by the total vertical sediment flux. Vertical flux equals the depth-averaged mean plume concentration ($\overline{C_h}$) multiplied by the total effective settling velocity $w_{e'}$. By substituting these terms into the original 1D clearance model (Eq. 2.5), a revised model can be obtained which accounts for gradients in plume SSC and enhanced removal processes occurring at the base of the plume:

$$ln\big(\overline{C_h^*(x)}\big) = \big(-\frac{w_{e'}}{hu}\big)x + ln(C_0) \tag{2.9}$$

where $\overline{C_h^*(x)}$ is the dilution-corrected form of $\overline{C_h}$ (see Eq. 2.6). The differences between the original concentration and w_e and revised concentration and $w_{e'}$ parameters are summarized in Figure 2.4. Whereas the original model only accounts for gravitational settling from the upper layers of the plume and assumes a uniform SSC profile (Figure 2.4a), the revised model accounts for total removal from the plume and a gradient in SSC (Figure 2.4b).

The effects of non-linear streamlines and plume deceleration can also be addressed if a residence time (t) is known, i.e., the travel time of water at each station since it left the river mouth. For this study, a Delft3D model was used to obtain estimates of t_{m} (see next subsection), where the subscript m means "modeled." Since t is represented in Eq. 2.4 by x/u, Eq. 2.4 can be re-written as:

$$ln(C^*(x)) = \big(-\frac{w_e}{h}\big)t_m + ln(C_0) \tag{2.10}$$

to account for non-linear streamlines and variations in plume speed.

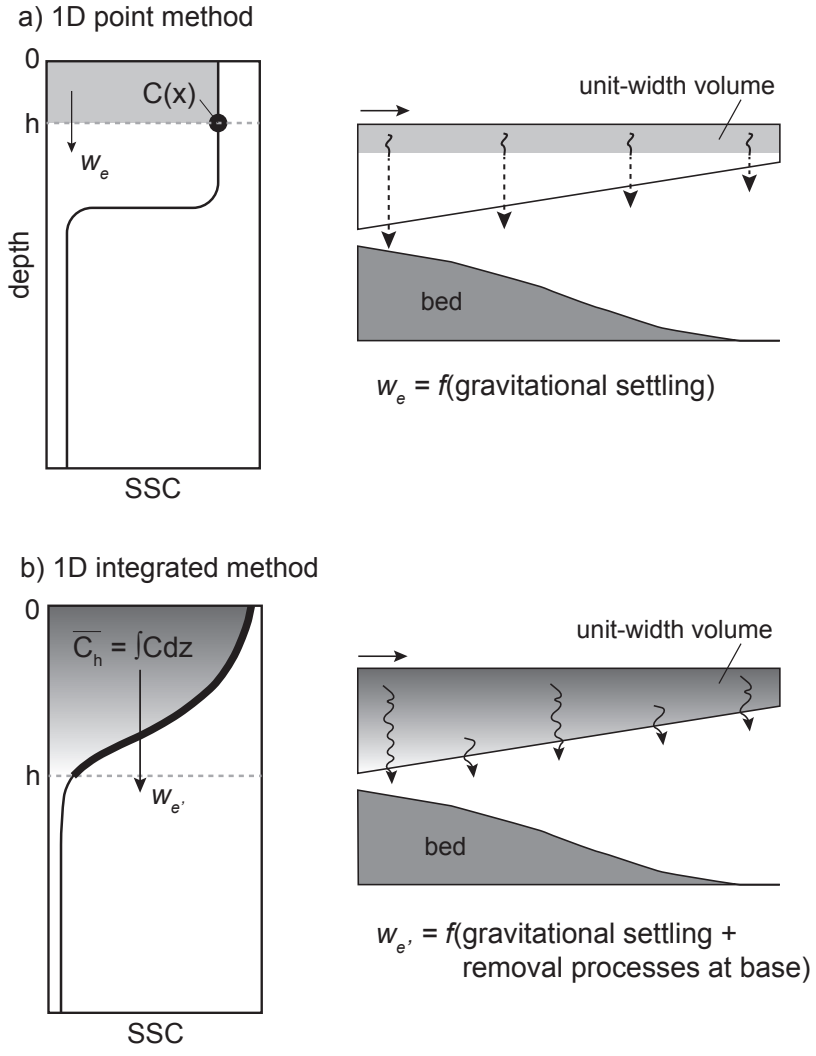

Figure 2.4: Conceptual diagram of 1D-point and -integrated methods. a) The 1D-point method yields w_e, the gravitational component of effective settling velocity. b) The 1D-integrated method yields $w_{e'}$, the total effective settling velocity, which includes removal processes occurring at the base of the plume.

Hydrodynamic modeling of t_m

Hydrodynamic modeling of the Elwha River plume was done by A. Stevens at USGS (personal communication), and was utilized to obtain estimates of plume velocity and salinity fields in this study. The thickness of the plume was defined by the 26 psu isohaline, and a mean plume velocity field was generated for each survey transect by averaging in the z-direction within the plume over 2-4 time steps that coincided with the transect. Plume streamlines were then calculated for each transect period. Station locations were extrapolated to the nearest streamline; stations that fell more than a few hundred meters from streamlines were omitted from analyses. Water residence times at each station were then calculated by integrating the velocity (relative to distance) along the appropriate streamline.

Application of revised 1D clearance model

Based on the original and revised 1D clearance models, effective and total effective settling velocities (w_e and w_e') were calculated from Elwha plume measurements using four methods summarized in Table 2.2. Methods 1 and 2 used point measurements of *C(x)* and *S(x)* at depths of h = 0.4 m. This depth was chosen because it was consistently inside the plume, which was often quite thin (see section 2.4.1). Methods 3 and 4 used depth-integrated mean plume values of SSC, which was integrated from $h \geq 0.2$ m to the base of the plume (h_{max}). The minimum value of $h \geq 0.2$ m was chosen such that all profiles would have a similar starting depth, despite variations in the depth of the first measurement due to waves.

For methods 1 and 3, a constant plume speed of $u = 0.5$ m/s was chosen, based on measurements reported by Warrick and Stevens (2011). This choice was validated by drifter measurements of velocity during survey G (Figure 2.5; see section 2.4.3).

It should be noted that in methods 1 and 2, one value of w_e was determined for each transect, since h was constant. In methods 3 and 4, w_e' was determined for each station in a given transect.

A Kolmogorov-Smirnov test was performed on the results from the four methods; none of

Table 2.2: Summary of methods used to calculated w_e and $w_{e'}$.

	Method 1	Method 2	Method 3	Method 4
Variable of interest	w_e	w_e	$w_{e'}$	$w_{e'}$
Equation	$\ln(C^*(x)) = \left(-\frac{w_e}{hu}\right)x + \ln(C_0)$	$\ln(C^*(x)) = \left(-\frac{w_e}{h}\right)t_m + \ln(C_0)$	$\ln(\overline{C_h^*(x)}) = \left(-\frac{w_{e'}}{hu}\right)x + \ln(C_0)$	$\ln(\overline{C_h^*(x)}) = \left(-\frac{w_{e'}}{h}\right)t_m + \ln(C_0)$
Measurement depth	point (h = 0.4 m)	point (h = 0.4 m)	plume-integrated	plume-integrated
Residence time	$t = x/u$ (u = 0.5 m/s)	t_m	$t = x/u$ (u = 0.5 m/s)	t_m
Tests	None (original equation)	Non-linear streamlines Variable plume speed	Non-uniform SSC	Non-uniform SSC Non-linear streamlines Variable plume speed

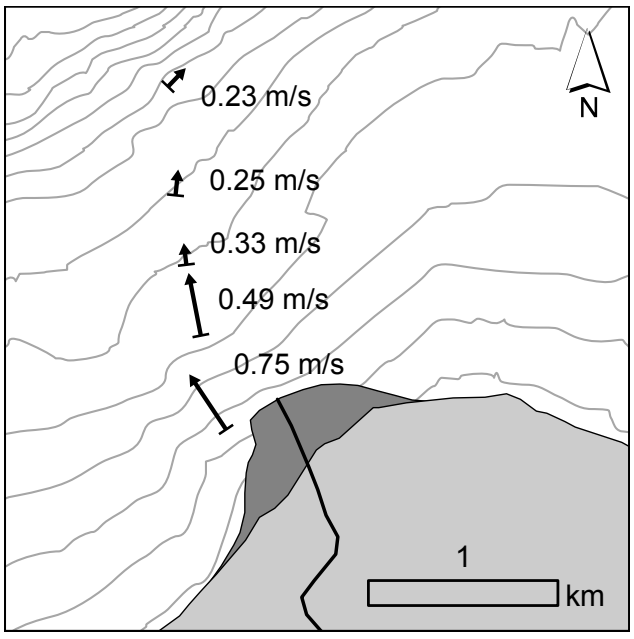

Figure 2.5: Drifter data from survey G. Vectors denote drifter velocity at the starting point of each arrow.

the datasets were normally distributed. Thus, a Wilcoxon rank-sum test (or Mann-Whitney U-test) was performed in lieu of a student t-test to determine if datesets originated from populations with different distributions at the 95% confidence level.

Mean values of w_e' (by transect, from method 4) were compared to environmental parameters (e.g., river discharge and wind speed). Log-linear regressions were performed, and p-values were computed for the slopes of the regressions using an ANOVA (analysis of variance) package.

2.4 Results

2.4.1 Plume and environmental properties (all surveys)

Mean 24-h river discharges for surveys ranged from 40 to 270 m^3/s, and fluvial SSC ranged from ∼0.15 to 6.5 g/L (Table 2.1). Wave heights ranged from ∼0.12 to 0.49 m. Mean wind speeds at Port Angeles during transects were <5 m/s. Tidal ranges and phases varied (Figure 2.2, Table 2.1).

Depth-integrated mean plume SSCs were <2.5 g/L during all surveys, and decreased to <0.2 g/L at distances >1500 m from the river mouth (Figure 2.6a). Strong vertical gradients in plume SSC were commonly observed (Figure 2.6a, inset). Mean plume salinities varied, but were generally ≥20 psu at distances >750 m from the river (Figure 2.6b). Plume thicknesses (as defined by the transition from plume to ambient-seawater salinities and SSC) also varied, and were generally <3 m (Figure 2.6c).

Mass fractions of freshwater and sediment in the plume both decreased sharply within 1500 m of the river mouth during all surveys (Figure 2.7). Horizontal gradients of freshwater and sediment loss were approximately parallel within each survey. Mass fractions of sediment were greatest during surveys A and C, corresponding to the two greatest water discharges (Figure 2.7, Table 2.1).

2.4.2 Disaggregated grain-size distributions and w_{si} (surveys B, C)

Disaggregated grain-size distributions from surveys B and C were dominated by fine silts, very fine silts, and clays (Figure 2.8a). Sands and coarse silts constituted 1–7% of samples collected at 370–880 m from the river mouth, and medium silts constituted 1–18%. Measured size distributions were slightly coarser in survey B than in survey C, despite greater river discharge during C. Mean fractions of finer silts and clays were 39% and 50%, respectively (Figure 2.8a). Weighted-mean disaggregated settling velocities ($\overline{w_{si}}$) calculated from these size distributions were <0.1 mm/s (Figure 2.8b), in the range of Stokes' settling velocities for single-grain settling of finer silts and clays.

Grain-size distributions from plume samples were compared to those from a set of river calibration samples collected by USGS (2017) at non-concurrent times between 2012 and 2015 (Figure 2.9). These example river samples generally contained ∼20-50% sand (Figure 2.9a; USGS, 2017). The mud distributions of the same river samples were generally coarser than the total grain-size distributions of plume samples collected during this study (Figure 2.9b). Sediments in both river mud fractions and bulk plume samples were generally unimodal, with mode in the finer silt to coarser clay size range (Figure 2.9b).

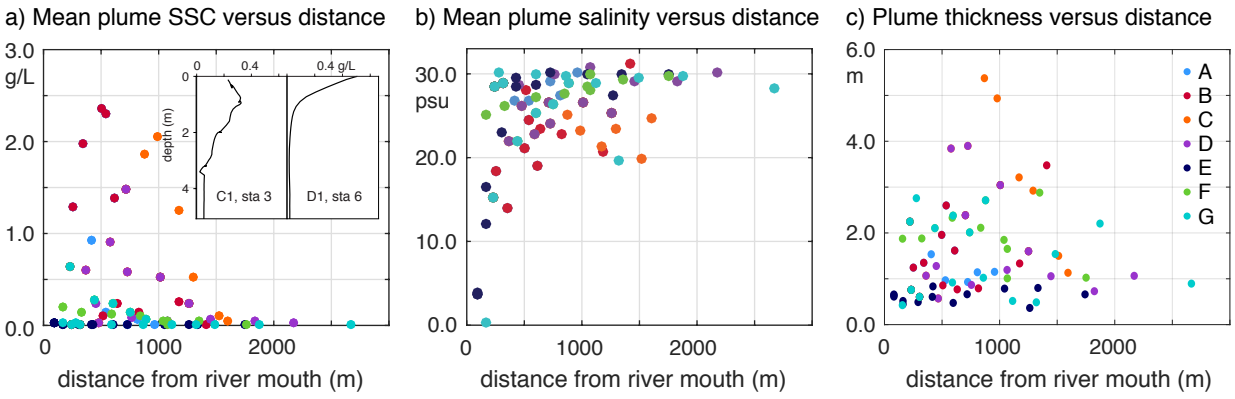

Figure 2.6: Variations in plume properties with distance, for all stations and surveys. a) Mean SSC within the plume, with inset showing example gradients in SSC within the plume. b) Mean salinity within the plume. c) Plume thickness.

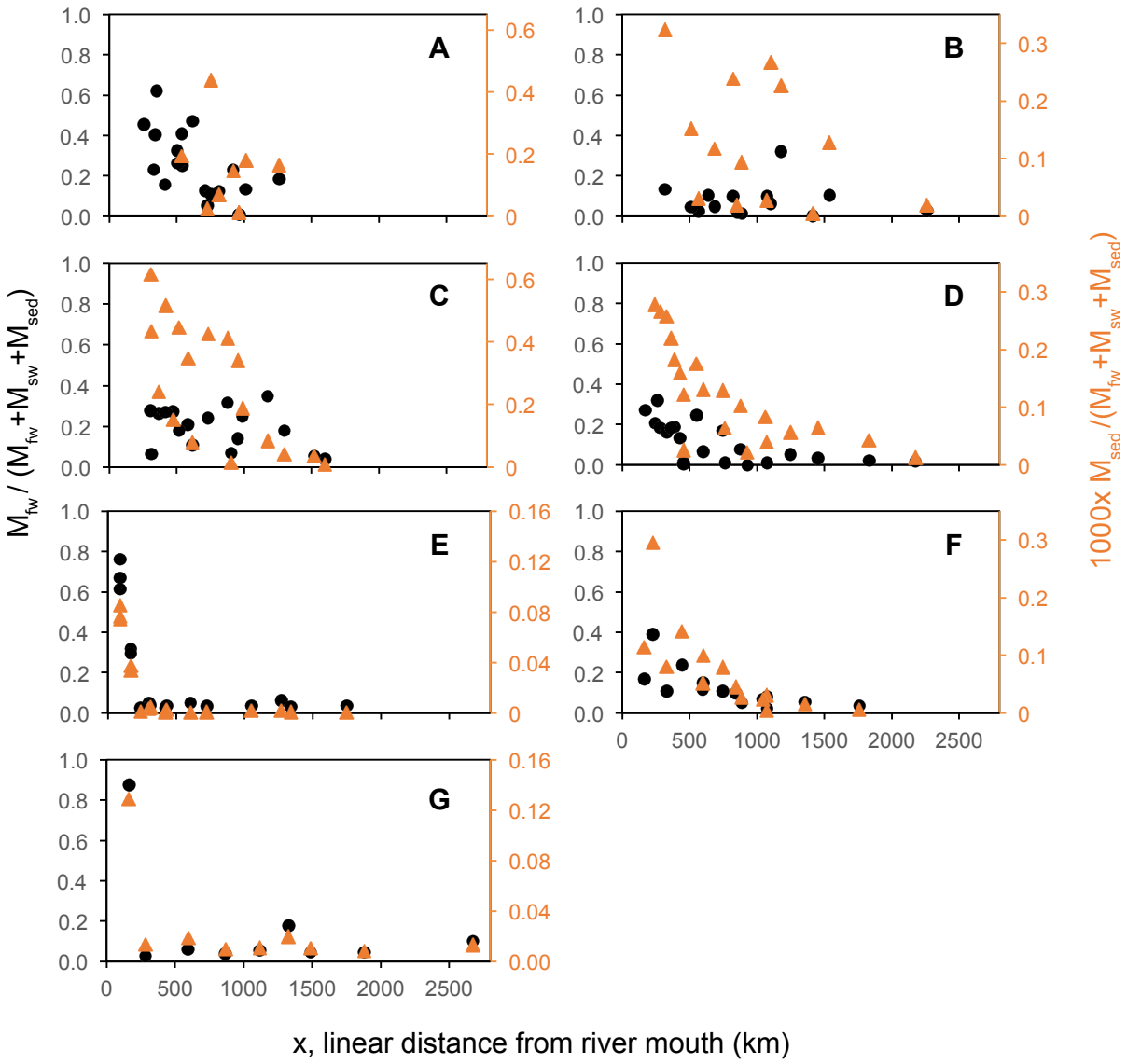

Figure 2.7: Mass fractions of freshwater (black circles) and suspended sediment (orange triangles) along all transects during all surveys. Note that the scales of the right-side axes vary.

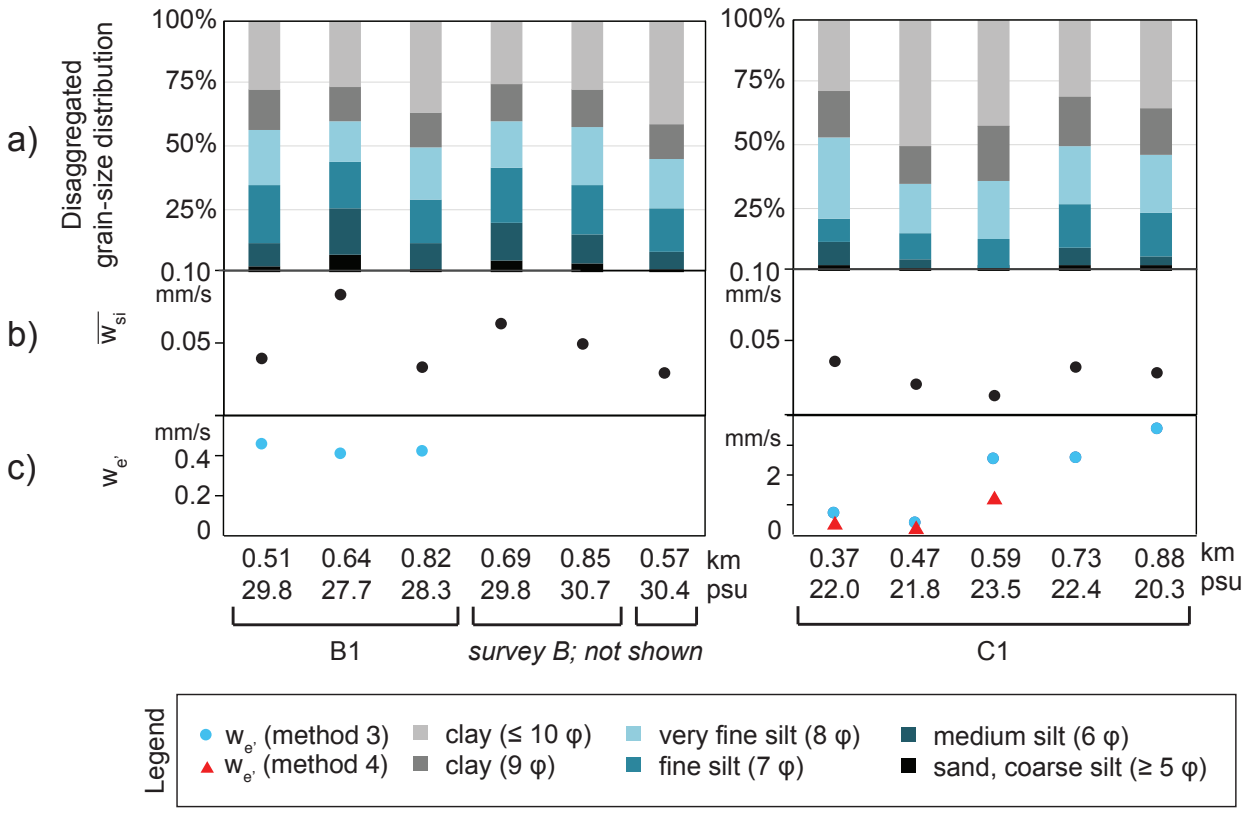

Figure 2.8: Settling velocity and grain-size data for select samples. a) Values of $w_{e'}$, determined from methods 3 and 4. b) Mean disaggregated settling velocities determined from grain-size distributions of bottle samples. c) Disaggregated grain-size distributions from bottle samples, surveys B and C; distance from the river mouth and mean plume salinity are shown on the x axis. Note that three samples are included from survey B which were not part of transect B1.

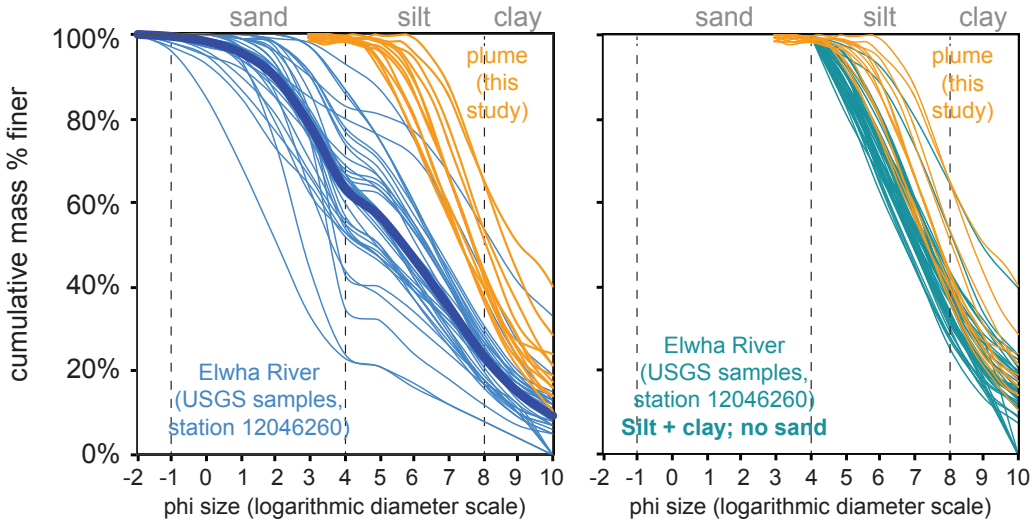

Figure 2.9: Disaggregated suspended-sediment grain-size data from the river and plume. a) Plume grain-size distributions from this study (see Figure 2.8), together with grain-size distributions from 41 river samples collected non-concurrently between 2012 and 2015 at station 12046260 (USGS, 2017). b) Plume grain-size distributions together with grain-size distributions from the mud fraction of the river samples shown in (a).

2.4.3 Velocities and residence times

Modeled plume speeds along streamlines of interest were generally <0.8 m/s (see transect F2 example in Figure 2.10). For many streamlines, little deceleration occurred between the river mouth and sample station. Measured velocities during survey G ranged from ∼0.23–0.75 m/s within 2 km of the river mouth (Figure 2.5). Modeled residence times at sampling stations ranged from ∼1 min to >2 h. Based on modeled velocity fields, many survey transects did not follow streamlines (see F2 example, Figure 2.10).

2.4.4 Estimates of effective settling velocity (w_e)

Estimates of w_e were 0.11–0.66 mm/s for method 1, 0.041–0.33 mm/s for method 2, 0.12–6.5 mm/s for method 3, and 0.13–3.5 mm/s for method 4 (Table 2.3; Figure 2.11). The mean values for methods 1 through 4 (excluding A3, B1, and C1) were 0.28, 0.18, 1.2, and 0.92 mm/s, respectively (Table 2.3). Transects A3, B1, and C1 yielded negative results for meth-

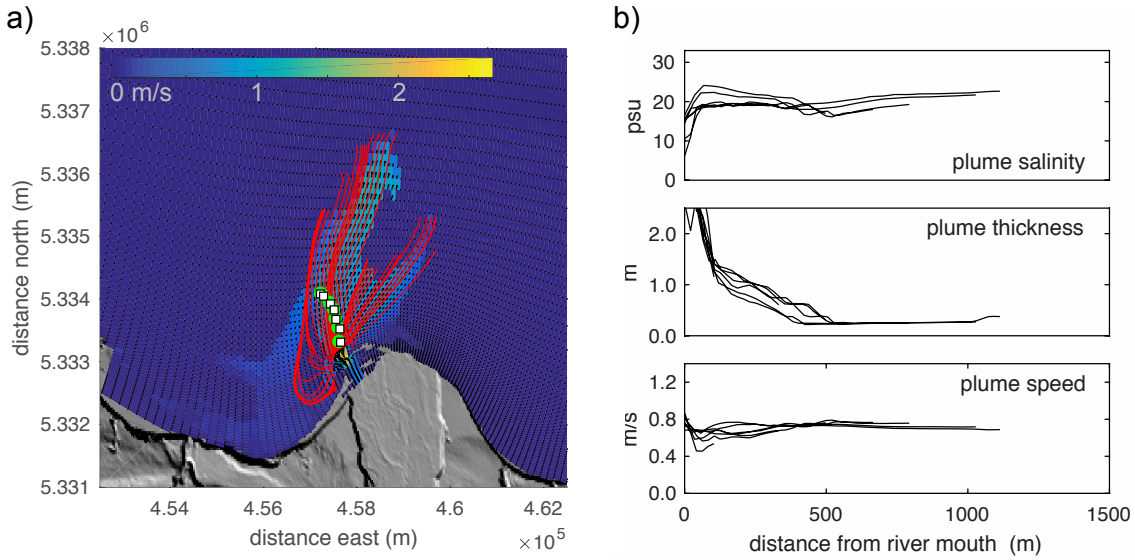

Figure 2.10: Example model output from the plume field coinciding with transect F2. a) Modeled plume velocity field, with streamlines and sample points (green circles). White squares denote sample points extrapolated to the nearest streamline. b) Modeled plume properties along streamlines leading to extrapolated sample points in (a).

ods 2 and 4, and thus those results were omitted from further anlayses. The distributions of results from methods 1 and 2 were not different at the 95% confidence level, nor were the distributions of results from methods 3 and 4. Methods 1 and 3 had statistically different distributions at the 95% confidence level (p-value of 0.010), as did methods 2 and 4 (p-value of 0.021). Values of $w_{e'}$ were generally ∼3–8 times greater than values of w_e (Figure 2.12).

Values of w_e from transects (methods 1 and 2) showed little relation to river discharge (Figure 2.13). Values of $w_{e'}$ obtained for discrete stations using methods 3 and 4 varied among surveys (Figure 2.14; Tables 2.1, 2.3). Along-transect values of $w_{e'}$ were generally constant (Figure 2.14c, d), except for a few transects wherein $w_{e'}$ decreased seaward (A2, C1, and G1).

Values of $w_{e'}$ (method 4) exhibited a weak positive relationship with river discharge, with $R^2 = 0.2$ and p-value of 0.024 (Figure 2.15). Relationships with other environmental parameters were rejected based on p-values >0.05 and/or small correlation coefficients.

Table 2.3: Effective and total effective settling velocity results (mm/s).

Survey transect	Method 1 (w_e)	Method 2 (w_e)	Method 3 ($w_{e'}$)	Method 4 ($w_{e'}$)
A1	0.40	0.23	1.2–2.0	0.82–1.4
A2	0.66	0.23	2.8–6.5	0.96–2.2
A3	0.36	-	0.25–0.63	-
B1	0.60	-	0.42–0.74	-
C1	0.19	-	0.33–3.3	-
D1	0.23	0.15	0.35–0.62	0.21–0.37
E1	0.22	0.18	0.19–0.46	0.22–0.53
E2	0.11	0.17	0.12–0.17	0.19–0.25
F1	0.18	0.041	0.58–1.7	0.13–0.16
F2	0.24	0.33	0.90–2.5	1.3–3.5
G1	0.23	0.13	0.81–4.8	0.47–2.79
Mean (all)	**0.31**	**0.18**	**1.2**	**0.92**
Mean (except A3, B1, C1)	**0.28**	**0.18**	**1.2**	**0.92**

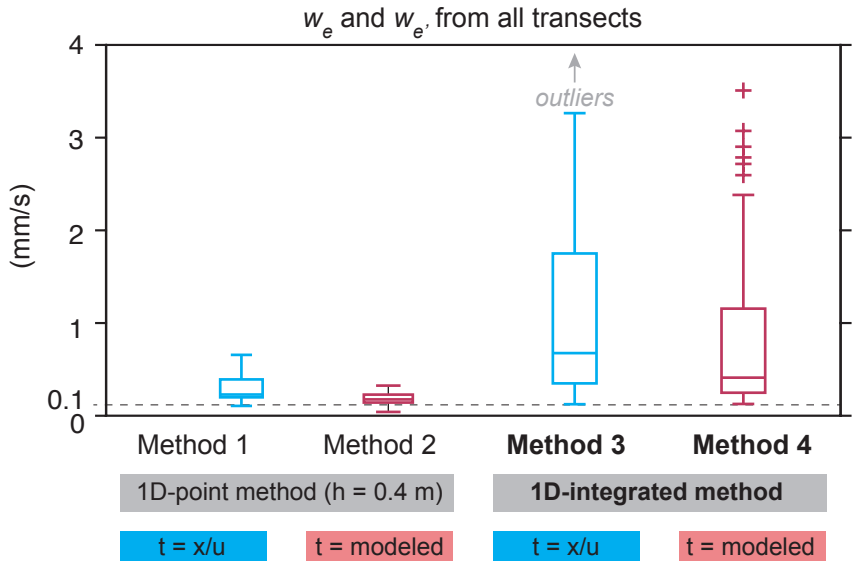

Figure 2.11: Effective and total effective settling velocities (w_e and $w_{e'}$) from all methods. Values of w_e (methods 1, 2) were generally smaller than values of $w_{e'}$ (methods 3, 4). The dashed line denotes 0.1 mm/s, a typical w_e value reported from other field applications of the 1D-point method (method 1).

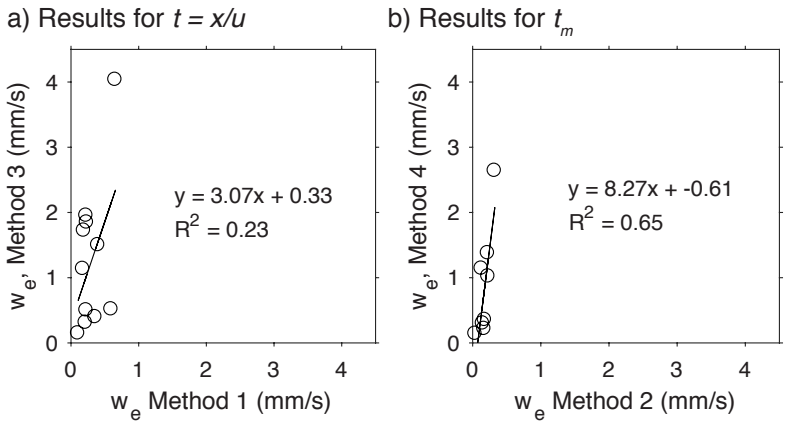

Figure 2.12: Comparisons of methods based on linear regressions. a) Results for $t = x/u$ (methods 1, 3). b) Results for t_m (methods 2, 4).

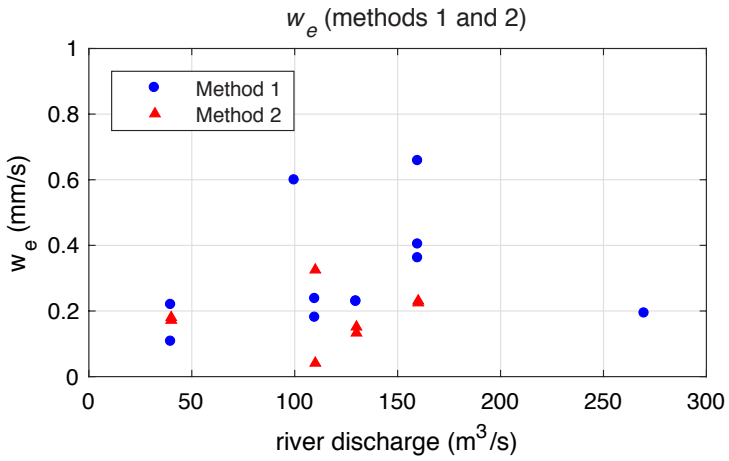

Figure 2.13: Effective settling velocities (w_e) for methods 1 and 2 (based on $h = 0.4$ m) versus river discharge. Values from method 1 (using distance and speed as a proxy for residence time) were generally greater than values from method 2 (using modeled residence times).

2.5 Discussion

2.5.1 Effective settling velocities (w_e) from the 1D-point method

Overall, the 1D clearance model worked well when applied to measurements from the small Elwha plume. Values of w_e (0.11–0.66 mm/s; method 1) for $x \leq 2.5$ km were similar to or greater than those reported from other applications of the 1D clearance model. For example, Hill et al. (2000) found values of 0.06-0.10 mm/s in the Eel River plume ($x \leq$30 km), and Wu et al. (2006) found values of 0.07–0.14 mm/s in the Herbert River plume ($x \sim$2–12 km). The 1D clearance model (based on point measurements at a constant depth) thus seems to work reasonably well even in the nearfield zone of the small Elwha plume.

The magnitudes of w_e in the Elwha plume suggest that the suspension is partially flocculated. Values are greater than $\overline{w_{si}}$, but smaller than the typical 1 mm/s settling velocity expected for flocs (e.g., Sternberg et al., 1996; Hill et al., 1998; Mikkelsen et al., 2007). Hill et al. (2000) and Curran et al. (2002) obtained similar w_e estimates for the Eel River plume, and used detailed grain-size measurements from the river and plume to estimate a

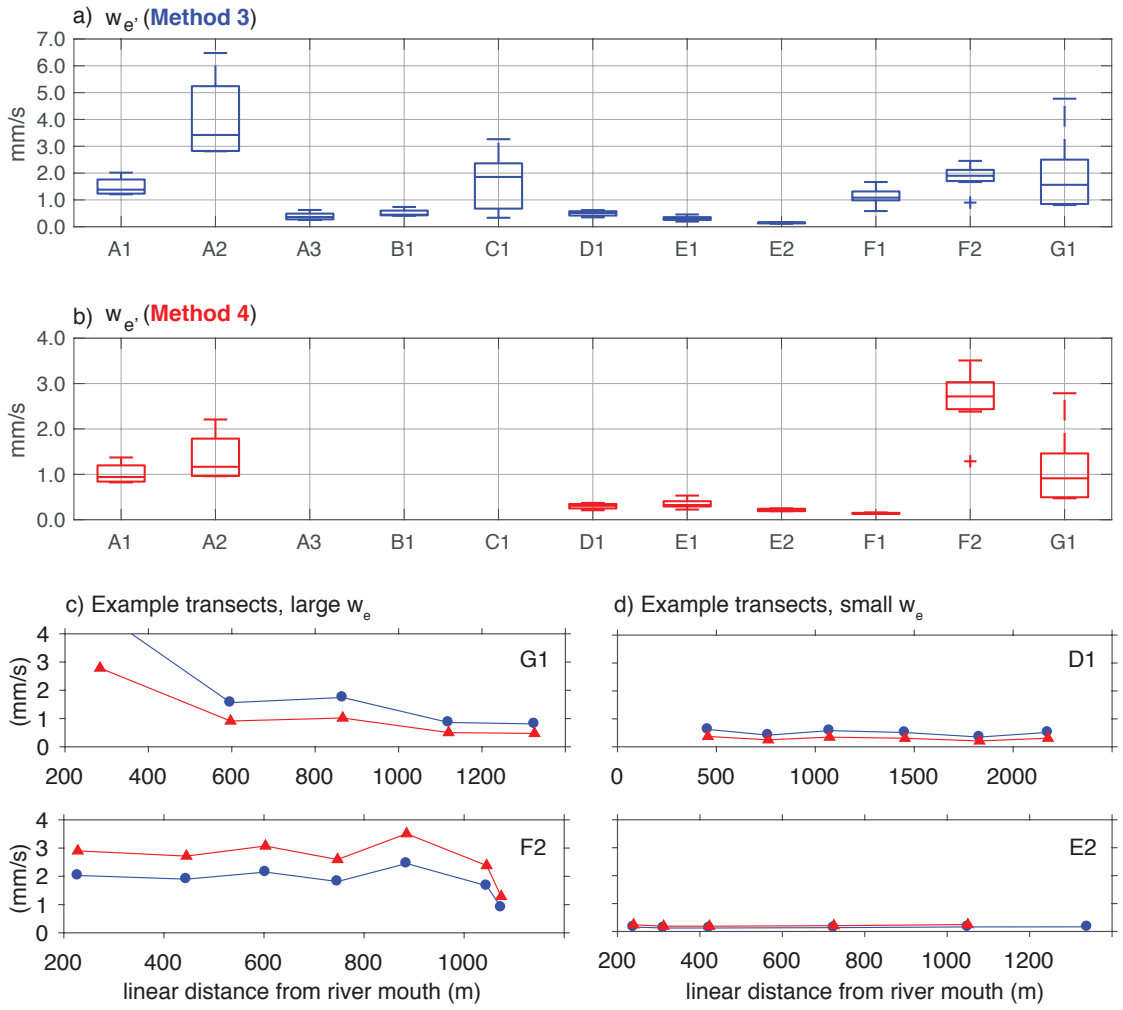

Figure 2.14: Values of $w_{e'}$ for methods 3 and 4, organized by transect. a) Method 3 results. b) Method 4 results. c) Example transects G1 and F2, showing the evolution of large $w_{e'}$ values with distance. d) Example transects D1 and E2, showing the evolution of small $w_{e'}$ values with distance.

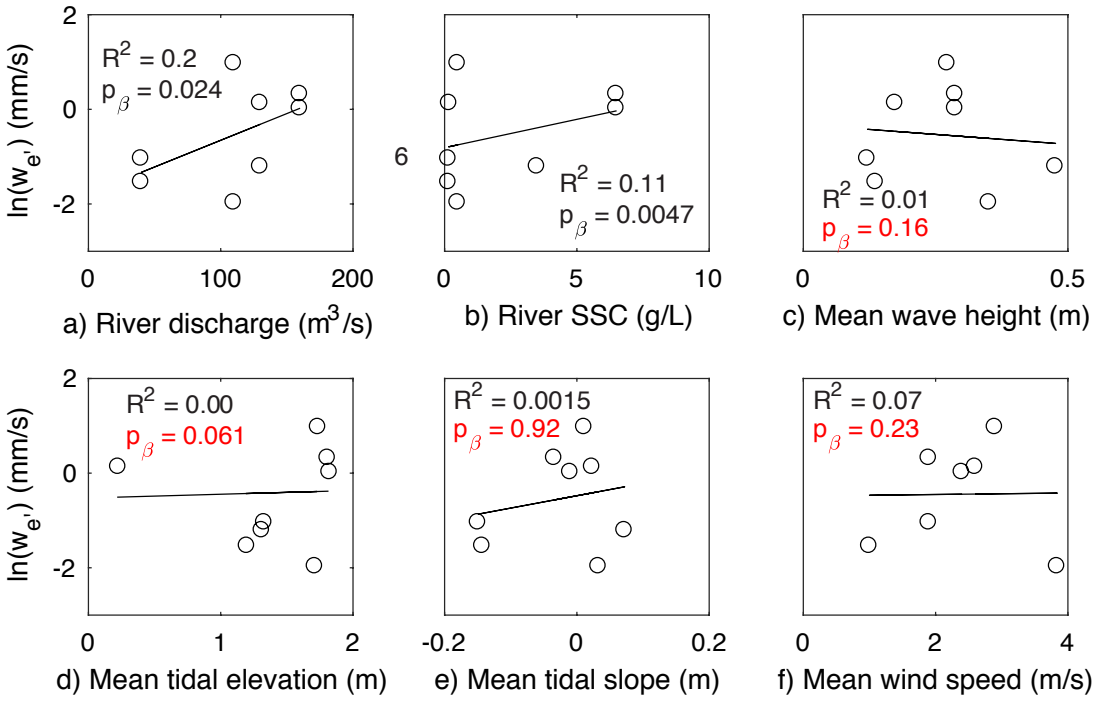

Figure 2.15: Natural logarithms of mean values of $w_{e'}$ (by transect; method 4) versus environmental parameters: a) Mean river discharge; b) Mean river SSC; c) Local wave height; d) Mean tidal elevation; e) Mean tidal slope; f) Mean wind speed. Correlation coefficients for linear regressions and p-values for regression slopes are shown. P-values >0.05 are highlighted in red.

floc fraction (f) of ~0.75. Because $f < 1$, and because w_e was less than 1 mm/s but still greater than w_{si}, they concluded that the Eel plume was partially flocculated. While grain-size measurements from this study are insufficient to determine a floc fraction, the general magnitudes of w_e are consistent with rapid removal of sediment beyond what single-grain settling could accomplish.

Interestingly, w_e calculations were insensitive to the use of t_m versus $t = x/u$ (method 2 versus method 1; Figure 2.11). Statistically, the distributions were the same at the 95% confidence level, and the sample means were ≤0.3 mm/s. The results were probably similar because little deceleration occurred in many surveys (per modeled streamlines, e.g., Figure

2.10), meaning the assumption of a constant plume speed was reasonable. Furthermore, the differences in path lengths for t_m versus $t = x/u$ were apparently small (e.g., ∼20% for the example shown in Figure 2.10) relative to other sources of variation.

In short, despite the strong tidal forcing and rapid changes in thickness that are characteristic of the Elwha plume, the 1D-point method yielded w_e values similar to those found in other systems. Thus, the method shows promise for characterizing w_e in the nearfield zone of a very small dynamic plume, even if survey transects cross-cut streamlines.

2.5.2 Total effective settling velocities ($w_{e'}$) from the 1D-integrated method

While the effective settling velocities (w_e) obtained from the 1D-point method were consistent with those found in other studies, they likely underestimate the total effective settling velocities for two reasons: 1) strong gradients in SSC were observed in the Elwha plume and 2) previous studies have identified contributions to $w_{e'}$ from enhanced removal processes at the base of the plume. Because SSC decreases with depth in the plume, and because the thickness of the plume changes rapidly with distance (Figure 2.6), w_e calculations based on *C*(x)* in the 1D-point method could over- or under-estimate w_e by accounting only for the concentration gradient in the uppermost layer (Figure 2.4). In other words, the 1D-point method doesn't account for SSC changes due to thinning or spreading (rather, only saltwater entrainment). The possibility of unevenly-distributed flocs within the plume is also ignored. Though the effects of plume spreading are not well-constrained in a 1D approach (as opposed to a control-volume approach), using $\overline{C*_h}$ in the 1D-integrated method proposed here accounts for gradients in SSC, an improvement over the 1D-point method.

Estimating w_e from *C*(x)* at a single depth within the plume also neglects processes of sediment removal that may occur at the plume base, like turbulence or gravitational instabilities (e.g., McCool and Parsons, 2004). Turbulence-induced mixing in particular has been identified as a minor to moderate contributor to total effective settling velocity in the field and lab (Nowacki et al., 2012; Rouhnia and Strom, 2017). In a flume study, Rouhnia and Strom (2017) found that turbulence-induced sediment removal became increasingly impor-

tant at low Richardson numbers (Ri), i.e., below a critical value of $Ri_{cr} = 0.25$ based on surficial plume speeds, or $Ri_{cr} = 1.0$ based on depth-averaged plume speeds (see also Geyer and Smith, 1987).

Estimated Ri for the Elwha plume, based on the modeled, depth-averaged velocities, were generally <1.0, suggesting that mixing at the base may be an important process for sediment removal. Strong mixing is also evident in the loss of most freshwater from the plume within ∼1500 km of the river mouth (Figure 2.7). Thus, some of the difference between the 1D-point results (w_e) and 1D-integrated results ($w_{e'}$) may reflect turbulent mixing. Total effective settling velocities were up to ∼3–8 times greater than effective settling velocities (Figure 2.12). Because this difference between $w_{e'}$ and w_e is greater than that found in prior studies (Nowacki et al., 2012; Rouhnia and Strom, 2017), this system likely experiences a high degree of mixing-induced removal, rapid loss of fast-settling macroflocs from the lower region of the plume, or some other enhanced removal mechanism. Rapid loss of macroflocs may have occurred during some surveys where an along-transect gradient in $w_{e'}$ was observed (e.g., G1, Figure 2.14c). However, $w_{e'}$ was relatively constant along-transect for most surveys, suggesting a stable population of microflocs (see Mikkelsen et al., 2006). Thus, much of the difference between $w_{e'}$ and w_e is attributed to a large degree of basal mixing.

Like the 1D-point results, the 1D-integrated results were generally insensitive to the use of approximated versus modeled residence times, as evident by the similar distributions of results (method 3 versus method 4 in Figure 2.11) and similar across-isobath trends in $w_{e'}$ (Figure 2.13). Results were sensitive to the choice of plume speed, however; assumed plume speeds of ∼0.1–0.8 (in lieu of a single value of $u = 0.5$ m/s) were required to reproduce the results of method 4 using method 3 for most surveys. This exercise simply highlights the need for reliable speed estimates in the 1D-integrated method, and suggests that results from method 4 better represent $w_{e'}$ than those from method 3.

Magnitudes of $w_{e'}$ reflect a well-flocculated plume suspension, since the values are much greater than $\overline{w_{si}}$ (see Kineke and Sternberg, 1989) and are within the range of floc settling velocities reported in other studies (e.g., Sternberg et al., 1996; Hill et al., 2000). Further-

more, the relatively constant proportions of clays and silts observed for transects B1 and C1 (Figure 2.8) suggest equal removal of multiple sediment sizes through flocs rather than single grains, as noted by Kranck (1980).

Results from methods 3 and 4 can be further validated using a simple scaling argument. Wu et al. (2006) used w_e estimates from the Herbert River plume to estimate the "characteristic distance of sediment expansion," or plume length scale (x_p), as follows:

$$x_p = -\frac{uh}{w_e} ln\left(\frac{C(x)}{C_{RW}}\right) \tag{2.11}$$

By defining the limit of the plume as the point at which 99% of the original sediment had been lost (i.e., $C(x) = 0.01 C_0$), they calculated an x_p value that was similar to the offshore distance of the 5 NTU (nephelometric turbidity unit) SSC contour, thereby validating the use of the 1D model and chosen parameters. By choosing $C(x) = 0.03 C_{RW}$ for the Elwha plume (to account for background turbidity values of 0.005 g/L), x_p was calculated as follows:

$$x_p = 3.5\frac{uh}{w_e} \tag{2.12}$$

using mean plume thicknesses for h, and $w_{e'}$ values from method 3 that were re-calculated with optimized values of u such that they were approximately equal to the results from method 4. The resulting x_p values were generally <5 km (Figure 2.16), consistent with modeled salinity contours of ~25–28 psu and gradients in plume freshwater and sediment (Figures 2.6, 2.7). This simplistic scaling offers further evidence that the calculated $w_{e'}$ values are reasonable, and that $w_{e'}$ values obtained from a basic set of measurements (i.e., salinity and SSC profiles) can be used to predict approximate length scales of sediment dispersal.

2.5.3 Particle packaging and dispersal in the Elwha plume

Because values of $w_{e'}$ are similar to published floc settling velocities (Figure 2.11), and because little sorting of particle sizes was observed (Figure 2.7), sediment in the Elwha plume is likely partially to well-flocculated, with relatively rapid clearance rates. This rapid clearance is reflected in the steep gradients of SSC within 2 km of the river (Figures 2.6,

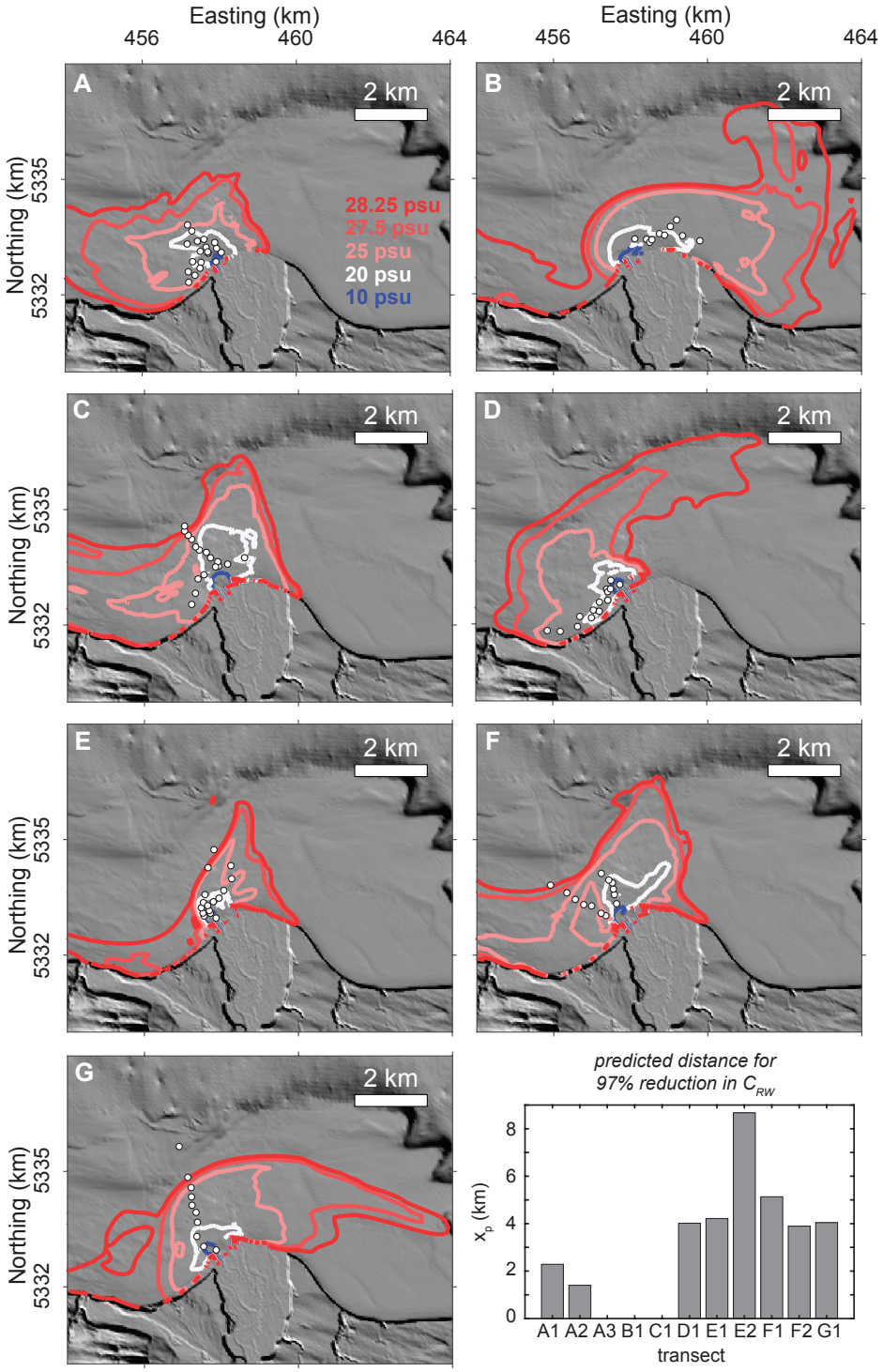

Figure 2.16: Modeled mean salinity fields for the surface plume during the surveys, and histogram (lower right) of predicted dispersal distances, i.e., distances required for 97% clearance of the initial SSC.

2.7) and by the scaling argument (see previous section). Flocculation is not surprising in this system, since flocs generally begin forming at salinities >1 psu (e.g., van Leussen, 1988), timescales of flocculation are on the order of a few minutes (e.g., Milligan, 1995; Curran et al., 2003) and well within the modeled residence times, and fluvial grain-size distributions of the Elwha River are clay-rich (40–66%, Figure 2.8a) relative to other systems with abundant flocs (Eel: 25% clay, Morehead and Syvitski, 1999; Burdekin: 36% clay, Bainbridge et al., 2012). The $w_{e'}$ values were generally smaller than those measured in the Columbia River plume, however (Nowacki et al., 2012). In the Elwha system, the small estuary (see Foley et al., 2015, in press) may limit the time needed for large macroflocs to grow before reaching the plume. Macrofloc growth occurs in ∼10 minutes in lab studies (e.g., Milligan, 1995; Curran et al., 2003). Furthermore, the small watershed size and glacial origin of sediments may limit the diagenesis of silt- and clay-size particles, though the timescales for diagenesis and effects on flocculation are unknown. Any effect on flocculation caused by ∼100 years of sediment and organics storage in the dammed reservoirs is also unknown.

Based on these poorly constrained characteristics of the local environment, as well as studies of other systems, the weak environmental relationships shown in Figure 2.14 are unsurprising. Many attempts to relate in situ w_f values to river discharge, wind speeds, wave heights, and other parameters for other systems have been inconclusive (e.g., Milligan and Hill, 1998; Curran et al., 2002). Curran et al. (2002) compared Eel plume w_e values to several parameters including river discharge and wave heights, but only found relationships with wind speed and tidal current speed. The weak positive relationship between $w_{e'}$ and river discharge suggests that clearance rates may increase during floods, but the exact reason—e.g., an increase in coarse single grains or an increase in flocculation rate—is unknown.

2.5.4 Implications and recommendations for future applications

The effective settling velocities (w_e) computed from the 1D-point method were similar to or slightly greater than values reported in other studies at greater distances from rivers. Thus, the 1D-point method seems applicable even in the nearfield zone of a very small, tidally

forced plume. This method is recommended for well-stratified plumes which experience little mixing and have uniform SSC profiles. However, for plumes which experience substantial mixing at the base and have gradients in SSC, the 1D-integrated method is recommended, based on the $w_{e'} > w_e$ relationship found in this study. The 1D-point method does not account for gradients in concentration or removal processes at the base, and the values of $w_{e'}$ from this study suggest that these effects are important in the nearfield zone of a tidally forced plume. Fortunately, using profile measurements rather than point measurements is relatively simple to do, given modern high-frequency profiling instruments.

The 1D-integrated method is also attractive for $w_{e'}$ characterizations because it is relatively insensitive to how residence time is calculated. In other words, it is not essential to follow streamlines in the field (which is logistically challenging in a small boat on a muddy ocean) nor to use a hydrodynamic model to calculate streamlines and residence times. The linear-distance approximation ($t = x/u$) provides reasonable results at a relatively low cost.

A key limitation of the 1D-integrated method is that it does not account for changes in the plume geometry in the y-direction, i.e., spreading. Nowacki et al. (2012) calculated w_e via the method of Hill et al. (2000) and compared the $w_{e'}$ results from control-volume estimates, and found similar results. Thus, the effects of plume spreading may not have a substantial impact on $w_{e'}$.

2.6 Conclusions

A simple 1D clearance model was used to calculate effective settling velocities (w_e) from the Elwha River surface plume, based on point measurements of salinity and SSC together with estimated and modeled plume speeds (i.e., the 1D-point method). Values of w_e were on the order of 0.1 mm/s, and were similar to values determined from two published field studies using the same method. The 1D-point method thus seems to have utility even in dynamic, nearfield zones of small-scale, highly turbid plumes. In application, values of w_e were relatively insensitive to the use of straight-line streamline approximations versus modeled streamlines. In other words, reasonable w_e values can be obtained from transects

that cross-cut streamlines.

Total effective settling velocities ($w_{e'}$) were also calculated using a modified version of the 1D clearance model that relied on integrated profiles of SSC from within the plume (i.e., a 1D-integrated method). Past studies have suggested that total effective settling velocity reflects both gravitational settling from a plume and enhanced sediment removal at the base of the plume. Results from this study validated this idea, insomuch as $w_{e'}$ (from the 1D-point method) exceeded w_e. Estimated Richardson numbers for the plume indicate that mixing is important, and thus turbulence-induced removal at the base of the plume may account for the high $w_{e'}$, as proposed by previous studies. Additional processes like loss of macroflocs from the lower part of the plume may also explain the difference in values, but in this system, $w_{e'}$ values were generally constant in the across-isobath direction, suggesting a stable population of microflocs in the plume.

Ultimately, the results suggest that the 1D-integrated method is a useful tool for characterizing $w_{e'}$ using simple profile measurements, even in the nearfield zone ($<$2.5 km from the river mouth) of a small, tidally forced plume. These results can in turn be used to predict general length scales of sediment dispersal from a plume, which may be useful in coastal modeling efforts.

Chapter 3

OBSERVATIONS AND MECHANICS OF A GRAVITY FLOW AT THE MOUTH OF A SMALL MOUNTAINOUS RIVER [1]

3.1 Introduction

Rivers dominate the terrestrial transport of sediment to the ocean, and sediment-gravity flows are responsible for much of the subsequent marine transport of particulates from shallow sources to deep and/or distal sinks (e.g., Talling et al., 2015). Marine sediment-gravity flows occur in diverse forms, including: autosuspending turbidity currents triggered on steep slopes; wave- and current-supported fluid muds on gently sloping, energetic shelves; hyperpycnal plumes triggered directly from small, muddy rivers; and hyperpycnal flows initiated indirectly by processes like sediment failures. These events tend to be episodic, energetic, and/or short-lived, and thus challenging to study. Few sediment-gravity flows have been observed in natural systems (Alexander and Mulder, 2002; Talling et al., 2015; Hughes Clarke, 2016), though their deposits are recognized in a variety of modern and ancient sediments worldwide (e.g., Piper and Normark, 2001; Prior et al., 1987; Bouma, 2000).

Because these flows can be a key agent of cross-shelf sediment transfer, ongoing research efforts have aimed to document flow mechanics in situ. In this study, two instrumented boundary-layer tripod systems were stationed seaward of the Elwha River mouth from 2011 to 2014, during an unprecedented dam-removal project. Peak fluvial suspended-sediment concentrations were predicted to reach 30–50 g/L during dam removal (Randle et al., 1996)—i.e., concentrations sufficient to form hyperpycnal plumes. The two tripods were deployed within 1 km of the mouth to monitor for gravity flows, and in 2014 an event lasting

[1]This chapter is formatted for journal submission as: Eidam, E.F., Ogston, A.S., Nittrouer, C.A., Observations and mechanics of a gravity flow at the mouth of a small mountainous river.

∼10 h was recorded. The event deposited ∼15 cm of sand and mud near the river mouth, though the deposit was eroded within three weeks by strong currents. This paper presents the hydrodynamics and sediment dynamics of the gravity-flow event in order to 1) characterize the style of gravity-flow process(es) that occurred; 2) explore the possible mechanisms of flow extinction; and 3) discuss the implications of these events (and the subsequent sediment erosion) to the role of gravity flows in dispersing sediment in other high-energy environments.

3.2 Background

3.2.1 Hyperpycnal plumes and flows

Hyperpycnal plumes are a sub-type of gravity flow formed by plunging rivers, i.e., rivers carrying sufficient suspended sediment to overcome the density of ambient seawater and become negatively buoyant (e.g., Bates, 1953). Hyperpycnal plumes were likely a key mechanism of sediment transport to deep-ocean sinks during past sea-level lowstands, when rivers discharged directly to continental slopes, and continental-scale glacial retreat produced high fluvial sediment loads (e.g., Plink-Björklund and Steel, 2004). Today, hyperpycnal plumes are predicted only from high-yield medium and small rivers during extreme sediment-loading events such as floods, landslides, post-fire erosion, and glacial outburst floods (Mulder and Syvitski, 1995). The critical suspended-sediment concentration (SSC) needed to produce a negatively buoyant hyperpycnal plume is commonly cited as 35–45 g/L (e.g., Mulder and Syvitski, 1995; Warrick et al., 2004; Mulder et al., 2003). This threshold value depends on the salinity of the receiving basin, and could be 1–2 orders of magnitude smaller given seawater entrainment in a river mouth or estuary (Felix et al., 2006). Hyperpycnal flows are a more general type of gravity flow often associated with extreme sediment discharge events, but not formed directly from plunging river effluent (e.g., Mulder et al., 2003). For example, rapid sedimentation at the mouth of a river may lead to the formation of a hyperpycnal flow when the tidal elevation decreases and the deposit becomes unstable (e.g., Clare et al., 2016). Rapid/convective sedimentation from plumes leading to concentrated boundary-layer

suspensions may also produce hyperpycnal flows (Parsons et al., 2001; Warrick et al., 2008). And on the continental shelf, wave and current re-working may initiate flows from previously deposited fluvial sediment (Traykovski et al., 2000; Hale et al., 2014).

Though hyperpycnal plumes (or flows) may only occur every 1–1000 years for many small rivers, they are likely important mechanisms of fluvial sediment dispersal (e.g., Mulder and Syvitski, 1995). Most knowledge about hyperpycnal plumes and flows is derived from modern and ancient sediment deposits and modeling studies, however. Few incontrovertible measurements of direct hyperpycnal plumes are available, but several studies have yielded valuable insights into delayed hyperpycnal-flow formation hours to days after peaks in river discharge, or multi-stage gravity-flow events. The hydrodynamics and sediment-dispersal styles of these events vary widely. For example, flows 20-40 cm thick with sediment concentrations >10 g/L were observed near the Santa Clara River within hours of river flood peaks, and likely formed from enhanced settling processes (or possibly a hyperpycnal plume; Warrick et al., 2008). Hyperpycnal flows are also thought to occur offshore of the Sepik River, following temporary trapping in the river mouth during floods and subsequent flow down a steep canyon (Kineke et al., 2000). Gravity flows >30 m thick with speeds >3 m/s were measured in in Bute Inlet during spring floods of the Homathko River (Prior et al., 1987). Hyperpycnal plumes likely formed from the Waiapu River during floods, given sediment concentrations >50 g/L in the river, but had limited seaward dispersal and were re-initiated later by waves and currents (Ma et al., 2008).

Temporary river-mouth storage and/or delta-front failures have generated hyperpycnal flows offshore of the Squamish Delta (Clare et al., 2016) and Fraser Delta (Ayranci et al., 2012) under favorable tidal conditions, e.g., tidal water-level decrease and unloading of freshly deposited sediments. Gravity flows have also been measured in Monterey Canyon, though they occur both in-phase and out-of-phase with river flood events, and are sometimes triggered by wave events or sediment failure at the canyon head (Paull et al., 2003; Johnson et al., 2001; Xu et al., 2004). Rivers in Taiwan exhibit great potential to generate hyperpycnal plumes (Milliman and Kao, 2005), and cable breaks (Carter et al., 2012), deep-sea

temperature anomalies (Kao et al., 2010), and sediment signatures (Chiang and Yu, 2008) suggest that typhoon-generated hyperpycnal flows may travel >100 km from the coast in steep channel networks to >2000 m water depth. On the Huanghe Delta, tidal currents can both initiate and extinguish hyperpycnal flows, and tend to limit the cross-shelf runout distance of flows (e.g., Wright et al., 1986, 1990; Li et al., 1998). While these studies represent some of the most compelling observations of marine hyperpycnal flow processes, additional studies have inferred such flows from sedimentary deposits, e.g., deposits from the Malpasset Dam failure (Mulder et al., 2009), the Var turbidite system (Mulder et al., 2001), and various historic deposits and outcrops (e.g., Girard et al., 2012; Plink-Björklund and Steel, 2004; Goldfinger et al., 2012).

In the above examples, flows range from centimeters to meters thick, with speeds of a few centimeters to a few meters per second, and have runout distances of >1 km to >100 km. Small reductions in near-bed salinity have been observed at a few km to >100 km from river mouths, and triggering mechanisms range from direct river plunging to turbulent resuspension of unstable sediment after a flood. Much remains to be learned about the nature and frequency of these events, a difficult task given their episodic nature. The present study took advantage of planned dam removals on the small mountainous Elwha River to observe gravity flows in situ. During dam deconstruction, fluvial sediment loads were frequently several grams per liter and occasionally >10 g/L during winter storms and spring snowmelt events (USGS, C. Magirl, personal communication). Boundary-layer tripod systems were deployed ∼200 m and 700 m from the mouth, in order to measure the coastal impacts of these sediment loading events. In early March 2014, a gravity-flow event occurred during the second peak in a two-stage river flood, and >15 cm of well sorted sand were deposited at the base of the delta foreset. Within three weeks, the deposit had been eroded. The dynamics of the event and subsequent erosion are evaluated here, and placed in the broader context of hyperpycnal flows from small rivers.

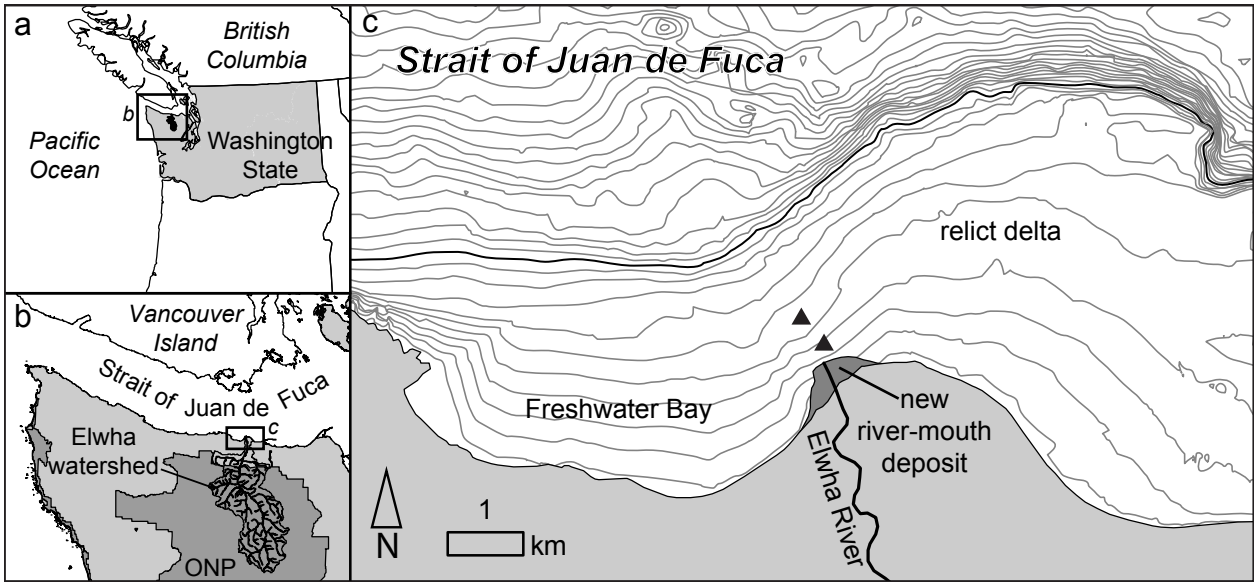

Figure 3.1: Study location. a) Northwest Washington and surrounding regions. b) Strait of Juan de Fuca, with the Elwha watershed highlighted within Olympic National Park. c) Instrument deployment sites on the relict delta near the new river-mouth deposit, east of Freshwater Bay. (Bathymetry contours are 5 m and the 50-m contour is bold; data were accessed from www.ocean.washington.edu/data/pugetsound.)

3.2.2 Regional setting

This study was conducted seaward of the Elwha River, a small mountainous river draining an 830-km^2 mountainous watershed on the Olympic Peninsula in Washington State, USA (Figure 3.1a, 1b; Duda et al., 2008). Mean annual river discharge is ∼40 m^3/s, but fall/winter floods and springtime snowmelt can produce discharge peaks of ∼200–300 m^3/s (USGS, 2017).

Two hydroelectric dams were constructed between 1913 and 1927 within 22 km of the coast, and together trapped ∼21 million m^3 of sediment by 2010 in reservoirs. Impounded sediments were ∼55% sand/gravel and ∼45% silt/clay (Gilbert and Link, 1995; Randle et al., 2015). Both dams were removed between 2011 and 2014, representing the largest planned dam removal ever conducted (Randle et al., 2015).

The Elwha River discharges to the Strait of Juan de Fuca, a tidal strait connecting the

Pacific Ocean to Puget Sound and the Strait of Georgia. Mixed, semi-diurnal mesoscale tides and a large tidal prism produce currents that can exceed 100 cm/s in the central strait (e.g., Fissel and Huggett, 1976). A complex history of glaciation and sea-level change resulted in the formation of a lowstand delta platform, which is now a submerged relict delta north of the modern suaberial delta (Figure 3.1c; Anderson, 1968). Tidal-current flow around the delta headland produces strong, flood-dominant, along-isobath tidal currents with maximum speed of >80 cm/s during spring tides and ∼50 cm/s during neap tides (Eidam et al., 2016). Significant wave heights near the river mouth average ∼0.5 m, with maximum values >2 m; wave orbital velocities are typically <20 cm/s (Eidam et al., 2016).

Between Sep 2011 and Sep 2013, >8 million tonnes of sediment were exported by the river to the coast, and river turbidities frequently exceeded 1000 formazin backscatter units (FBU) during discharge events, representing a few grams per liter of suspended sediment (USGS, 2017; Curran et al., 2014). More than 2.5 million m^3 of sand and gravel deposited at the river mouth (Gelfenbaum et al., 2015), while ∼95% of the fine-grained sediment delivered to the coast was exported to distal sinks by energetic, asymmetric tidal currents (Warrick et al., 2015; Eidam et al., 2016). A muddy surface plume 1–3 m thick commonly formed seaward of the river mouth, with measured turbidities of ∼0.010 to >2.0 g/L (Eidam et al., 2016). Baseline studies classified the plume as small-scale and strongly influenced by tidal currents (Warrick and Stevens, 2011). Below the plume, typical salinities and temperatures near the river mouth (∼15 m water depth) were 26–33 psu and 7–12°C (Eidam et al., 2016); the ranges reflected the strong river influence.

Seabed sediments across the relict delta were typically gravel prior to dam removal, except for a zone of sandy sediment in Freshwater Bay (Warrick et al., 2008; Eidam et al., 2016). During dam removal, a new muddy/sandy deposit formed in Freshwater Bay, at the center of a periodic tidal eddy resulting from current flow around the delta headland (Gelfenbaum et al., 2015; Eidam et al., 2016). Near the river mouth, mud and sand deposited temporarily during fluvial delivery events, but were eroded within hours to days by strong tidal currents (Foley and Warrick, in press).

3.3 Methods

River discharge data were obtained from USGS gauge 12045500 (USGS, 2017). Suspended-sediment concentrations and suspended-sediment loads were obtained from USGS gauge 12046260 (USGS, 2017; Curran et al., 2014; provisional data from C. Magirl, personal communication). Atmospheric pressure data were obtained from NOAA site 9444090 (PTAW1, Port Angeles; NOAA, 2017).

Two bottom-boundary-layer (BBL) instrumented tripods were deployed near the river mouth from Nov 2013 to Apr 2014. Tripods T1 and T2 were deployed 200 m from the mouth (at ∼14 m depth) and 700 m from the mouth (at ∼23 m depth), respectively (Figures 3.1c, 3.2). T1 supported an up-looking acoustic Doppler current profiler (ADCP), an acoustic Doppler velocimeter (ADV), a down-looking high-resolution ADCP (hrADCP), an acoustic backscatter sensor (ABS), several optical backscatter sensors (OBSs), a conductivity/temperature/depth sensor (CTD), and two sediment tube traps. T2 supported two

Table 3.1: Instrument deployment schemes for the two tripods (T1 and T2). Sensor acronyms are explained in the text (see Methods). Sampling schemes are given in terms of interval between bursts (BI), sampling frequency (SF), and samples per burst (SPB) where applicable.

Sensor	Type	Elevation (cm)*	BI/SF/SPB	Bin size
T1, 48.153°N 123.567°W				
ADCP (up)	RDI Workhorse, 1200 kHz	208	30 min / 2 Hz / 360	50 cm
hrADCP (down)	Nortek Aquadopp	71	60 min / 4 Hz / 512	40 mm
ABS	Aquatec AquaSCAT 1000	90	60 min / 4 Hz / 1500	5 mm
ADV	Sontek Hydra	53	60 min / 16 Hz / 5760	-
CTD	Microcat	62.5	60 min / 16 Hz / 5760	-
OBS	Campbell Scientific	31.5	60 min / 2 Hz / 960	-
OBS	Campbell Scientific	48	60 min / 16 Hz / 5760	-
OBS	Campbell Scientific	102.5	60 min / 2 Hz / 960	-
Sed. trap	6.7 cm diameter, ∼32-cm-tall acrylic	99, 201	-	-
T2, 48.156°N 123.571°W				
ADV	Sontek Hydra	30	60 min / 16 Hz / 5760	-
Sediment tube trap	6.7 cm diameter, ∼32-cm-tall acrylic	81, 208	-	-

* Elevation is measured from the seabed to the sensor face, pressure sensor, conductivity cell, or trap opening, as applicable.

ADVs, two OBSs, and two sediment tube traps. Deployment schemes and trap dimensions are given in Table 1. Similar systems were deployed in the vicinity continuously from 2011 to 2013 (see Eidam et al., 2016).

OBS voltages were converted to mass concentrations via laboratory calibrations (see Eidam et al., 2016). Up-looking acoustic backscatter data (from the ADCP) were corrected for sound-water absorption and beam spreading per Deines (1999). Down-looking acoustic backscatter data (from the ABS) were corrected for attenuation and spreading using the algorithms described by Caine, 2007 (and references therein). ABS responses were not calibrated for sediment concentrations, given the variability in seabed grain sizes and resuspension capacity measured in this environment (see Eidam et al., 2016).

ADV pressure data were corrected by subtracting atmospheric pressure obtained from the NOAA station (see above). Elevations of various sensors were corrected for changes in bed elevation (due to sediment deposition) recorded by the ADV altimeter. Corrected pressure data and an assumed Nikuradse roughness of k_N = 3.75x10^{-4} m (based on $k_N = 2.5d_{50}$ and d_{50} = 150 μm) were used to obtain combined wave-current shear velocities (u_{*cw}) following the method given in Madsen, 1994. The z_0 estimates obtained from this method were used together with the Law of the Wall equation to extrapolate current speeds at z = 50 cm above bed, or "cmab" (u_{50}). This extrapolation allowed for comparison of velocity measurements from different time periods despite changes in bed elevation. Turbulent kinetic energy (TKE, or k) was calculated from within-burst, 16-Hz velocity data using the following standard equation:

$$k = \frac{1}{2}(\overline{(u')^2} + \overline{(v')^2} + \overline{(w')^2}) \tag{3.1}$$

where u', v', and w' are the horizontal and vertical velocity deviations from the mean current within each burst. This formulation includes deviations generated by organized motions such as waves, but in this study, k values were compared for periods of similar wave conditions before and during the event of interest.

Water and combined water-sediment densities were calculated for the boundary layer from the CTD measurements. Water densities (ρ_{w}) were calculated using standard equations of

state (Nayar et al., 2016; Sharqawy et al., 2010). Combined water-sediment densities (ρ_{ws}) were calculated from CTD data and lower OBS data (initially 32 cmab) from T1 using the following formula (e.g., Wright et al., 1986):

$$\rho_{ws} = \rho_s C + (1 - C)\rho_w \tag{3.2}$$

where ρ_{s} is the sediment density (assumed to be 2650 kg/m^3) and C is the volume concentration of sediment.

Measurements from three periods on 9 Mar 2014 were investigated for potential gravity flows. Maximum flow speeds (u_{max}) and their corresponding elevations (z_{max}) were estimated from hrADCP velocity profiles. Maximum flow thicknesses (h_{est}) were visually estimated from mid-water-column minima in hrADCP and ADCP velocity profiles. Ambient seawater density was computed based on assumed salinity, temperature, and pressure values outside the boundary layer of 30 psu, 7.5°C, and 14.8 dbar, as observed in past winter surveys (Eidam et al., 2016). A densimetric Froude number was calculated per the equation (e.g., Middleton, 1993):

$$Fr = \frac{u_{\max}}{\sqrt{\rho' g h}} \tag{3.3}$$

where g is gravitational acceleration (9.81 m/s^2) and ρ' is the density anomaly of the flow relative to the ambient fluid, i.e.,

$$\rho' = \frac{\rho_{ws} - \rho_w}{\rho_w} \tag{3.4}$$

Seabed erosion rates were estimated for comparison to actual erosion of the new deposit in mid-late Mar 2014. A dry density (ρ_{dry}) was estimated from the upper 13-14 cm of the lower sediment trap on T1 using the following equation (Allersma, 1988 in Winterwerp and van Kesteren, 2004):

$$\rho_{dry} = 480\alpha_c + (1300 - 280\alpha_c)(\zeta^{sa})^{0.8} \tag{3.5}$$

where α_{c} is a consolidation coefficient ranging from 0 to 2.4 (for fresh to old deposits), and ζ^{sa} represents the sand fraction (in percent). A value of 0 was assumed for α_{c}, yielding $\overline{\rho_{dry}}$ of 1180 kg/m^3 for measured sand fractions of 84–94%. The erosion rate (E, kg/m^2/s) was

calculated following an equation given by Torfs et al., 2001:

$$E = E_1 exp(-\kappa \tau_c^{\chi})(\tau - \tau_c) \tag{3.6}$$

where τ is the measured shear stress, τ_c is the critical shear stress needed for erosion, and E_1, κ, and χ were determined experimentally to be 0.25, 8, and 0.5, respectively (Torfs et al., 2001). A time series of τ was determined from u_{*cw} according to the standard equation:

$$\tau = u_*^2 \rho_w \tag{3.7}$$

The estimated erosion rate (E) was calculated for an assumed value of τ_c, and the results were divided by the calculated $\overline{\rho_{dry}}$ from the sediment trap and multiplied by 3600 s to determine the depth of erosion between each measurement. This depth was compared to the change in bed elevation measured by the ADV altimeter. A value of $\tau_c = 0.195$ Pa was then determined iteratively such that the mean measured and predicted bed elevation changes were equal for 10 Mar to 28 Mar.

Shipek grab samples of the seabed were collected in Nov 2013 and Apr 2014 near the river mouth and in Freshwater Bay. Sediments from tripod tube traps and shipek grab samples were processed for grain-size distributions. Samples containing less than a few percent mud were dried and sieved. Samples with more than a few percent mud were rinsed through a 63-μm sieve using 0.05% $NaPO_3$ to separate sand from mud. Most mud fractions were processed in a Micromeritics Sedigraph (particle-size analyzer); mud fractions from Apr 2014 shipek grab samples were processed by the pipette method at a remote field station as part of an experiential learning course. Sand fractions were sieved or processed in a settling column. The settling column was a 192-cm-long water-filled acrylic cylinder containing a plate suspended from a scale connected to a computer. Sand subsamples were released into the column at a known starting time, and the change in plate weight was recorded. Mass fractions of sand and coarse silt (2000 μm to 32 μm) were determined using the time-series of weight measurements, the fall distance within the column, and Gibbs' settling velocity equation (Gibbs et al., 1971) for turbulently settling particles. Total mud and sand grain-size data were then binned into whole-phi increments.

3.4 Results

3.4.1 River discharge and delta change

River discharge was <100 m^3/s for most of winter 2013–2014. The flood event of 6–9 Mar 2014 was characterized by discharge peaks of 270–350 m^3/s, and SSC peaks of 19.8 g/L on 6 Mar and 14.3 g/L on 9 Mar (Figure 3.2; USGS, 2017; C. Magirl, personal communication). Total suspended load measured from 6 to 9 Mar 2014 was ∼880,000 tonnes (C. Magirl, personal communication). During the winter, the nascent river-mouth delta prograded several tens of meters seaward (Stevens et al., 2017a, 2017b; Figure 3.3). During the 6–9 Mar 2014 flood, the river mouth scoured a new outlet just west of T1 (Figure 3.2; A. Ritchie, personal communication).

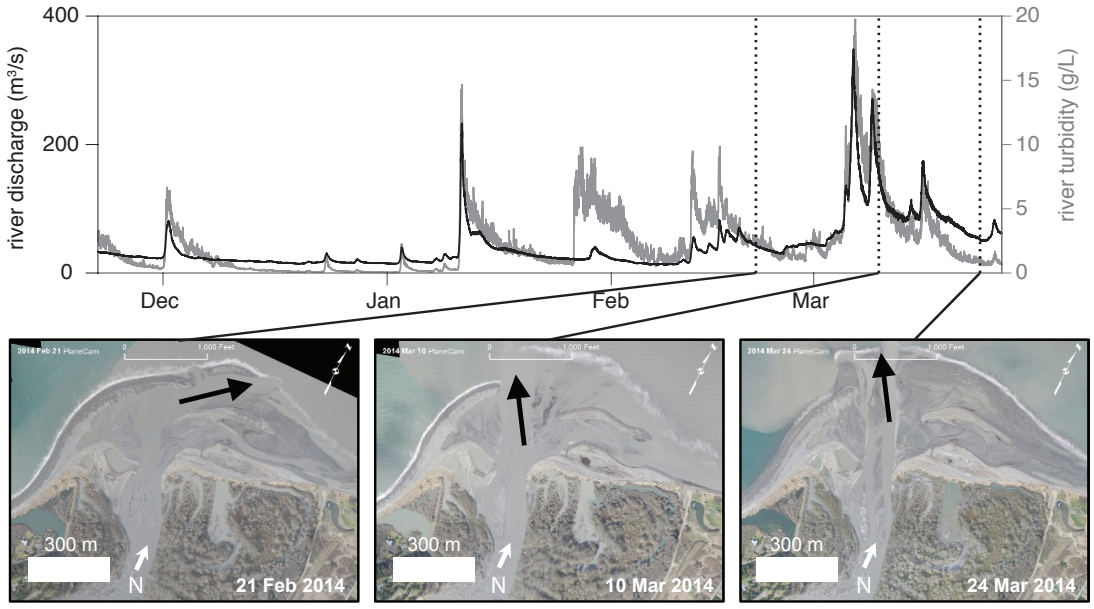

Figure 3.2: Photos and time-series plots highlighting growth of a new river-mouth deposit. a) River discharge and turbidity (USGS, 2017) during the tripod deployment reported in this study. b) Aerial photographs of the growing river-mouth deposit on 21 Feb 2014 (left), 10 Mar 2014 (center), and 24 Mar 2014 (right); arrows denote major river outlets (modified from A. Ritchie, personal communication).

3.4.2 Water and sediment dynamics at T1 before, during, and after the 6-9 Mar 2014 event

During 6-9 Mar 2014, temperatures, salinities, boundary-layer densities, vertical velocities, and current speeds at T1 changed appreciably relative to winter 2013–2014 background values (Figure 3.4). Salinities decreased from ∼32 to ∼22–27 psu and temperatures warmed from ∼7.8°C to 9.0°C (Figure 3.4b). Boundary-layer ρ_w decreased from ∼1025 to ∼1017 kg/m^3, and ρ_{ws} increased from ∼1026 to ≥1037 kg/m^3 (Figure 3.4c). Vertical velocities

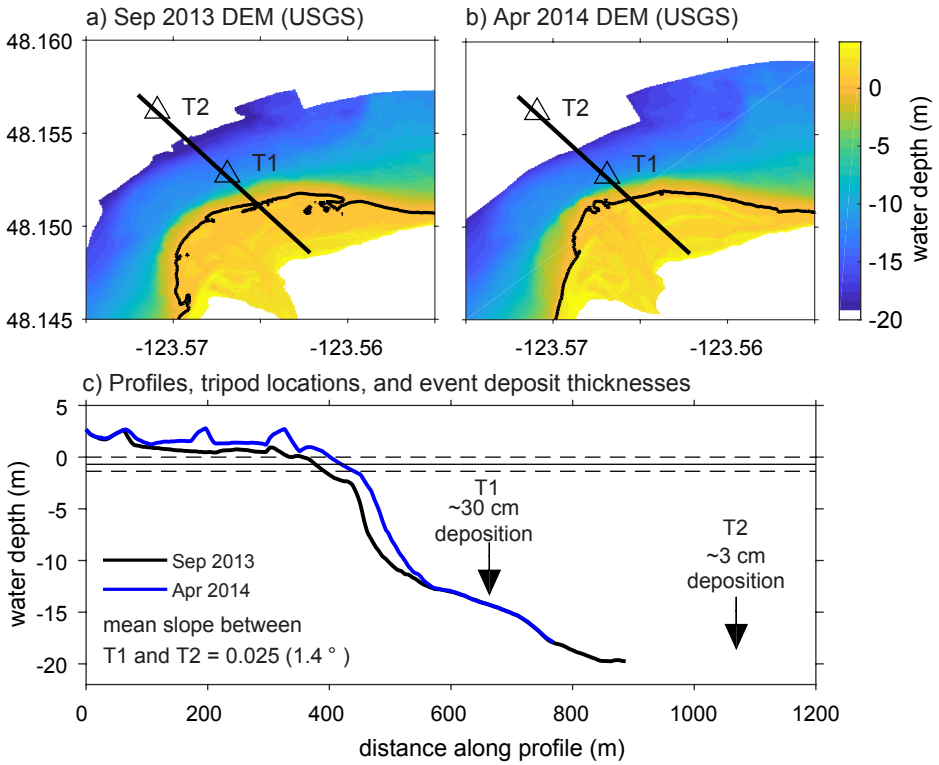

Figure 3.3: Bathymetry and instrument locations. a) Bathymetry from Sep 2013, with Nov 2013–Apr 2014 tripod sites. b) Bathymetry from Apr 2014 with tripod sites. c) Bathymetry profiles from the transect lines shown in a) and b). Approximately 30 cm and 3 cm of sediment were deposited at T1 and T2, respectively, between Feb and Mar 2014. Black contour lines in (a) and (b) represent 0 m water depth at the outer shoreface. In (c), the solid horizontal line is mean sea level (MSL), and upper and lower dashed lines are mean higher high water (MHHW) and mean lower low water (MLLW), respectively. Bathymetry data are from Stevens et al., 2017a, 2017b.

throughout the water column were anomalously negative (downward) for several hours on 9 Mar (-0.01 to -0.03 m/s) (Figure 3.4d). Wave energy was moderate throughout the winter and the event (maximum significant wave heights were 1.6 m with mean value of 0.42 m; not shown). Current speeds and calculated TKE were reduced relative to background values for several days beginning on 7 Mar (Figure 3.4e), though the wave climate was similar to the pre-event conditions. On 9 Mar, the bed elevation increased by >15 cm at T1, and ∼3 cm at T2 (Figure 3.4f).

Boundary-layer (and water-column) dynamics on 9 Mar were distinctly different between two time periods: stage 1 (08:00 to 12:00) and stage 2 (13:00 to 18:00). During stage 1 (light gray region in Figure 3.5), the water surface elevation began to fall, and currents were weak (Figure 3.5a, b). Water-column backscatter signals were relatively weak (Figure 3.5e). A few centimeters of bed aggradation occurred (Figure 3.5f), and SSC reached values of ∼1 g/L and >10 g/L at the upper and lower OBSs, respectively (Figure 3.5g). Total u_{*cw} was between 0.01 and 0.02 cm/s (Figure 3.5h). During stage 2 (dark gray region in Figure 3.5), the water level reached a minimum (∼1.6 m lower than at 08:00), and along-isobath currents began accelerating. A strong backscatter signal propagated upward from the boundary layer to fill nearly the entire water column by 18:00. The bed aggraded by more than 10 cm, and SSC at both OBSs decreased abruptly. Total u_{*cw} was 0.02-0.03 cm/s. During both stages, wave energy was relatively weak and vertical velocities were generally downward (Figure 3.5c, d)

Within days of the event, salinities returned to pre-event levels. By early April, the deposits at T1 and T2 had eroded and bed elevations had returned to roughly pre-event levels (Figure 3.4g).

3.4.3 Velocity and backscatter profiles (9 Mar 2014)

Sediment-gravity flows are often manifest by anomalously large near-bed current speeds and sediment concentrations. For most of winter 2013–2014, and for "typical" periods on 9 Mar (see Figure 3.6), velocity profiles exhibited characteristic logarithmic decay. At 03:00, 09:00,

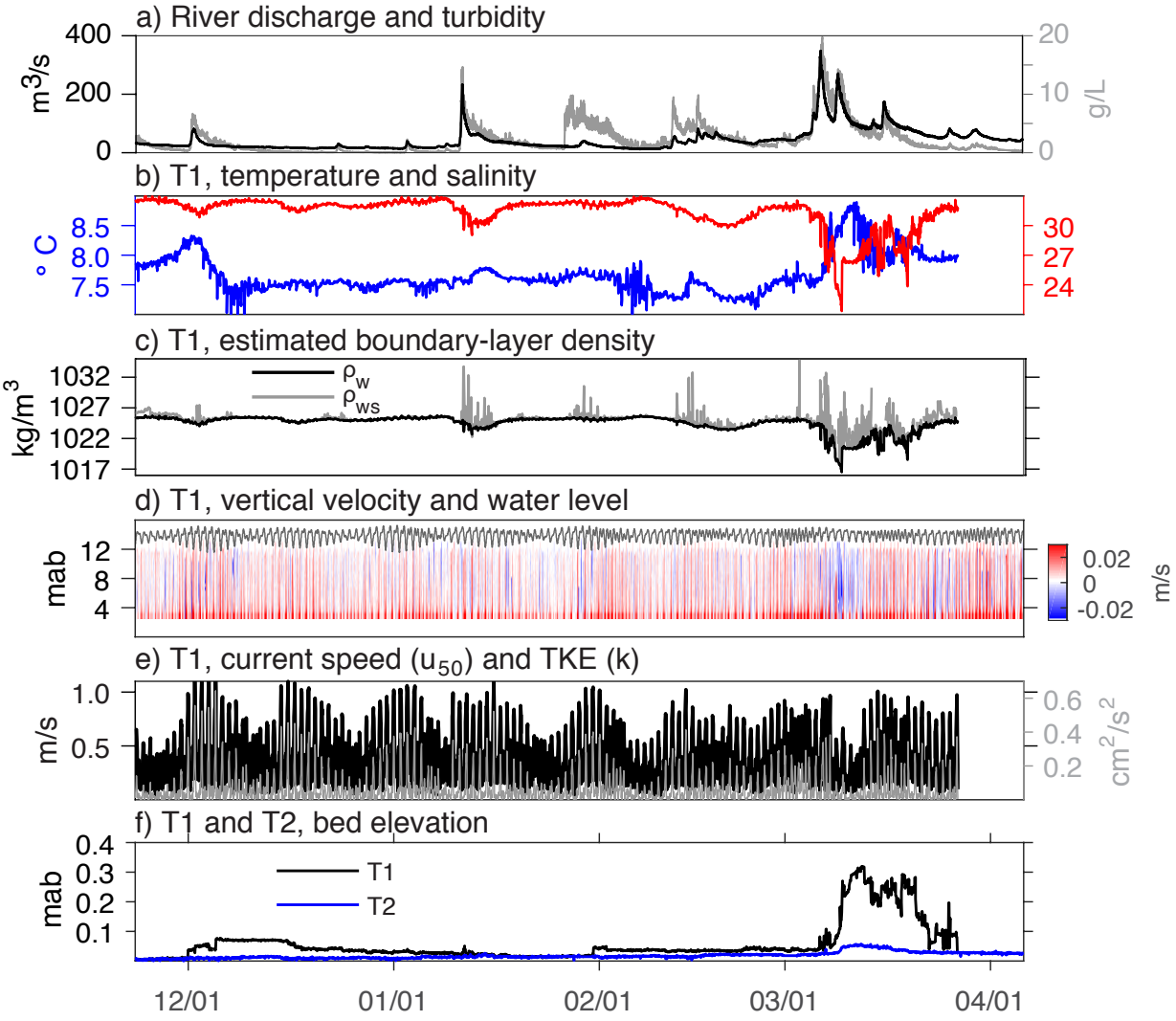

Figure 3.4: Four-month time-series measurements collected at T1 and T2 during winter 2013–2014. a) River discharge and turbidity (USGS, 2017). b) Temperature and salinity at T1. c) Boundary-layer water density (ρ_{w}) and water/sediment density (ρ_{ws}). d) Vertical velocity measured by the up-looking ADCP at T1. e) Current speed extrapolated to 50 cmab and TKE at T1. g) Bed elevation at T1 and T2 (from ADV altimeter).

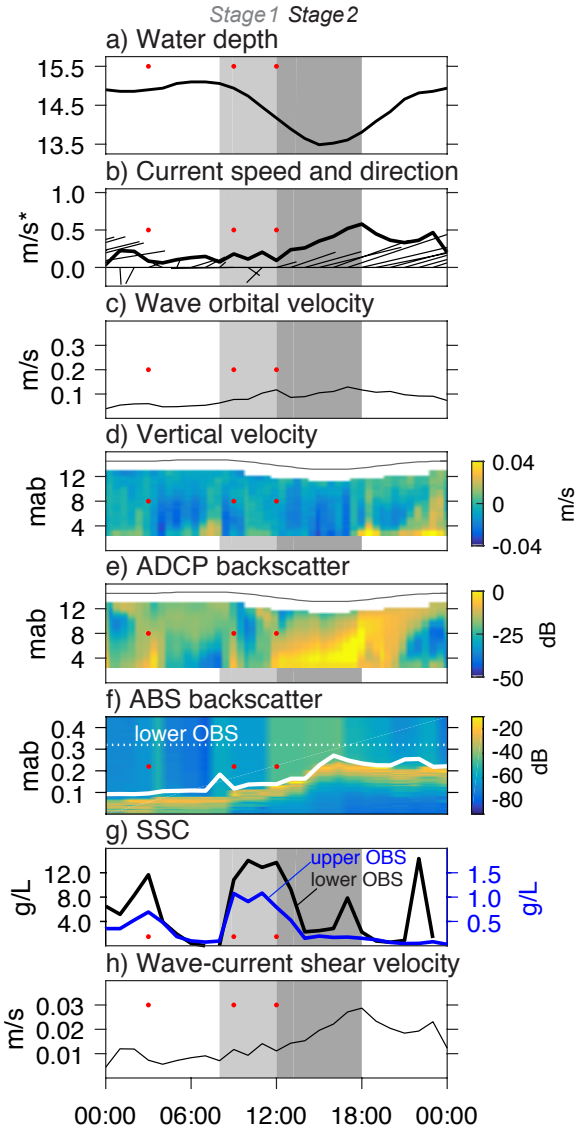

Figure 3.5: Detailed time-series measurements at T1 from 9 Mar 2014. a) Water depth. b) Current speed (dark line) and unscaled direction (flows between 12:00 and 18:00 are along-isobath). c) Wave-orbital velocity. d) Vertical velocity. e) ADCP backscatter. f) ABS backscatter (elevation of lower OBS is noted). g) SSC, upper OBS (∼100 cmab) and lower OBS (∼32 cmab). h) Wave-current shear velocity (u_{*cw}) calculated using a sensor elevation corrected for bed aggradation. Red dots mark times 03:00, 09:00, and 12:00 (see Figure 3.6). Two time periods (08:00–12:00/12:00–18:00) are highlighted in light/dark gray across all panels, corresponding to times of intense SSC in the boundary layer and/or water column.

Table 3.2: Gravity-flow properties on 9 Mar. U_{max} and z_{max} are the magnitude and elevation of the maximum boundary-layer flow speed, respectively. H_{est} is the estimated flow thickness, ρ_{ws} is the flow density, and $\rho_a{}^*$ is the assumed ambient seawater density. Fr_d is the densimetric Froude number, calculated from the adjacent parameters. SSC are given for two elevations. Parameter Δz_{bed} is the change in bed elevation since the previous entry.

Time	u_{max} (m/s)	z_{max} (m)	h_{est} (m)	ρ_{ws} (kg/m^3)	ρ_a* (kg/m^3)	estimated Fr_d	SSC (g/L) ~20 cmab	SSC (g/L) ~90 cmab	Δz_{bed} (cm)
9 Mar 3:00	0.11	0.30 m	≤4 m	1025.2	1023.5	0.43	11.7	0.69	0.33 cm**
9 Mar 9:00	0.18	0.36 m	≤5 m	1024.2	1023.5	0.98	10.8	1.08	2.21 cm
9 Mar 12:00	0.09	0.26 m	≤3 m	1025.6	1023.5	0.37	13.7	0.79	2.11 cm

* Computed from assumed salinity, temperature, and pressure of 30 psu, 7.5°C, and 14.8 dbar, respectively
** Referenced to 9 Mar 0:00

and 12:00, there were local maxima in velocity and backscatter near bed (Figure 3.6). These anomalous flows were all less than ∼5 m thick, and thickness roughly scaled with u_{max} (Table 3.2). The flows had excess densities of 0.7–2 kg/m^3. Fr_d was nearly supercritical (i.e., ∼1) only for the 09:00 event. SSCs from the lower OBS were inversely related to u_{max}.

Another expected signature of gravity flows is anomalous down-slope current flow. Typically, currents at the T1 site flowed along-isobath (see examples from 9 Mar at 06:00, 08:00, and 16:00 in Figure 3.6), except during periods of tidal phase change and very slow current speeds. At 03:00 and 12:00 on 9 Mar, currents were weak and along-isobath, but flowed in nearly opposite directions between the upper water column and boundary layer. At 09:00, currents flowed down-slope within ∼6 m of the bed, whereas currents in the upper water column flowed along-isobath (Figure 3.6).

Acoustic backscatter data have also been used in previous studies to identify muddy gravity-flow layers, manifested as weak returns in place of a strong seabed signal. On 9 Mar, relatively weak ABS returns were observed at 03:00 and 06:00–15:00 (Figure 3.7). It is also worth noting that within 0.5 m of the bed, velocity profiles were approximately logarithmic during all of these times (Figure 3.7).

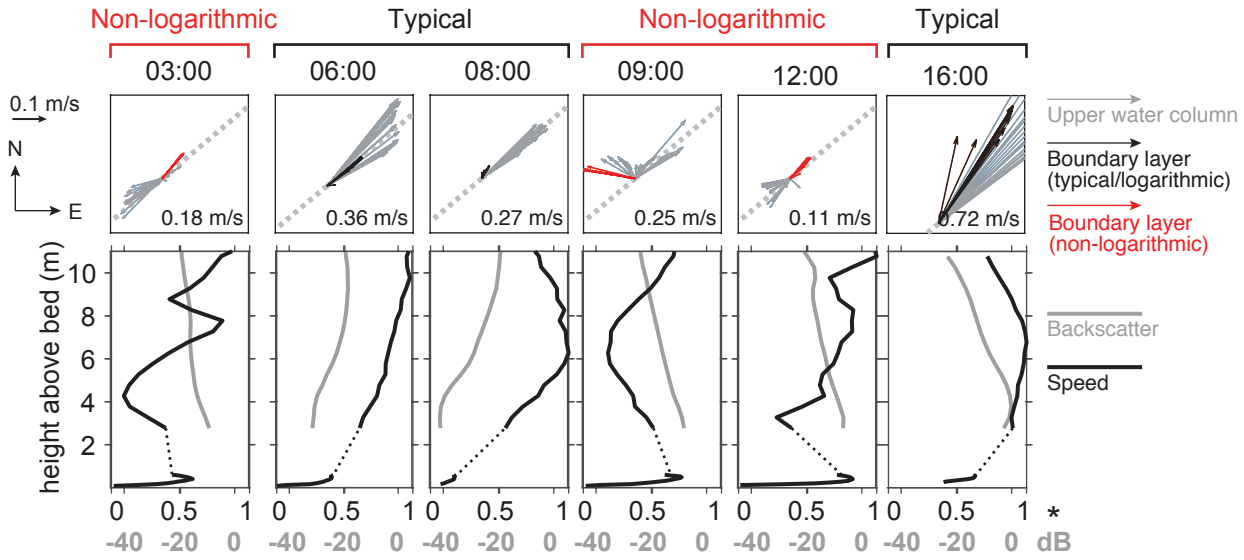

Figure 3.6: Hourly water-column speed and backscatter data from 9 Mar 2014. Vector plots (top row) represent water-column (gray) and boundary-layer (black) current velocities, in east/north coordinates. Red vectors are boundary-layer flows thought to represent gravity flows (at 03:00, 09:00, and 12:00). Gray dashed lines represent the along-isobath direction, and noted speeds are maximum values for each time period. Line plots (bottom row) represent water-column profiles of current speed (black) and backscatter (gray). Local near-bed velocity maxima occurred at 03:00, 09:00, and 12:00. (*Speeds normalized to the maximum value for each profile.)

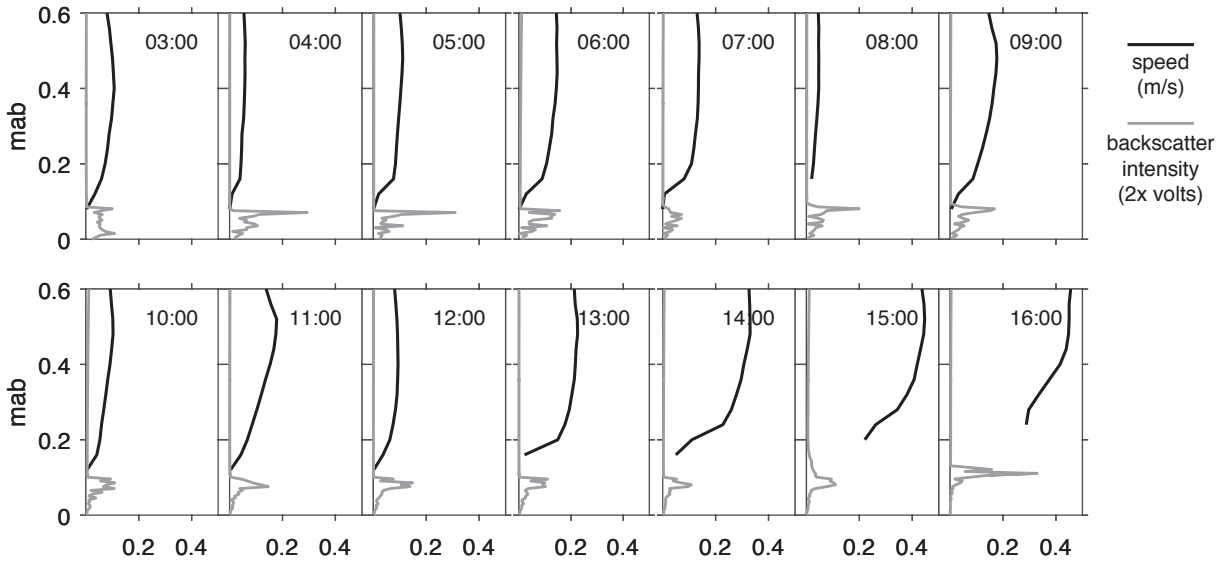

Figure 3.7: Hourly near-bed speed and backscatter profiles from 9 Mar 2014. Speed profiles (from the hrADCP) vary in magnitude according to tidal phase; hours 03:00, 09:00, and 12:00 are interpreted to be gravity-flow periods (see Figure 3.6). Sharp backscatter peaks (from the ABS) occurred at 04:00, 05:00, 08:00, and 16:00, and indicate a hard return from a solid bed. During the remaining times, weaker, diffuse returns probably indicate abundant sediment in transport near the bed.

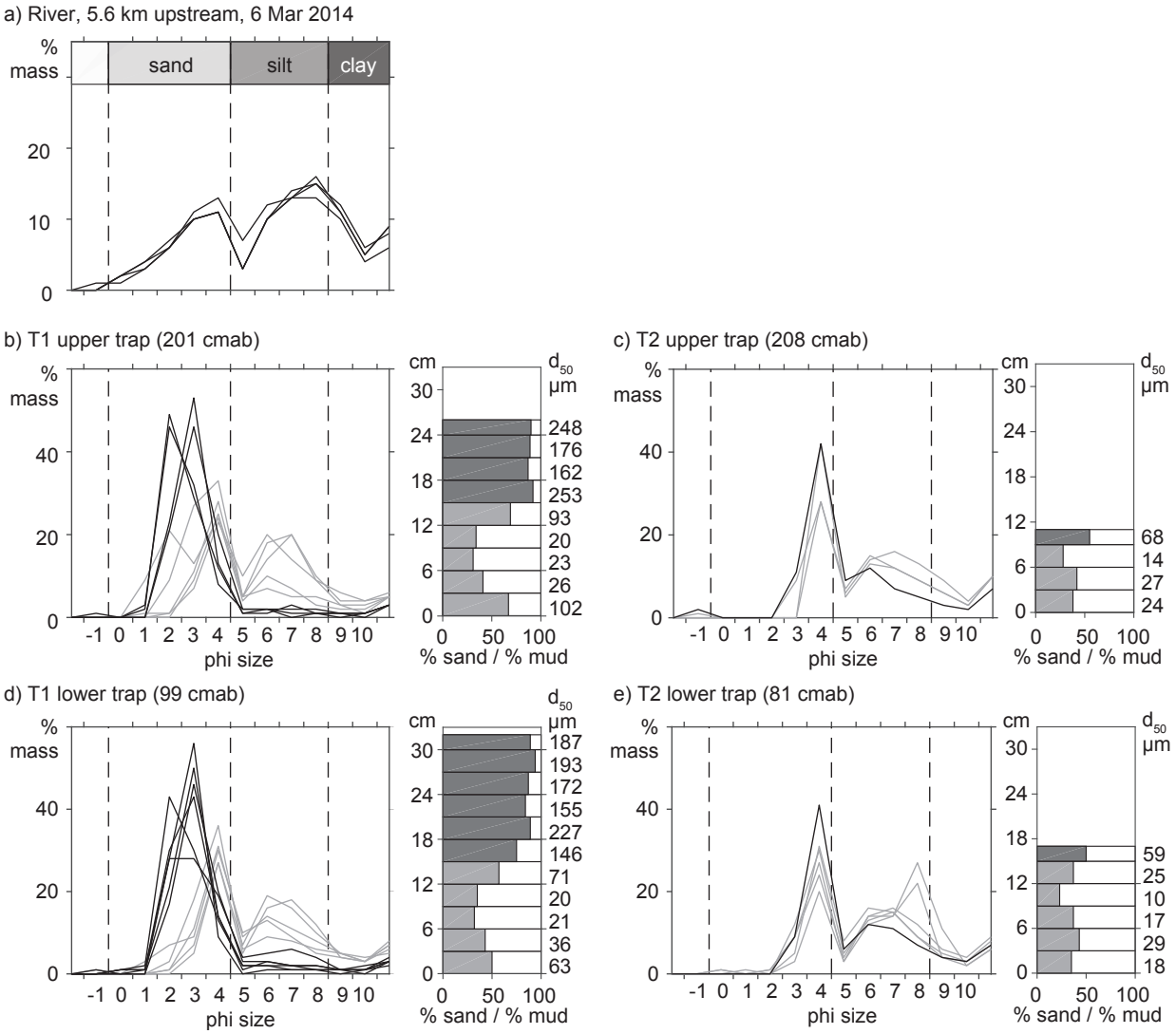

Figure 3.8: Grain-size distributions from the Elwha River and sediment traps. a) Grain-size distributions from suspended-sediment samples collected in the Elwha River by USGS (2017) at gauge 12046260 on 6 Mar 2014. b-e) Grain-size distributions from the tripod sediment traps. For each trap, mass frequency plots are given at left, and down-core sand/mud distributions, together with median grain size, are given for each 3-cm subsample at right. Light gray lines/sections denote muddier samples, which are interpreted as pre-event (pre-March 2014) sedimentation. Dark gray lines/sections denote sandier samples, interpreted as event (early Mar 2014) sedimentation.

3.4.4 Sediment-trap grain sizes

The sediment traps mounted at ∼100 and 200 cmab on T1 were full or nearly full upon retrieval one month after the event, in contrast to prior deployments of similar duration (see Eidam et al., 2016). Sediment in the lowest 12–15 cm of both traps was composed of 50–75% mud, and was characterized by bimodal size distributions (modal sizes were very fine sand and medium/fine silt). The upper portions of both traps contained well-sorted, dominantly medium or fine sand (Figure 3.8). The traps from T2 contained <18 cm of sediment, and all but the uppermost interval was composed of dominantly muddy sediment. Like the muddy portions of the T1 traps, these sediments were bimodal, and had peaks in the very fine sand and fine/very fine silt ranges. The uppermost 1–2 cm of each trap contained well-sorted, very fine sand.

3.4.5 Shear stresses and erosion rates after the event

After the event, maximum τ was ∼1–2 Pa and maximum E was 0.017 kg/m^2/s (Figure 3.9a, b). Erosion rates fluctuated on tidal cycles. Maximum actual and predicted erosion depths were ∼0.15 and 0.037 m, respectively, between measurements (Figure 3.9c, d).

3.4.6 Seabed grain sizes

The spatial distribution of grain sizes near the river mouth and in Freshwater Bay changed little between Nov 2013 and Apr 2014 (Figure 3.10). Muddy and sandy sediments were generally confined to Freshwater Bay, where median sizes fined somewhat from coarse/medium silt to fine/very fine silt. Gravels (equal to or coarser than -1 ϕ or 2 mm; Wentworth, 1922) were dominant east of T1 and T2. At T1 and T2, median sediment sizes coarsened somewhat between Nov 2013 and Apr 2014, from gravel and very coarse sand to gravel (Figure 3.10).

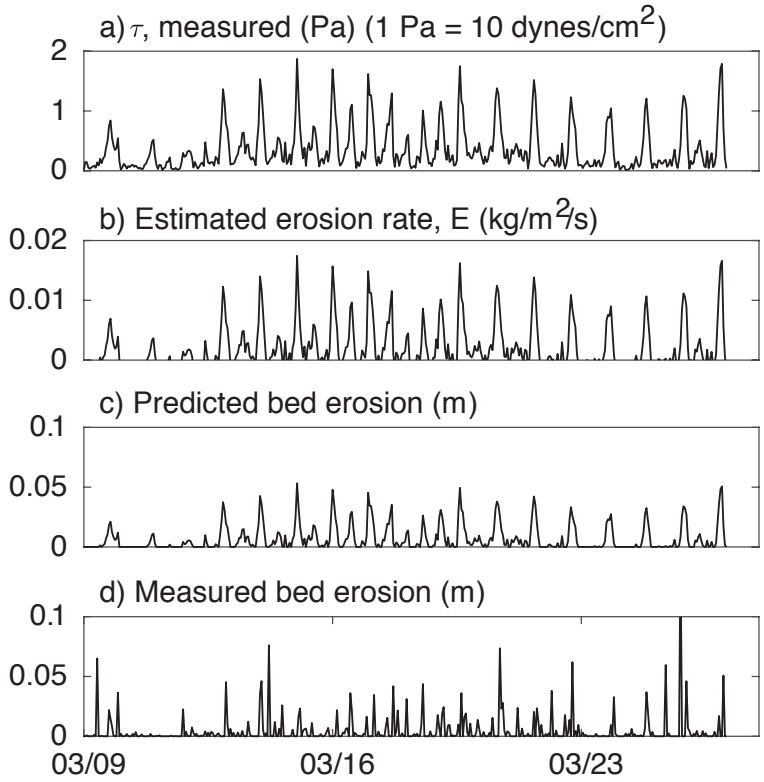

Figure 3.9: Post-event erosion parameters. a) Calculated shear stress. b) Estimated erosion rate. c) Predicted bed erosion depth. d) Measured bed erosion depth.

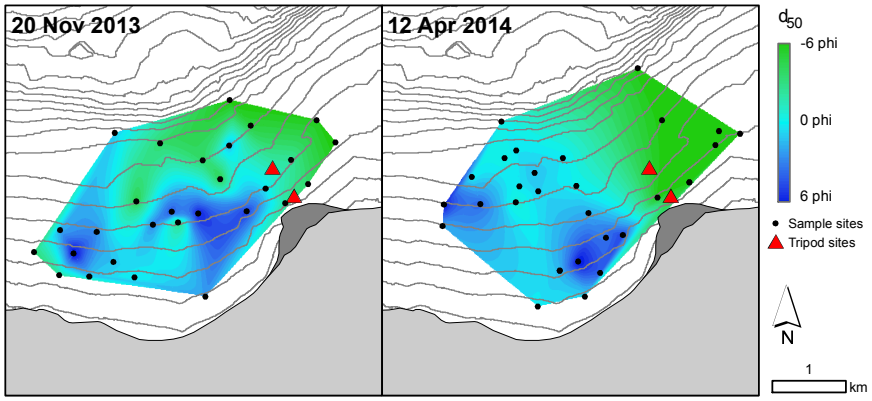

Figure 3.10: Distributions of median grain sizes (d_{50}) from Nov 2013 (left) and Apr 2014 (right). Shaded areas represent interpolations made from point measurements (locations shown). Sites that were too coarse to sample were assigned a d_{50} value of -6 ϕ (gravel, 64 mm). Some fining occurred in Freshwater Bay during winter 2013–2014. Areas near the tripod sites remained coarse (very coarse sand to gravel).

3.5 Discussion

The 9 Mar 2014 event was likely a hyperpycnal flow (or series of flows) that had a short runout distance and was extinguished within a few hours, resulting in the deposition of >15 cm of sandy sediment at the toe of the new river-mouth delta. Here we discuss the mechanics of the flow, possible mechanisms of extinction, and context within the literature of observed gravity flows and their deposits. Post-even erosion of the deposit is also addressed.

3.5.1 Punctuated hyperpycnal flows

The three events that occurred at 03:00, 09:00, and 12:00 on 9 Mar exhibited characteristics of hyperpycnal flows. Boundary-layer flow was directed downslope or opposite to the overlying flow (Figure 3.6), and there was evidence of local, near-bed maxima in velocity profiles (Figure 3.6), characteristic of gravity flows (Kneller et al., 1999). Each event was accompanied by near-bed SSC >10 g/L, which is the critical value commonly cited for fluid muds (e.g., Ross and Mehta, 1989). The measurement at 09:00 likely represented the only

period of supercritical flow. Previous studies have suggested that supercritical flows on steep slopes (>1.15°) are particularly susceptible to mixing/entrainment at the upper interface (e.g., Bowen et al., 1984; Stacey and Bowen, 1988; Sequeiros et al., 2010). The steep slopes near the instrument site (1.4° to >10°) and strong backscatter signals in the lower and middle water column during all three events (Figure 3.5e) suggest that mixing may have been active, and thus could have helped extinguish the flow, accounting for the brief duration.

Stage 1 processes may have represented direct hyperpycnal plumes. On 6 Mar, fluvial SSC was up to 14.2 g/L (C. Magirl, personal communication), i.e., less than the commonly cited critical value of 35–45 g/L but still substantial. Some studies have suggested that the critical value for plunging may be lower (∼6–12 g/L, McCool and Parsons, 2004), and that saltwater entrainment within a river mouth may reduce the SSC needed for plunging by up to two orders of magnitude (e.g., Felix et al., 2006). The intertidal topset of the new delta (Figure 3.2) may have provided a space for saltwater entrainment at high tide before the effluent plunged at the foreset. Excess boundary-layer densities (i.e., ρ_{ws} minus ρ_a) observed during the events were small but positive (∼0.7–2.1 kg/m^3). Vertical velocities at T1 were generally downward, suggesting plunging flow, but the backscatter signal confounds this observation because the turbidity signals generally spread upward from the boundary layer rather than downward from a surface plume (Figure 3.5d, e). Thus, if plunging did occur, it must have occurred <200 m from shore; Lamb and Mohrig (2009) note that plumes which can spread laterally (like the Elwha plume) and discharge over steep slopes tend to plunge closer to shore, but the distance scale is not well constrained. In short, fluvial SSC, boundary-layer SSC, and velocity data from stage 1 step support the formation of a brief hyperpycnal plume (conceptualized in Figure 3.11a), but more comprehensive density profiles would be needed for confirmation.

3.5.2 Sustained boundary-layer transport, stage 1

While the three punctuated events at 03:00, 09:00, and 12:00 displayed the strongest characteristics of hyperpycnal plumes, intense BBL SSC and ongoing bed aggradation of several

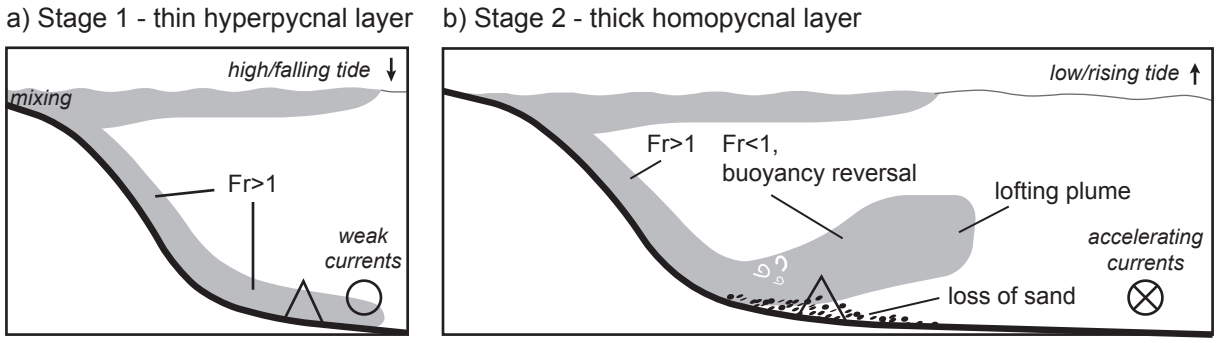

Figure 3.11: Conceptual diagrams of stage 1 and 2 processes on 9 Mar 2014. a) Stage 1: thin, supercritical, hyperpycnal layer, and downslope transport of fine sediment during high/falling tide. b) Stage 2: thick, subcritical, homopycnal layer, and deposition of sand during low/rising tide.

cm persisted from 08:00 to 12:00 on 9 Mar (Figure 3.5). Because this period coincided with falling water levels (Figure 3.5a), near-bed SSC >10 g/L (Figure 3.5g), weak upper-water-column backscatter (Figure 3.5e), and bed aggradation of several cm, it likely represented sustained down-slope flow of dominantly sandy sediment. By analogy, gravity flows were commonly observed during falling water at the Squamish Delta, and attributed to tidal unloading and subsequent failure of unstable, freshly deposited delta-lip sediments (Clare et al., 2016). Gravity flows have also been attributed to delta-front failures in a variety of other environments, as well as to resuspension of temporarily deposited flood sediments within a river mouth (e.g., Plink-Björklund and Steel, 2004; Piper and Normark, 2009). Both failure of unstable delta-front sediments and resuspension of temporarily stored sediments are likely triggers for this period of sustained turbidity and deposition in the Elwha case. These are implied by the tidal water-level decrease between 08:00 and 12:00 (Figure 3.5a), intense sediment delivery of the preceding three days (Figure 3.2a), and the dynamic nature of the river-mouth channel (Figure 3.2b). Furthermore, the concept of a sustained, downslope sandy flow is supported by the strong but localized (near-bed) SSC signal, consistent with observations and models of sandy underflows being thinner and more concentrated than

muddy flows (Bowen et al., 1984). Also, the runout distance of a gravity flow depends on the proportion of fine versus coarse sediment (Alexander and Mulder, 2002), and a sandy flow would be consistent with the apparently short runout of the 9 Mar event evident in the sharp deposition gradient (>15 cm at T1 versus ∼3 cm at T2 located 500 m down-slope; Figure 3.4f).

3.5.3 Sustained boundary-layer transport, stage 2

The punctuated event at 12:00 on 9 Mar marked a change in BBL dynamics from the thin, concentrated BBL flow of 08:00–12:00 (stage 1) to a much thicker, less concentrated flow from 13:00–18:00 (stage 2; Figure 3.5). This period was characterized by accelerating, along-isobath tidal currents, strong downward vertical velocities, a strong upward-propagating backscatter signal, substantial bed deposition, and relatively small values of near-bed SSC (Figure 3.5). It should be noted here that the near-bed ABS response intensified during this time, in contrast with the SSC signal; this apparent contradiction is attributed to a coarsening in near-bed suspended sediments and differing properties of optical and acoustic sensors (acoustic sensors are more responsive to larger particles than optical sensors; Lynch et al., 1994). The bed-aggradation and sediment-trap data suggest rapid down-slope transport and deposition of sandy sediment, while the water-column backscatter suggests lofting of finer sediment, and overall deterioration of the flow. Together, these dynamics of flow extinction suggest a combination of three process: a hydraulic jump, a lofting hyperpycnal plume experiencing buoyancy reversal, and the transition from a negatively buoyant hyperpycnal plume to neutrally buoyant homopycnal plume due to mixing at the upper interface (Figure 3.11). Each mechanism is discussed separately here, though they all share similar signatures and likely occurred simultaneously.

Sediment flowing down the foreset of the delta during stage 1 may have formed a super-critical flow owing to the extremely steep slopes (3-10°; Figure 3.11a). During stage 2, the flow was subcritical at T1, i.e., at the point where the seabed slope decreased (see Komar, 1971 and Sequeiros et al., 2009 for discussion of slope impacts on gravity flows). A transi-

tion from supercritical to subcritical would have necessitated a hydraulic jump (e.g., Garcia, 1993; Figure 3.11b). In general, coarser sediments are rapidly deposited at a jump, owing to the reduced carrying capacity of the flow in spite of increased turbulence; meanwhile, finer sediments may remain suspended beyond the jump (e.g., Garcia, 1993; Kneller and Buckee, 2000). The presence of a hydraulic jump near T1 from 12:00 to 18:00 is well supported by the data. Sand deposited rapidly in conjunction with a sharp decrease in near-bed SSC, despite increasing bed stresses (Figure 3.5h). This suggests decreased carrying capacity of the flow, which would have been amplified by its deceleration as more sediment settled. At the same time, a strong backscatter signal was observed in the middle water column, suggesting upward turbulent mixing of fine suspended sediment (Figure 3.5e). This was likely caused by accelerating tidal currents (Figure 3.5b) and/or thickening of the gravity flow at the supercritical-subcritical transition.

Stage 2 boundary-layer and water-column dynamics also exhibit characteristics of a lofting hyperpycnal plume, i.e., a negatively buoyant plume experiencing buoyancy reversal due to deposition of sediment and loss of excess density (Figure 3.11b; e.g., Kneller and Buckee, 2000; Stevenson and Peakall, 2010; Gladstone and Pritchard, 2010; Pritchard and Gladstone, 2009). In this type of process, deposition of some sediment allows a negatively buoyant plume to become positively buoyant, because the sediment needed to provide excess density in seawater has been lost. This is thought to produce sediment sorting, because sand deposits rapidly (resulting in the buoyancy reversal), while fine sediments remain suspended in the rising plume and deposit elsewhere. This mechanism has been used to explain "deep-water massive sands," structureless sand bodies (i.e., deposits not produced by bedload transport) found at transitions between continental slopes and continental rises (e.g., Gladstone and Pritchard, 2010). Lofting hyperpycnal plumes have also been invoked for the formation of 5–40-cm-thick, well-sorted sand lobes in the Santa Barbara channel (CA), located seaward of several high-yield small mountainous rivers (Steel et al., 2016). In the Elwha example, the slope transition may have reduced the sand-carrying capacity of the flow, and/or accelerating tidal currents may have introduced sufficient turbulence to destroy any flow stratification,

allowing rapid deposition of well-sorted sands (Figures 3.5f, 3.8) and lofting of finer sediments (Figure 3.5e).

Whether a hydraulic jump or lofting plume was the dominant mechanism of flow extinction (or both mechanisms occurred simultaneously), in stage 2 the flow lost its identity as a hyperpycnal (negatively buoyant) plume and became a homopycnal (neutrally buoyant) plume filling most of the water column. The flow may have lost its momentum and identity as a gravity-driven boundary-layer flow due to waning supply, deposition of sediment at the toe of the delta slope, and/or mixing at the upper interface by accelerating, along-isobath tidal currents (Figures 3.5b, 3.6, 3.10d). This combination of deposition, saltwater entrainment, and upward mixing in strong tidal flow would have eliminated the positive density anomaly, allowing the flow to become neutrally buoyant (Figure 3.11b; see Bates, 1953) and sediment to be advected far from the river mouth.

3.5.4 Post-event seabed changes

In the three weeks following the 6–9 Mar flood, the deposits at T1 and T2 were almost completely eroded (Figure 3.4f) by strong tidal-current flow. The estimated critical shear stress for erosion (τ_c) was similar to values measured by Mitchener and Torfs (1996) for mixed sand/mud beds with bulk densities of 1200–1600 kg/m^3, and fell between critical values used by Wiberg et al., 1994 to characterize mean sediment sizes of 130 μm (0.16 Pa) and 230 μm (0.22 Pa). The estimated τ_c thus seems reasonable for a seabed composition represented by the sediment-trap samples. It is unsurprising that this value is greater than many estimates of cohesive bed erosion thresholds (e.g., 0.11–0.50 Pa, Amos et al., 1997), given that mixtures of sand and mud tend to be less erodible than mixtures of either constituent size class (e.g., Mitchener and Torfs, 1996).

Predicted erosion rates were comparable to those measured for sand/mud mixtures in laboratory tests (Mitchener and Torfs, 1996) and generally an order of magnitude greater than those measured for cohesive beds at the Fraser Delta in the nearby Strait of Georgia (Amos et al., 1997). Because of high erosion rates driven primarily by tidal currents, the

deposit at T1 effectively disappeared within 3 weeks of the event. Larger-scale mapping of seabed sediment sizes offshore of the Elwha Delta and in Freshwater Bay also revealed little size/textural change during winter 2013–2014. Thus, almost no record of this major discharge event and gravity flow was preserved. This is surprising in light of the muddy flood deposits found seaward of other small mountainous rivers (e.g., Eel River, Sommerfield and Nittrouer, 1999; Waipaoa River, Carter et al., 2010), and the coarse sizes of the event deposit. In this tidally energetic system, currents provide sufficient shear stress to remove even an erosion-resistant muddy sand deposit.

3.5.5 Implications

The occurrence of limited gravity-flow activity between fall 2011 and spring 2015 (despite intense fluvial sediment loading) and the nearly complete erosion of the Mar 2014 event deposit highlight the difficulty in forming gravity flows, and preserving their deposits. Though the Mar 2014 flood was accompanied by fluvial SSC >10 g/L and may have formed a hyperpycnal plume, much of excess density was supplied by sand, which rapidly settled at the base of the river-mouth delta during a period of strong tidal flow. Tidal currents are known to initiate, re-direct, and extinguish gravity flows in other environments (e.g., Huanghe, Li et al., 1998; Eel shelf, Imran and Syvitski, 2000). In the Elwha case, tidal currents likely interrupted the flow and induced mixing at the upper interface, a process amplified by the rapid deposition of sand and associated loss of flow density/identity. The result was a very brief flow with short runout distance. The sandy nature of the flow also suggests the triggering mechanism may have been erosion of bed material from the face of the new river-mouth deposit, in contrast to traditional models of plunging, muddy plumes.

While the Elwha event may be an example of processes that form massive sand deposits, it also highlights uncertainties about the prevalence and persistence of sandy hyperpycnal plumes. Hyperpycnal plumes are generally associated with high-yield rivers which discharge high concentrations of mud during floods; however, during some floods, much of the fluvial load may comprise sand. Because sand settles rapidly, gravity flows may be less likely to form

(or have shorter runout distances) than expected, and thus the frequency of hyperpycnal plumes predicted by rating curves may be over-estimated. Alternatively, the erosion of the sandy deposit in the tidally energetic Strait of Juan de Fuca suggests that in some environments, gravity flows may occur more frequently than predicted from the stratigraphic record. Evidence of gravity-flow deposits have been identified in other coarse-grained delta systems, but represent a small fraction of the total deposit because of the erosive power of ambient waves or currents (e.g., Lønne and Nemec, 2004). The Elwha Delta case thus adds to the ranks of major terrestrial events that have left little marine record.

3.6 Conclusions

During a major dam removal event, a series of gravity-flow processes occurred over a 14-h period within 200 m of a steep deltaic deposit at the mouth of the Elwha River. A few punctuated events displayed characteristics of hyperpycnal plumes or hyperpycnal flows, namely, local near-bed velocity maxima, SSC >10 g/L, anomalous near-bed flow directions, and in one case, an estimated Fr_d of ∼1. These may have been plunging hyperpycnal plumes associated with river effluent of up to ∼14 g/L SSC, assuming that saltwater mixing in the river mouth provided the added density needed to plunge (e.g., Felix et al., 2006). This concept is supported by positive excess boundary-layer densities. Alternatively, a sustained hyperpycnal flow may have been triggered by failure or prolonged erosion of delta-front sediments following several days of intense delivery.

Sustained transport of sandy sediment to the toe of the delta occurred over multiple hours in two stages, 08:00–12:00 and 13:00–18:00, on 9 Mar 2014. In the first stage, evidence suggests continuous failure and downslope transport of dominantly sandy sediment during a period of falling water level, as has been observed in other small-delta systems (e.g., Clare et al., 2016). The second stage was characterized by rapid deposition of well-sorted sands, subcritical flow, and mixing of finer sediments higher into the water column. This change in flow coincided with accelerating along-isobath currents, which may have contributed the turbulence needed to disrupt the flow. The extinction dynamics suggest the formation of

a hydraulic jump and/or lofting plume, which facilitated the transition from a negatively buoyant hyperpycnal flow to a neutrally buoyant homopycnal plume.

The subsequent erosion of nearly all the deposited sediment highlights the potential absence of some "extreme events" from the marine sedimentary record. In environments where sufficient wave and/or current energy is available to erode muddy sands, even major fluvial loading events (up to 14 g/L in this case) and sandy gravity flows may not leave a lasting impression on the stratigraphic record.

Chapter 4

DYNAMIC CONTROLS ON SHALLOW CLINOFORM GEOMETRY: MEKONG DELTA, VIETNAM [1]

4.1 Introduction

Large tropical rivers are major sources of sediment to global oceans (Milliman and Meade, 1983; Nittrouer et al., 1995; Milliman et al., 1999; Syvitski et al., 2003), and often form compound deltas composed of a subaerial deltaic plain and subaqueous deltaic clinoform (e.g., Nittrouer et al., 1986; Kuehl et al., 1989; Alexander et al., 1991; Nittrouer et al., 1996). Here we use the term "clinoform" to denote the total wedge-shaped package of sediments contained in the subaqueous-delta deposits. Subaqueous clinoforms contain large amounts of fluvially derived sediment, sequester diverse geochemical constituents and natural resources, and serve as the marine foundation for subaerial delta progradation (e.g., Coleman and Prior, 1982).

The Mekong River (Figure 4.1) is one of the eleven largest rivers worldwide in terms of both water and sediment discharge (Milliman and Meade, 1983; Perry et al., 1996; Milliman and Farnsworth, 2011). In the past several thousand years, it has transported sediment from the Himalayas, Thailand, Laos, and Cambodia (Rubin et al., 2014) and formed a broad, asymmetric subaerial-delta plain bounded by a long, narrow subaqueous-delta clinoform. Mekong River sediment loads are expected to change, however, as a result of exacerbated human activities like dam construction and channel-bottom mining (e.g., Lu and Siew, 2006; Walling, 2008; Kummu et al., 2010; Kondolf et al., 2014; Brunier et al., 2014). These activities, combined with sea-level rise and land-surface subsidence, have prompted concerns about changes to Mekong Delta shorelines, including coastal erosion and increased flood risks

[1]This chapter was submitted to *Continental Shelf Research* as: Eidam, E.F., Nittrouer, C.A., Ogston, A.S., DeMaster, D.J., Liu, J.P., Nguyen, T.T., Nguyen, T.N., Dynamic controls on shallow clinoform geometry: Mekong Delta, Vietnam, and was accepted for publication on 30 May 2017.

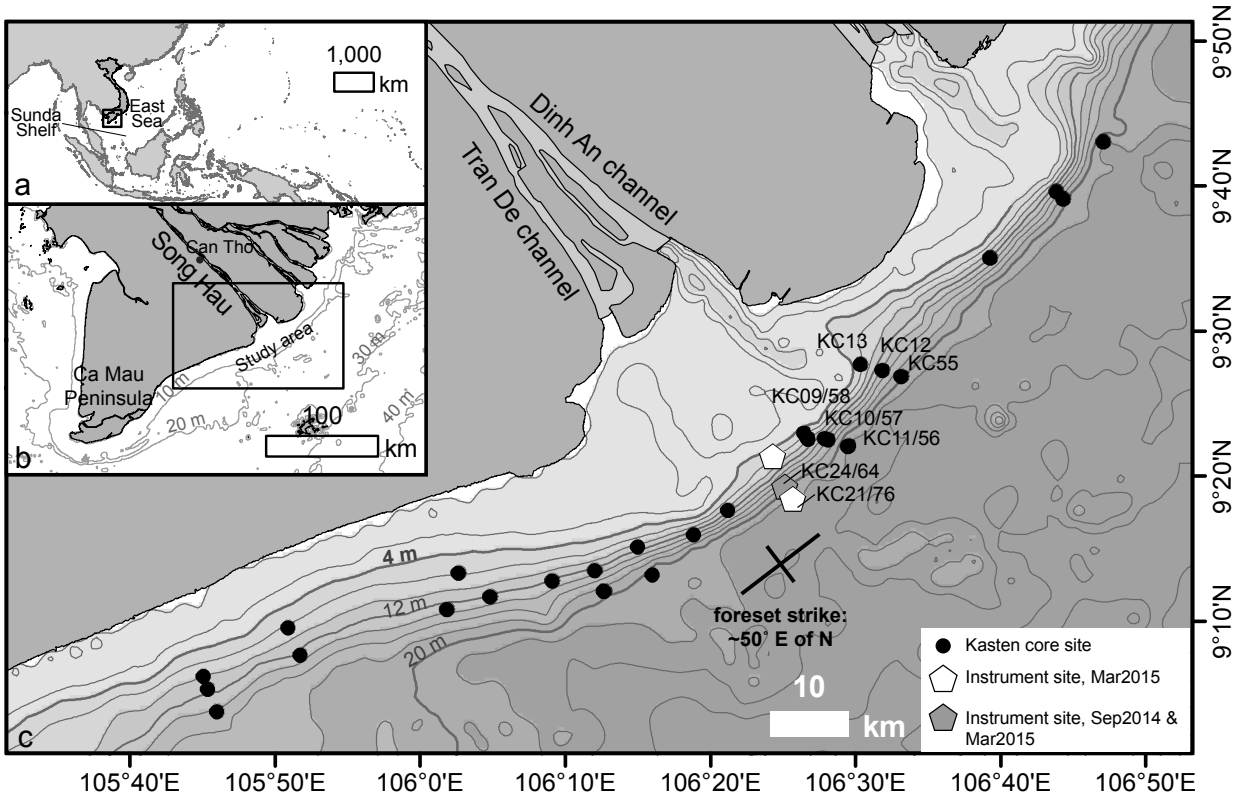

Figure 4.1: Location of study area and sample sites. a) The Mekong River discharges onto the Sunda Shelf in the East Sea. b) The study area was a ∼100-km-long section of the subaqueous delta (or clinoform) offshore of the two branches of the Song Hau, the southernmost Mekong distributary c) Kasten cores and instrument sites were located on the foreset and bottomset. Cores presented in this paper are labeled, and are located near the Song Hau. Cores KC09 through KC24 were collected in Sep14; cores KC55 through KC76 were collected in Mar15. Data from the unlabeled cores are presented in DeMaster et al. (in press). (Contours are 2 m; bathymetry is courtesy of the Vietnam Institute of Marine Geology and Geophysics.)

(Takagi et al., 2014; Manh et al., 2015; Kondolf et al., 2015; Phan et al., 2015; Anthony et al., 2015).

Subaerial and subaqueous deltas are dynamically linked, because a finite amount of sediment is distributed between these two sinks (e.g., Swenson et al., 2005). The fraction of total fluvial sediment sequestered in each sink depends on multiple factors including time since

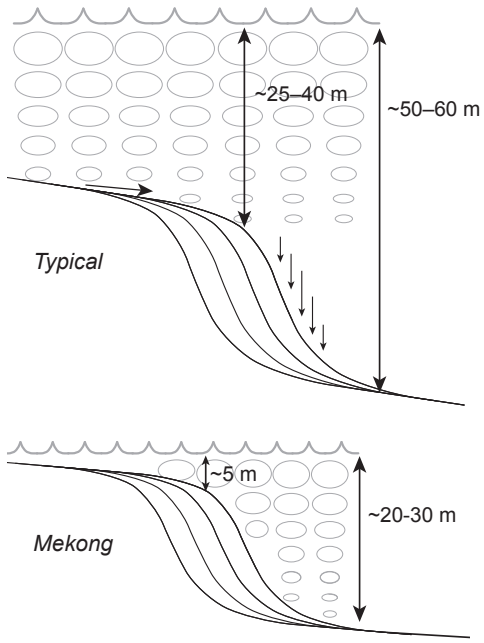

Figure 4.2: Conceptual diagram contrasting typical large-river clinoforms with the Mekong clinoform. Gray ellipses represent potential wave-orbital velocities. Note the different rollover and bottomset depths, and similar clinoform thicknesses.

initiation of the delta, floodplain deposition, sea-level change, change in accommodation space, subaqueous delta progradation rate, and wave and current transport (e.g., Goodbred and Kuehl, 1999; Swenson et al., 2005). This dynamic link has also been recognized for the Mekong Delta (Ta et al., 2002), and the fate of its shoreline is dependent on the mechanics of subaqueous clinoform growth. Previous work has suggested a seasonal connection in sediment transport and storage between the southernmost distributary (Song Hau; Figure 4.1b) and the subaqueous delta (e.g., Gagliano and McIntire, 1968; Wolanski et al., 1998; Tamura et al., 2010; Nowacki et al., 2015). However, the timing and processes of sediment transfer seaward of the river mouth remain poorly understood (Anthony et al., 2015).

The Mekong clinoform is distinguished among large-river deltas in that the transition (or subaqueous "rollover point") between the broad, flat topset and steeper foreset lies at a

depth of only 4–6 m (see Xue et al., 2010; Unverricht et al., 2013; Liu et al., in press). For many large-river deltas, the subaqueous rollover depth is considered the fairweather "wave-current base" (Walsh et al., 2004; Figure 4.2), and is commonly located at 25–40 m depth (e.g., Amazon River, ∼40 m, Nittrouer et al., 1986; Ganges-Brahmaputra River, ∼30 m, Kuehl et al., 1997; Indus River, ∼30 m, Giosan et al., 2006; Ayeyarwady River, ∼30 m, Rodolfo, 1969; and Gulf of Papua, 25–40 m, Walsh et al., 2004). Above this depth, waves and currents provide the energy needed for a majority of sediment to bypass the topset. Below this depth is a "stress refuge," or zone of reduced bed stress, where sediment rapidly accumulates after delivery by advection, diffusion, and/or gravity-flow processes (e.g., Kuehl et al., 1986; Kineke et al., 1996; Pirmez et al., 1998; Traykovski et al., 2007; Walsh and Nittrouer, 2009).

The mechanics that produce shallow rollovers like that of the Mekong (4–6 m), Atchafalaya (∼5 m; Neill and Allison, 2005), and Yangtze (∼12–15 m, Hori et al., 2002; Liu et al., 2007) are poorly constrained, but important to understand because changes in transport energy and/or sediment supply (as expected for the Mekong) can alter the extent or depth of the subaqueous topset, and consequently the subaerial shoreline position (Driscoll and Karner, 1999; Swenson et al., 2005). Many systems with deeper rollovers are classified as tide-dominated deltas (Amazon, Ganges-Brahmaputra, and Gulf of Papua), whereas the Mekong and Yangtze are classified as mixed-energy, or wave- and tide-dominated (e.g., Hori et al., 2002; Goodbred and Saito, 2012). The Yangtze and Mekong clinoforms share similar tidal ranges, wave climates, seasonal storage/transport regimes, and southward growth (e.g., Wright and Nittrouer, 1995; Hori et al., 2002); however, we do not fully understand how these dynamical processes impact the clinoform geometry.

This study evaluates patterns of modern sediment dispersal and deposition seaward of the largest Mekong distributary channel, the Song Hau (Figure 4.1), to understand better the maintenance of a subaqueous rollover at 4–6-m water depth. Specifically, we connect seasonal and across-isobath transport gradients to observed morphology by evaluating:

- seasonal differences in sediment flux magnitudes and directions on the lower foreset;
- across-isobath variations in sediment transport during the energetic windy monsoon; and
- linkages between observed transport patterns, sediment accumulation rates (SARs), and sedimentary structures.

The forcing that contributes to the shallow geometry of the Mekong clinoform is then placed in a more global context, via comparison of wave energy for eight large deltas from around the world. We show that when comparing these systems, bed stresses alone cannot explain observed cross-sectional morphology in terms of a foreset stress refuge, and other factors such as current direction must be considered. Ultimately, this study aids the understanding of large-delta morphodynamics by exploring the impacts of transport direction as well as available transport energy.

4.2 Background

4.2.1 The Mekong River

The Mekong River runs ∼4700 km from the Himalayas to the East Sea (South China Sea) (Figure 4.1). Estimated annual water discharge is ∼475–550 km^3/yr (MRC, 2005 and Milliman and Farnsworth, 2011, respectively) and estimated annual sediment discharge is ∼87 Mt/yr at Kratie, Cambodia (Darby et al., 2016; see Gugliotta et al., in press for location of Kratie). Seasonal water discharge at Kratie varies from ∼2000 m^3/s during the windy northeast monsoon (Nov to Apr) to ∼40,000 m^3/s during the rainy southwest monsoon (May to Oct) (MRC, 2017). In Vietnam, the river splits into seven distributaries (Figure 4.1b); the southernmost (Song Hau) carries ∼40% of the total river discharge (Nguyen et al., 2008), and divides into the Dinh An and Tran De channels near the coast (Figure 4.1c).

4.2.2 Hydrography of the receiving basin

Seaward of the Song Hau, hydrodynamics are affected by regional currents, seasonal monsoons, and basin morphology. Tides are mixed semi-diurnal with a mean range of ∼3.2 m (Gagliano and McIntire, 1968), and M2 current ellipses are counterclockwise (Zu et al., 2008). Ambient salinity in the topset region is typically ∼32 ppt (Gagliano and McIntire, 1968). Regional currents are anticyclonic during the rainy southwest monsoon (May to Oct) and cyclonic during the windy northeast monsoon (Nov to Apr) (Hu et al., 2000; Liu et al., 2001). Near the Mekong distributaries, rainy-season surface flow is northeastward (Jun–Aug, ∼0.50 to 0.75 m/s) and windy-season surface flow is southwestward (Oct–Apr, ∼0.10 to 0.75 m/s) (Wyrtki, 1961; Gagliano and McIntire, 1968; Fang et al., 2002). During the rainy monsoon, upwelling likely helps carry the high-discharge plume offshore (Hordoir et al., 2006; see also Dippner et al., 2006), while during the windy monsoon/downwelling season, the low-discharge plume is compressed against the coast (Hordoir et al., 2006). Southern Vietnam was impacted by 47 typhoons between 1954 and 1991; 20 occurred during November (Imamura and To, 1997), a season of waning river discharge following the rainy monsoon.

4.2.3 Previous work on sediment dynamics seaward of the Song Hau

Net sediment export from the Dinh An channel is ∼11 Mt/yr, which reflects ∼1 t/s export during the high-flow season and ∼0.3 t/s import during the low-flow season (Nowacki et al., 2015). Particle sizes in the Song Hau are >50% fine silt and 15–20% clay (Wolanski et al., 1996). At Can Tho, typical suspended-sediment concentrations (SSCs) range from 0.01 g/L (Mar 2015) to 0.06 g/L (Sep 2014); greater variations occur in estuarine waters at the mouth of the Dinh An (0.05–0.15 g/L in Sep 2014, and 0.15–0.25 g/L in Mar 2015; McLachlan et al., in press).

Seaward of the Song Hau, SSCs vary by an order of magnitude between the rainy southwest monsoon and windy northeast monsoon (Anikiyev et al., 1986). Monthly surface SSCs characterized from satellite observations are greatest from Jul to Mar (sometimes exceeding

0.1 g/L), reflecting river input during the rainy summer monsoon and subsequent coastal resuspension during the windy winter monsoon (Loisel et al., 2014). The maximum spatial extent of this coastal turbid zone occurs in Apr–May (Loisel et al., 2014). Late in the windy monsoon season (Mar–May), the greatest coastal SSC has been measured between the shoreline and the seaward limit of the subaqueous delta, with greater values occurring near-bed than at the surface (Unverricht et al., 2014).

In general, fluvial sediment is delivered to the inner shelf (i.e., the topset) during the rainy summer monsoon, and then resuspended and transported southwestward during the windy winter monsoon (e.g., Gagliano and McIntire, 1968; Nguyen et al., 2000; Liu et al., 2009; Xue et al., 2012; Unverricht et al., 2013; Xue et al., 2014), when sediment is also re-imported into the river (Wolanski et al., 1996; Wolanski et al., 1998; Nowacki et al., 2015). Modeled bottom currents are similar during both rainy and windy monsoons, and wave resuspension during the windy monsoon probably facilitates southwestward sediment transport (Xue et al., 2012).

4.2.4 The compound Mekong Delta

The Mekong Delta is a compound delta composed of a ∼63,000 km^2 subaerial plain (Nguyen et al., 2000) and >300-km-long subaqueous delta on the Sunda Shelf, which was submerged after the Last Glacial Maximum (e.g., Hanebuth and Stattegger, 2003; Schimanski and Stattegger, 2005). The delta shoreline has prograded 200 km since the Holocene sea-level lowstand 6.3 kya (Tamura et al., 2009), at decreasing rates (17–18 m/yr prior to 3.5 kya, and 13–14 m/yr after 3.5 kya; Ta et al., 2001). The delta is thought to have transitioned from tide-dominated to wave- and tide-dominated ∼3 kya (Ta et al., 2002; see also Hanebuth et al., 2012).

The toe of the modern subaqueous delta lies at ∼24–32-m water depth (Gagliano and McIntire, 1968; Xue et al., 2010; Unverricht et al., 2013; Liu et al., in press), and the shelf break between the Sunda Shelf and the central basin of the East Sea lies at 180–220-m water depth (Hanebuth and Stattegger, 2003) ∼300 km east of the Song Hau mouth. Intense

southwestward coastal transport associated with northeast monsoon winds has formed the Ca Mau Peninsula southwest of the Mekong distributaries (Figure 4.1; e.g., Gagliano and McIntire, 1968; Liu et al., 2009; Xue et al., 2010; Tamura et al., 2012).

The modern subaqueous delta exhibits properties of a typical mud-rich subaqueous delta composed of clinoform-shaped structures, and will henceforth be referred to as a clinoform for brevity. Internal beds converge at the landward and seaward ends (Xue et al., 2010; Liu et al., in press), forming a sigmoidal sediment wedge consistent with clinoform models. The topset width varies from >12 km seaward of the Song Hau (Unverricht et al., 2013) to <3.5 km in the south-central region (Unverricht et al., 2013), where the shoreline is likely erosional (e.g., Anthony et al., 2015). Foreset slopes range from 0.001 to 0.005 (Xue et al., 2010), which are low compared to other muddy clinoforms (Patruno et al., 2015).

Surface sediments within 25 km of the Song Hau (along-isobath) are dominated by fine to very fine sands and silty sands; farther southwestward, clinoform sediments grade into sandy silt with patches of sand (Unverricht et al., 2013; see also Xue et al., 2014). Seaward of the bottomset, sediments are thought to be coarser, relict sands remaining from the Holocene sea-level transgression (Unverricht et al., 2013). Estimated sediment accumulation rates (SARs) near the southern end of Ca Mau are >1–10 cm/yr, in cores composed of laminated sandy muds found in <12-m water depth (Unverricht et al., 2013). Cores collected from diverse locations on the clinoform exhibit non-steady-state and/or very rapid accumulation (Unverricht et al., 2013; Xue et al., 2014).

4.3 Methods

4.3.1 Instrument measurements

Water-column profile data and time-series measurements were collected using ship-based sensors and a boundary-layer instrument system (tripod), respectively, in Sep 2014 and Mar 2015. These sampling times will henceforth be referred to as "Sep14," coinciding with peak river flow, weak southwest winds, and wet monsoon conditions; and "Mar15," coincid-

ing with weak river flow and strong northeast monsoon winds. Ship-based water-column salinity, temperature, depth, and SSC profiles were measured with a small profiling conductivity/temperature/depth (CTD) sensor outfitted with an optical backscatter sensor (OBS). Measurements were made at ∼10–20 sites across the subaqueous delta during each survey, and every 30 min for 10–12 h at tripod stations (Figure 4.3). Acoustic backscatter measurements were collected along several transects and at tripod stations using a downward-looking acoustic Doppler current profiler (ADCP, 600 kHz) mounted on the vessel at 2.7 m below the water surface.

The tripod was deployed on the lower foreset seaward of the Song Hau in Sep14, and at the same station as well as upper-foreset and bottomset stations in Mar15 (Figure 4.1c). The system included an upward-looking 1200-kHz ADCP, a downward-looking 2 MHz high-resolution ADCP (hrADCP), an acoustic Doppler velocimeter (ADV), a pressure/wave/turbidity sensor, and 1–3 OBSs. Deployments lasted ∼10–12 h and were limited by daylight hours and local fishing activity.

OBS data from fixed and profiling sensors, as well as ADCP backscatter data from the shipboard sensor, were converted to SSCs via lab and field calibrations (Appendix A.1, A.2). Boundary-layer sediment fluxes were computed from OBS and current data (Appendix A.3). Total, wave, and current shear velocities (u_*, u_{*c}, and u_{*w}) for time-series observations were calculated from ADV data using a wave-current interaction model (Madsen, 1994) with an assumed bed roughness of $z_0 = 0.7$ mm (sand/mud bed; Soulsby, 1997), and from hrADCP data using the log-profile method (e.g., Sternberg, 1972). Values obtained from the log-profile method were discarded where $R^2 < 0.98$ for the log-linear fit of the velocity profile.

4.3.2 Sediment cores

Thirty-two kasten-type gravity cores measuring 12 cm square by up to 3 m long were collected at water depths of ∼5–21 m along a 140-km stretch of the subaqueous delta (Figure 4.1) during both cruises. X-radiograph negatives were produced from 23 cores. Cores were subsampled at 2-cm intervals for grain-size and radiochemical analyses. Subsamples were

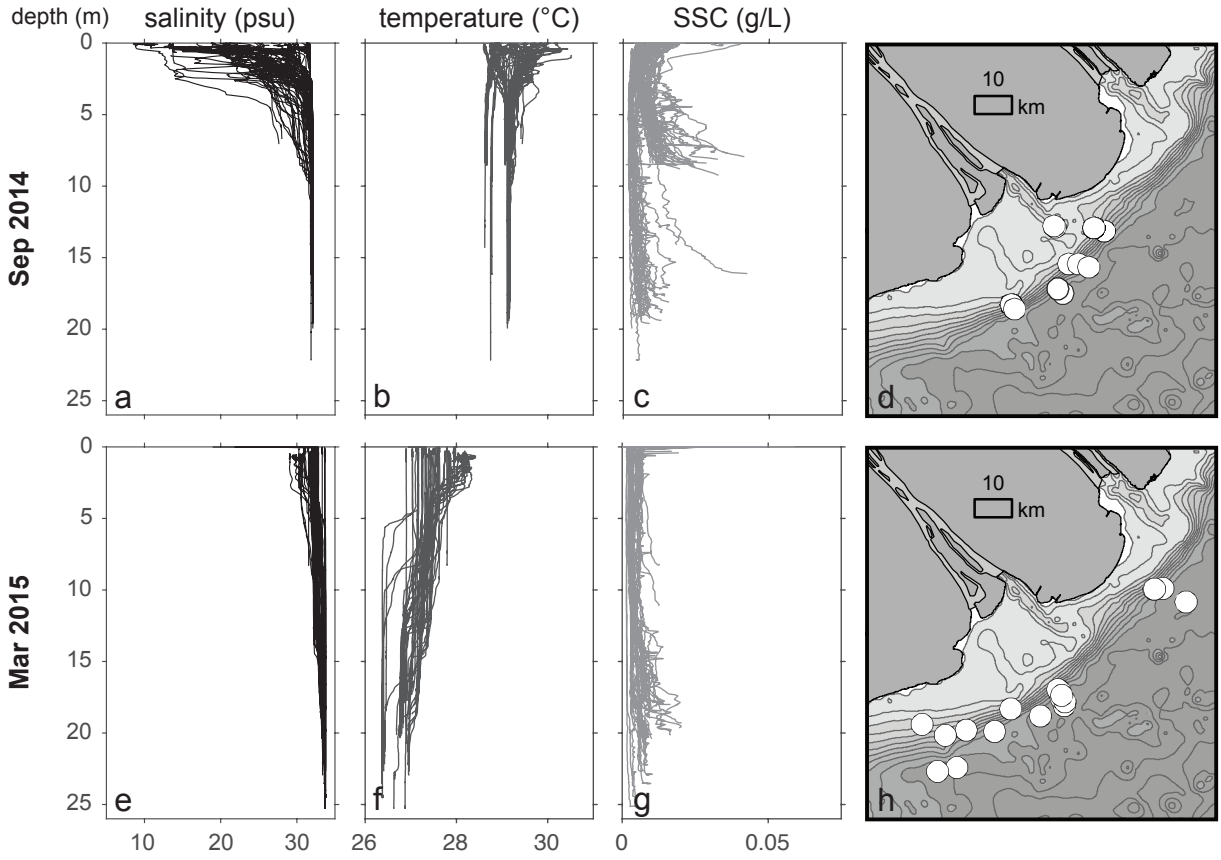

Figure 4.3: Salinity, temperature, and SSC profiles. Water-column profiles from all casts collected during the study in Sep14 (top row) and Mar15 (bottom row) illustrate seasonal variability. Surface and ambient salinities were generally fresher in Sep14, temperatures were generally cooler in Mar15. SSCs at >8 m depth were similar in both seasons, but were greater in Sep14 than in Mar15 at stations <8 m deep, especially near bed.

analyzed for mud/sand size distributions in the lab (Appendix A.4). Data were binned into percents of sand ($\leq$4 ϕ; $\geq$63 μm), coarse/medium silt (5–6 ϕ; 16–63 μm), fine/very fine silt (7–8 ϕ; 4–16 μm), and clay (>8 ϕ; <4 μm). Radiochemical analyses of ^{210}Pb were performed on a subset of core samples to determine SARs and mass accumulation rates (MARs), following a method similar to that of Nittrouer et al., 1979 (Appendix A.5). Results from a subset of 13 cores collected near the Song Hau and at tripod sites are presented herein; results from all cores and a detailed discussion of radiochemical analyses are presented in

DeMaster et al. (in press).

4.3.3 Wave climates and modeled bed stresses

Monthly wave climatologies for the Mekong and seven other fluvial dispersal systems were obtained from the NOAA WAVEWATCH III (NWW3) model (NOAA, 2016b) for a 10-yr period. This information was used to estimate mean annual wave-induced shear velocities at a range of water depths for each system using linear wave theory. For the Mekong, total (wave and current) shear velocities were also estimated using NWW3 model output together with annual mean currents extrapolated from the data collected in this study (Appendix A.6).

The eight fluvial dispersal systems selected for comparison were chosen because they have subaqueous clinoforms that are actively supplied by fluvial sediment sources, are evolving under modern fluvial-marine dispersal processes, and lie within the NWW3 model domain. This list is not meant to be exhaustive, but rather to highlight differences in morphologies and forcing mechanisms. A few other fluvial-marine dispersal systems exhibit shallow clinoforms, including the Mahakam River, Orinoco River, and Adriatic Sea. However, such systems were omitted from comparison because of complicating factors like subsidence, sparse published data, and role of Ekman transport (e.g., Salahuddin and Lambiase, 2013; Aslan et al., 2003; Puig et al., 2007;).

4.4 Results

4.4.1 Water-column profiles

In Sep14, ambient ocean salinity was ∼31.9–32.1 psu, and a fresher surface plume of ∼9–30 psu was observed to depths of ∼0.5–5 m (Figure 4.3a). Temperatures ranged from 28.6 to 30.5°C, and were generally warmer in the plume (Figure 4.3b). SSC was typically <0.03 g/L throughout the water column. Peaks in SSC occurred in surface waters and near bed. Greatest near-bed SSC occurred at stations in shallow water depths (i.e., <8 m; Figure 4.3c).

In Mar15, ambient ocean salinity was ∼32.2–33.0 psu (Figure 4.3d), and a slightly fresher surface layer of ∼29–32 psu extended to depths of ∼3–5 m (Figure 4.3e). Temperatures ranged from 26.4 to 28.5°C, and were frequently up to 2°C warmer at the surface than at depth (Figure 4.3f). SSC was <0.02 g/L throughout the water column (Figure 4.3g).

4.4.2 Time-series measurements

Seasonal comparison from instrument deployments

Seasonal variations in water-column and boundary-layer dynamics were observed at the lower foreset site (Figure 4.4; see Figure 4.1 for location). In Sep14, peak surface currents (>0.60 m/s at 0–10-m depth) and peak boundary-layer currents (∼0.35 m/s, ∼0.47 mab) were measured during the falling tide within the 12 h 20 min deployment window (which was nearly as long as a 12 h 25 min tidal cycle). Maximum u_* was ∼0.026 m/s during the falling tide and ∼0.023 m/s during the rising tide. It is worth noting that u_* values computed using the log-profile method (applied to hrADCP data) and wave-current interaction model (applied to ADV data) were similar. Total u_* was slightly greater than u_{*_c} at all times (Figure 4.4). Surface salinities were smallest during falling tide, though this freshened surface layer persisted during the rising tide. Maximum SSC in this surface layer was ∼0.012 g/L. Significant wave heights and wave-orbital velocities were <0.05 m and <0.01 m/s, respectively. Maximum observed SSC was ∼0.015-0.025 g/L within 2.5 m of the bed during low tide, coinciding with northeastward currents and minimum bed stresses (Figure 4.4, left column). The net measured transport direction was ∼15° east of north and along-isobath.

At the same site in Mar15, peak surface currents (>0.60 m/s at 0–10-m depth) and peak boundary-layer currents (0.34 m/s, ∼0.47 mab) occurred during the rising tide (Figure 4.4, right column), in contrast to Sep14 peak currents. It should be noted that Mar15 deployments only lasted 10 h 10 min to 11 h each, i.e., they lasted 82%–89% of a 12 h 25 min tidal cycle, and so maximum and minimum measured values may not represent the extreme values for a given tidal cycle. Bed shear velocities were of similar magnitude to Sep14 values,

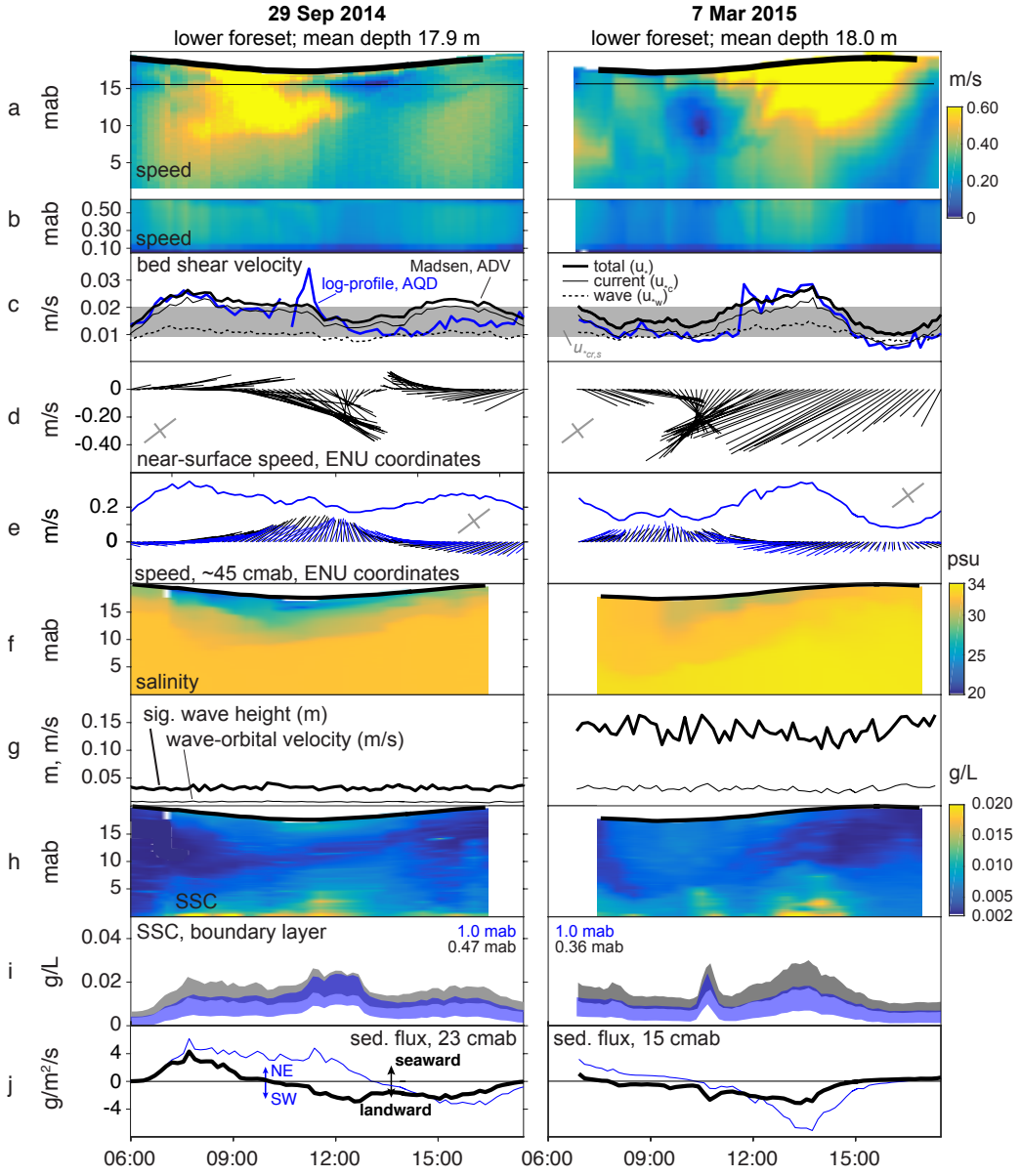

Figure 4.4: Seasonal comparison of time-series boundary-layer measurements on the lower foreset. a) Up-looking ADCP current velocities; b) down-looking boundary-layer hrADCP current velocities; c) bed shear velocities computed by the log-profile method (hrADCP) and wave-current interaction model (ADV), with nominal threshold of motion for sand shown in gray; d) stick plots of surface currents (see line in (a) for corresponding depth); e) magnitude (continuous line) and vectors of currents at ~0.45 mab; f) water-column salinity contoured from CTD casts; g) significant wave height and wave-orbital velocity; h) SSC contoured from 30-min CTD casts; i) SSC near bed; j) sediment flux for across-shelf (bold) and along-shelf (blue) directions. Deployment sites are shown in Figure 4.1. Gray crosses represent along- and across-isobath directions (see Figure 4.1c). Times are local.

but peaked during a different tidal condition. The maximum values (u_* = 0.028 m/s, u_{*c} = 0.024 m/s, u_{*w} = 0.015 m/s) occurred during the rising tide and southwestward current flow. Minimum observed u_* (0.016–0.020 m/s) and minimum observed u_{*w} and u_{*c} (both ∼0.007–0.011 m/s) occurred during periods of along-isobath flow. The wave climate was slightly more energetic in Mar15 than in Sep14, with H_{sig} and u_{br} of ∼0.15 m and 0.04 m/s, respectively. Sediment flux was greatest during periods of rising tides and was generally landward and southwestward. The net transport direction for the 10 h 40 min lower foreset deployment was 65° west of north, i.e., landward across-isobath.

Cross-shelf comparison of hydrodynamics and sediment fluxes from instrument deployments

In Mar15, strong across-shelf variabilities were observed in near-bed currents and sediment fluxes (Figure 4.5; see Figure 4.1 for locations). Peak near-bed currents were 0.38, 0.34, and 0.28 m/s at the upper foreset, lower foreset, and bottomset sites, respectively, and directions of peak measured flow were variable. Corresponding maximum bed shear velocities were 0.059 m/s, 0.028 m/s, and 0.024 m/s, representing a ∼60% reduction down-slope. Surface currents were similar in magnitude and direction at all three sites, were strongly southwestward, and were maximum during rising tides. These surface currents were associated with deflection of near-bed currents on the upper foreset, but appeared to have little influence on near-bed currents at the two deeper sites (Figure 4.5).

Wave heights and orbital velocities were greatest on 11 Mar at the upper foreset site, and were ∼1 m and 0.5 m/s, respectively. Maximum observed near-bed SSC occurred during rising tides, and was 0.78 g/L on the upper foreset, 0.018 g/L on the lower foreset, and 0.011 g/L on the bottomset, a ∼99% decrease down-slope. Sediment fluxes were dominantly landward and southwestward on the upper foreset, and were two orders of magnitude greater than those at the two deeper sites (Figure 4.5).

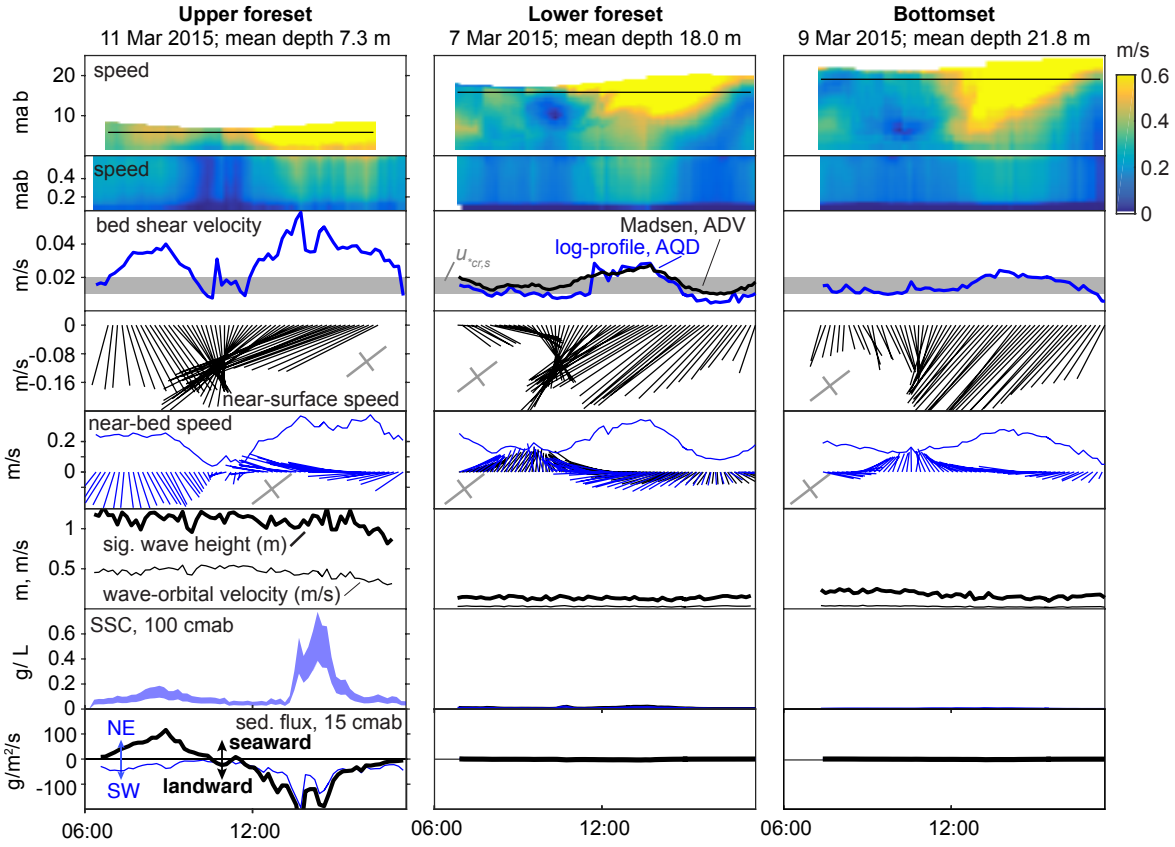

Figure 4.5: Cross-shelf comparison of time-series boundary-layer measurements collected on the upper foreset, lower foreset, and bottomset in Mar15. See Figure 4.4 caption for detailed descriptions. Deployment sites are shown in Figure 4.1. Times are local.

Cross-shelf ADCP transects

Sediment concentrations observed in across-isobath ADCP transects were greatest near-bed during falling tides (Figure 4.6, transects T2 and T6), and were twice those observed during rising tides. During both rising and falling tides, SSCs >0.01 g/L were localized to regions <12 m deep. At the southernmost transect (T5, Figure 4.6), suspended sediment was more evenly mixed throughout the water column than at sites near the river mouth. No along-shelf trend in SSC was apparent between transects northeast and southwest of the Song Hau.

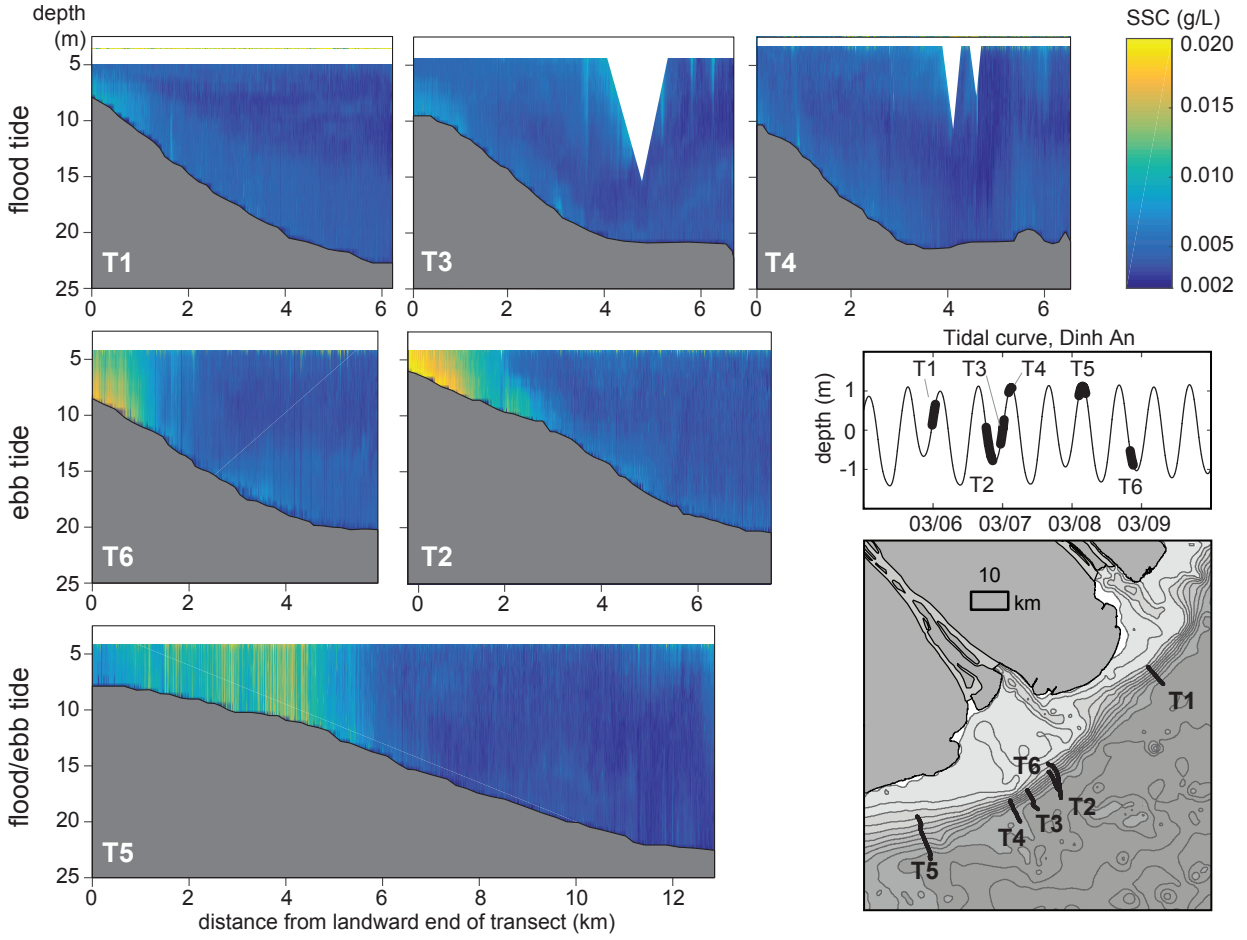

Figure 4.6: Cross-isobath ship-mounted ADCP transects of calibrated backscatter from Mar15. Transects (T1, et cetera as shown) were completed at the tidal phases shown on the Dinh An predicted tidal curve and at locations shown on the map (lower right). Greatest SSC was observed at <12 m water depth on transects T2, T5, and T6. Approximate tripod deployment locations are shown on T2. (Surface values representing instrument noise have been shaded.)

4.4.3 Seabed sediment sizes and structures

Sand, silt, and clay fractions varied in cores collected along three transects near the Song Hau (Figure 4.7). Upper foreset cores (KC13 and KC09/58) contained ≤45% sand. Lower foreset cores (KC12, KC10/57, and KC24/64) contained ≤25% sand, with remaining size fractions divided somewhat evenly between silt and clay. Physical laminations millimeters to centimeters thick were most prevalent in upper foreset cores (Figure 4.8). Evidence of physical and biological mixing was widespread in cores on the lower foreset (Figure 4.8). Bottomset cores (KC55, KC11/56 and KC21/76) were characterized by sand fractions of 10–70%, and were composed of abundant shell hash. Sand fractions of select subsamples were analyzed, and yielded fine to very fine sand. Grain-size distributions and median grain sizes (d_{50}) in homogenized 2-cm-thick subsamples showed little down-core variability within cores (Figure 4.7; Figure B.3). Along transects, bottomset cores contained greater sand fractions than foreset cores (Figure 4.7).

4.4.4 Sediment accumulation rates

Sediment accumulation rates (SARs and MARs) are presented for 13 cores collected at the tripod sites and on transects near the Song Hau (Figure 4.9 and Table A.1); replicate datasets and data for additional cores are presented in DeMaster et al. (in press). SARs (MARs) varied across-isobath, and were greatest at ∼13–14-m water depth (Figure 4.9a, c). Rates were moderate on the upper foreset, ranging from 4.1(3.7) to 5.3(5.4) cm/yr (g/cm^2/yr). Rates were moderate to high on the lower foreset, ranging from 3.3(3.4) to 7.9(7.9) cm/yr (g/cm^2/yr). (Even greater rates were observed at similar depths elsewhere in the study area; see DeMaster et al., in press.) Rates were smallest on the bottomset, ranging from 0.47(0.59) to 1.7(1.4) cm/yr (g/cm^2/yr). Cores collected at the same stations in both Sep14 and Mar15 sometimes yielded different SARs, highlighting the small-scale spatial variability within the system. Several cores exhibited evidence of non-steady state accumulation (Figure 4.10) in many forms, including isolated layers of anomalously high activity (e.g., KC55, Figure 4.10)

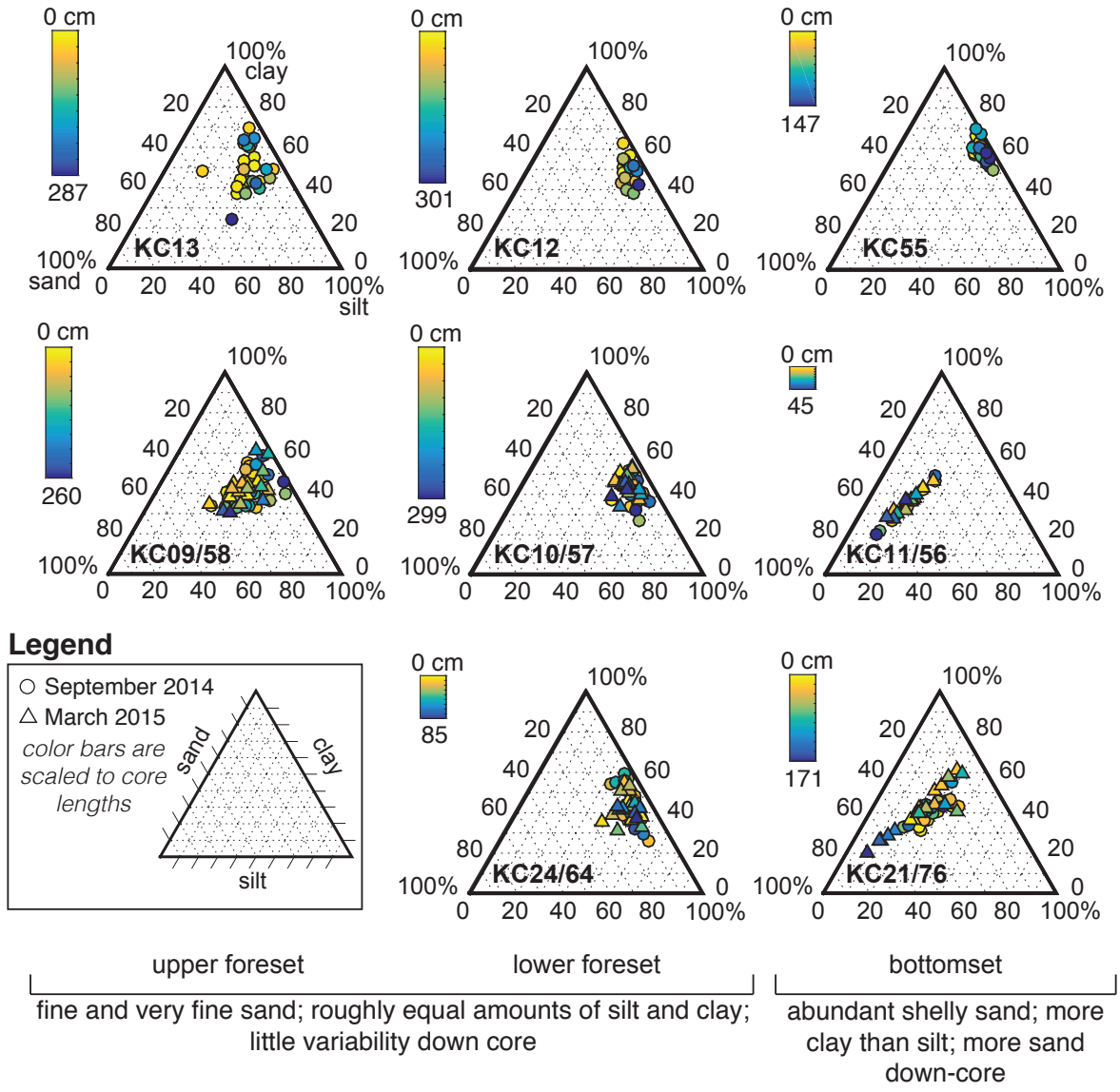

Figure 4.7: Down-core grain-size distributions from kasten cores collected along three cross-shelf transects near the river mouth. Upper foreset sites contained up to 45% sand, lower foreset cores contained up to 30% sand, and bottomset cores contained up to 70% sand. In foreset cores, silt and clay fractions were roughly equal to each other, and there was little variability with depth in core. In bottomset cores KC11/56 and KC21/76, sand fractions increased with depth in core. Note that KC55 is likely transitional between foreset and bottomset. See Figure 4.1, 4.9 for core locations.

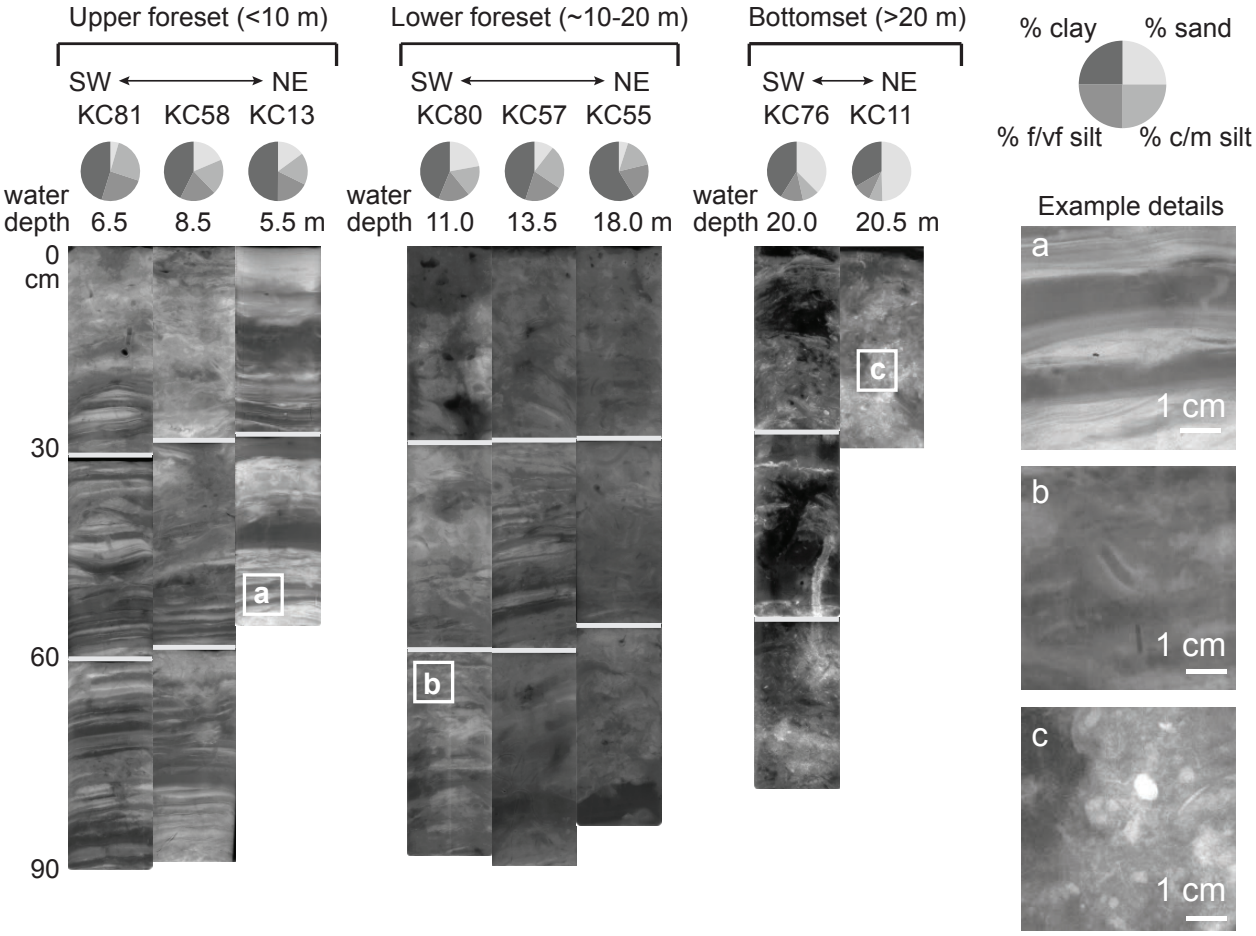

Figure 4.8: Core structures and sediment sizes. Mean grain-size distributions (from subsample intervals shown in Figure 4.9) and x-radiograph negatives from the upper 30-90 cm are shown for cores from the upper foreset, lower foreset, and bottomset. Physical structures were most prevalent on the upper foreset, at water depths <10 m (left; inset a). Mottled sediments and evidence of bioturbation (e.g., burrows) were prevalent on the lower foreset, at 10–20 m water depth (middle; inset b). Shell hash was observed in bottomset cores from >20 m water depth (right; inset c).

and apparent changes in sediment input over short time scales (e.g., KC58 and KC13 in Figure 4.10); however, no consistent patterns were observed among the 21 cores processed for this study (see also DeMaster et al., in press). Some cores (e.g., KC58, Figure 4.10) exhibited a transition from laminated sediments at depth to mottled/bioturbated sediments near the surface. Additional core data are presented in Table A.1 and Figure A.4.

4.4.5 Wave climates and modeled wave stresses for the Mekong and other systems

Based on the NWW3 model (NOAA, 2016b), the Mekong wave climate peaks in Nov through Feb, with $\overline{H_{sig}}$ >1.0 m, $\overline{T}$ of 8–10 s, and $\overline{u_{br}}$ of 0.2–0.3 m/s (Figure 4.11) at 20-m water depth seaward of the Song Hau. This timing coincides with the northeast windy winter monsoon, and lags peak river discharge (Aug to Nov) (Figure 4.11). In a global context, the wave climate (in terms of frequency distribution of $\overline{H_{sig}}$ and $\overline{T}$ at 20 m water depth) of the Mekong dispersal system is comparable to that of the Atchafalaya system, and weaker than those of the Yangtze, Amazon, Ayeyarwady, Ganges-Brahmaputra, Gulf of Papua, and Indus systems (Figure 4.12).

At the depth of the rollover, modeled $\overline{u_*}$ and $\overline{u_{*_w}}$ for the Mekong clinoform are ∼2 times greater during the windy monsoon than the rainy monsoon (Figure 4.13). Both $\overline{u_*}$ and $\overline{u_{*_w}}$ exceed the nominal threshold of motion for sand (∼0.01–0.02 m/s; Miller et al., 1977) to depths of ∼14–23 m during the windy monsoon, but only to depths of ∼5–19 m during the rainy monsoon. The rollover depth of 4–6 m coincides with modeled $\overline{u_*}$ of 0.045–0.058 m/s during the windy monsoon (Nov–Apr) and 0.023–0.029 m/s during the rainy monsoon (May–Oct).

Modeled mean annual $\overline{u_{*_w}}$ at rollover depths for the Mekong and Atchafalaya systems are greater than the threshold of motion for sand ($\overline{u_{*cr,s}}$) (Figure 4.14a). For the Yangtze system, the difference between $\overline{u_{*_w}}$ and $\overline{u_{*cr,s}}$ is smaller (Figure 4.14b), and for systems with deeper rollovers, $\overline{u_{*_w}}$ converges with $u_{*cr,s}$ at rollover depths (Figure 4.14c).

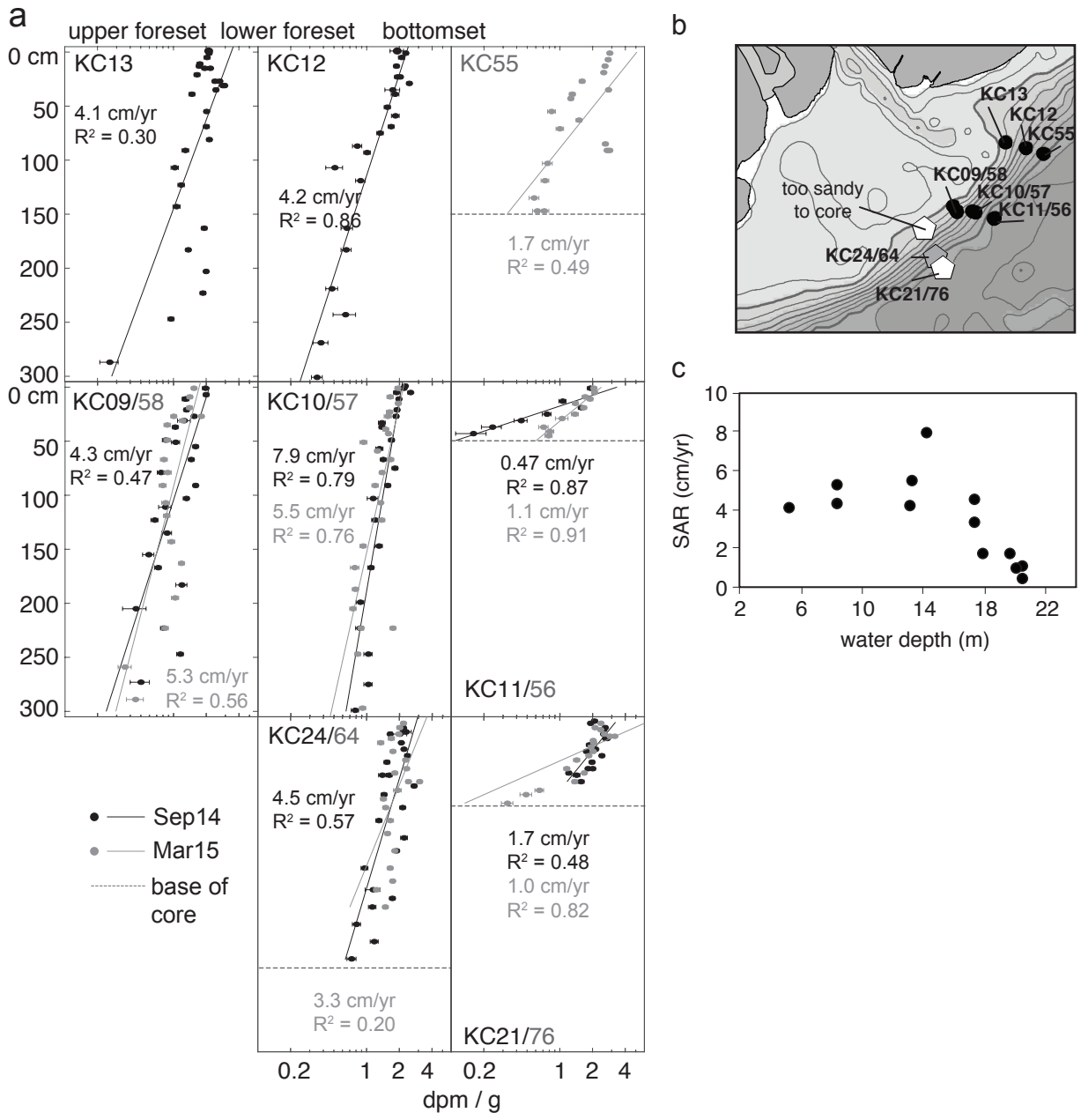

Figure 4.9: Apparent sediment accumulation rates (SARs). (a) Accumulation rate profiles for 8 sites and 2 seasons. (b) Map of cores presented here (see DeMaster et al., in press for additional results). (c) SAR versus water depth for the cores shown in (a) and (b).

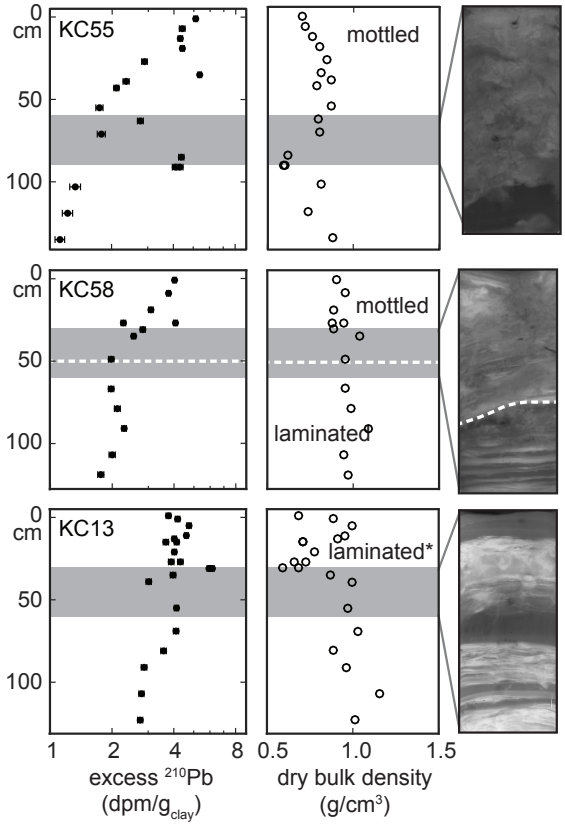

Figure 4.10: Examples of non-steady-state accumulation features observed from various water depths throughout the study area. Shaded areas in ^{210}Pb and density plots correspond to x-radiograph negatives shown at right. KC55 exhibits mottled sediments and several regions of anomalously high clay-normalized excess ^{210}Pb activity. KC58 exhibits a transition from mottled to laminated sediments at ∼50 cm depth, which corresponds to an increase in accumulation rate down core. KC13 exhibits laminated sediments, variable activities, and variable densities. *Laminated sediments were observed from 0-60 cm in KC13; x-radiograph negatives below 60 cm were not collected.

4.5 Discussion

Advective sediment transport on the subaqueous Mekong Delta is thought to be dominated by the northeast windy monsoon, resulting in along-shelf clinoform growth toward the southwest, much like the Yangtze River and Adriatic Sea clinoforms (e.g., Liu et al., 2006; Cattaneo et al., 2007). The controls on the shallow across-shelf geometry of the Mekong clinoform are

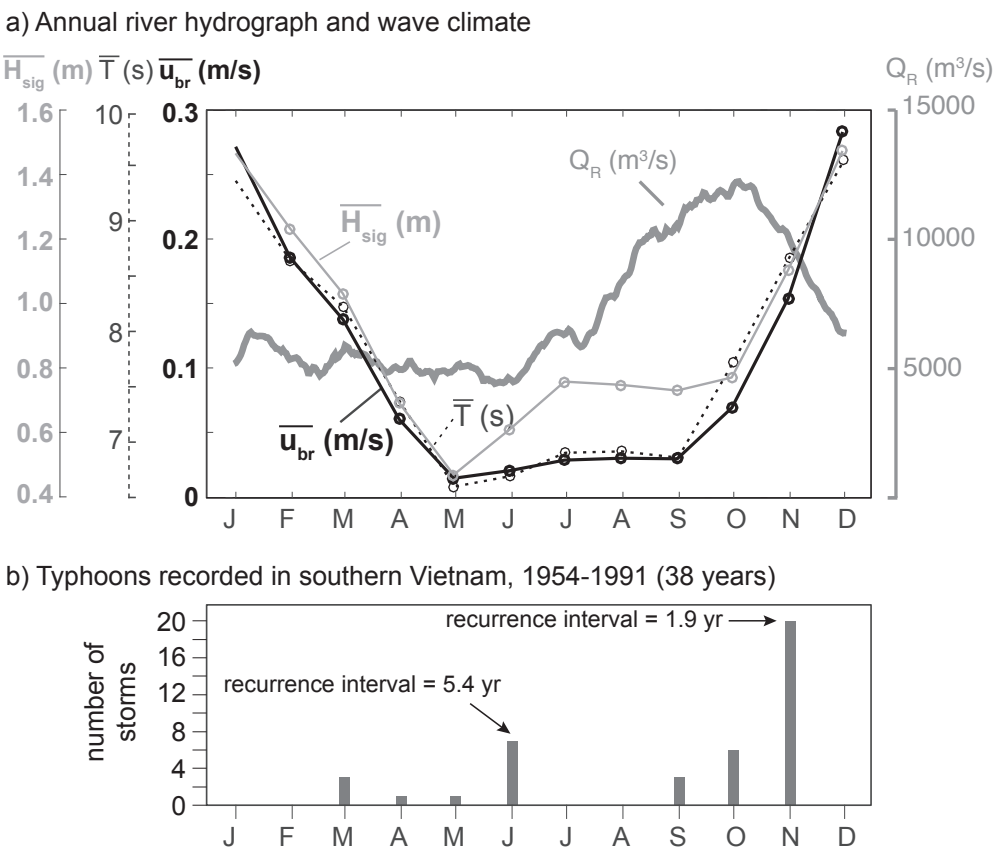

Figure 4.11: Mekong River hydrograph, Mekong Delta wave climate, and southern Vietnam typhoon frequency. a) Annual time-series of Mekong River discharge at Can Tho, and Mekong wave parameters at 20-m water depth seaward of the river mouth. $\overline{H_{sig}}$ = significant wave height, $\overline{T}$ = wave period, and $\overline{u_{br}}$ = wave-orbital velocity (all values are monthly means). River discharge peaks in Sep-Oct, and wave energy peaks in Nov-Mar. River data were obtained from the Mekong River Commission (MRC, 2017). Wave parameters were obtained from the NWW3 global wave model (NOAA, 2016b). b) Typhoons recorded in southern Vietnam from 1954 to 1991 (38-yr period), as reported by Imamura and To, 1997. During this period, typhoons occurred most frequently in November, with a recurrence interval of 1.9 yr.

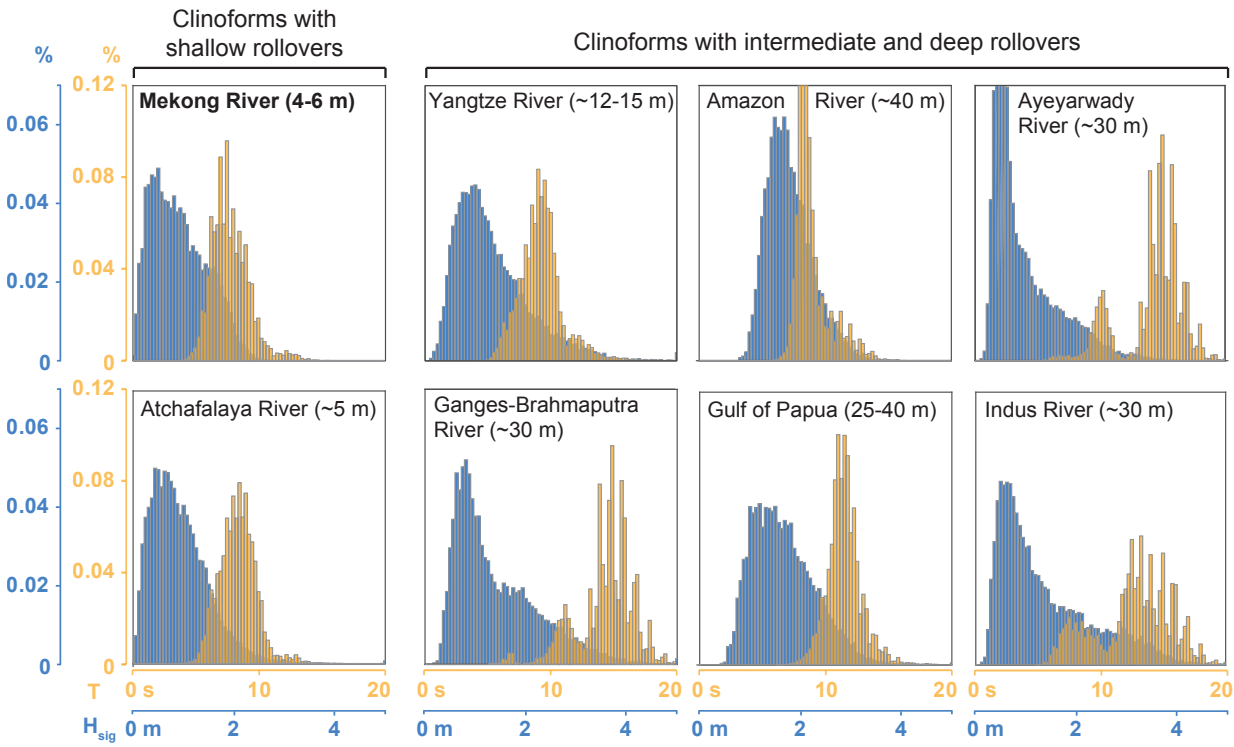

Figure 4.12: Histograms of modeled wave periods (T) and significant wave heights (H_{sig}) for eight large-river deltas at 20-m water depth. Wave periods and heights tend to be smaller in deltaic systems with shallower rollovers. Wave parameters were obtained from WaveWatchIII (NOAA, 2016b). See text for rollover depth citations.

less well understood, however. Possible controls are discussed here in terms of sediment delivery and seasonal reworking processes, with supporting evidence from seabed cores. Transects sampled near the Song Hau are highlighted, where signals of sediment transfer are expected to be most pronounced because of proximity to a major sediment source. Modeled gradients in bed shear velocities are then used to evaluate the concept of a stress refuge for the Mekong clinoform. Finally, wave stress versus depth relationships for the Mekong system are compared to those of seven other large-delta systems, in order to understand better the differences in morphodynamics.

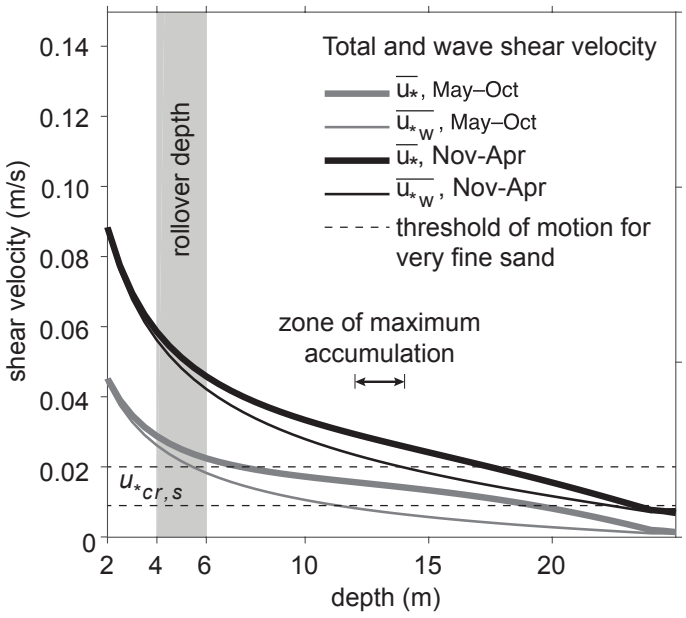

Figure 4.13: Modeled total and wave shear velocities ($\overline{u_*}$,$\overline{u_{*w}}$) for two seasons. The rollover depth coincides with modeled $\overline{u_*}$ = 0.045–0.059 m/s during the windy monsoon (Nov–Apr) and 0.023–0.029 m/s during the rainy monsoon (May–Oct). During the windy monsoon, modeled $\overline{u_*}$ and $\overline{u_{*w}}$ exceed the nominal threshold of motion for very fine sand (0.01-0.02 m/s; dashed lines) at all topset and foreset depths. During the rainy monsoon, $\overline{u_{*w}}$ is less than the threshold of motion for sand at most depths on the foreset.

4.5.1 Seasonal sediment concentrations and connections between environments

Mean plume concentrations (∼0.010 g/L at 20–30 km from shore) were similar to those measured by Anikiyev et al. (1986) and modeled by Xue et al. (2012), but less than those predicted from monthly satellite SSC climatologies by Loisel et al. (2014). These measurements represent a snapshot of coastal conditions in a spatially variable plume (see Wackerman et al., in press), but the magnitudes and patterns of SSC provide valuable insight about sediment delivery pathways. During the high-discharge season, plume SSC values were less than those measured in the river (at Can Tho) and in the Dinh An estuary (see McLachlan et al., in press). Given surface-water velocities of ∼0.20–0.80 m/s (Figure 4.4) and a nominal floc settling velocity of 1 mm/s (e.g., Sternberg et al., 1999; Dinh An

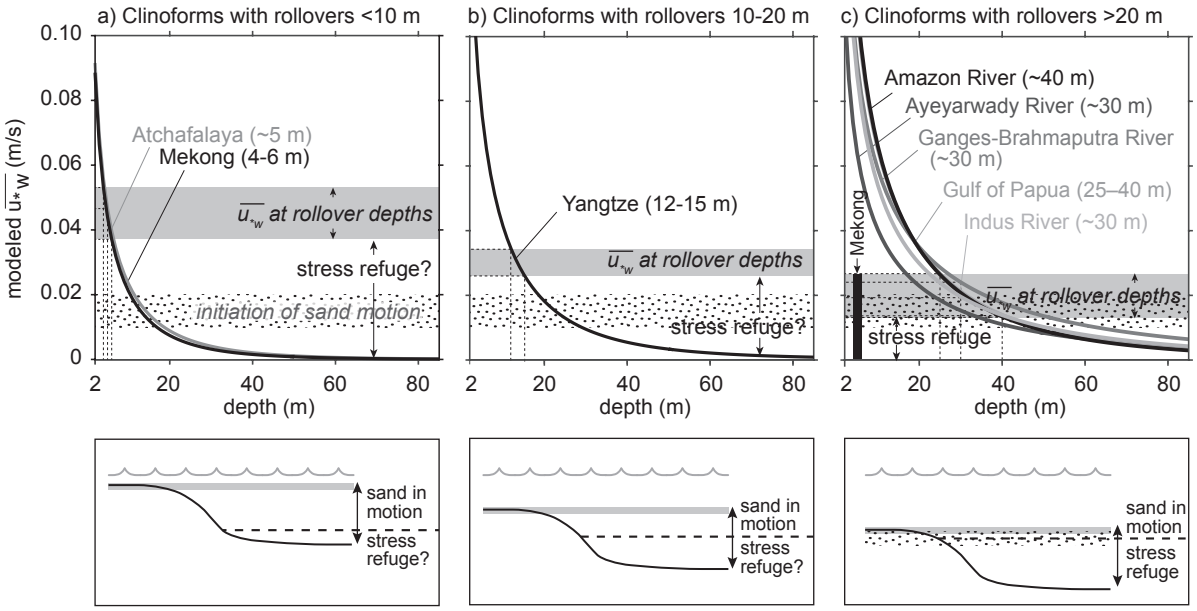

Figure 4.14: Modeled $\overline{u_{*w}}$ for eight tide-dominated and mixed-energy compound deltas. a) The Mekong and Atchafalaya deltas have shallower rollovers corresponding to $\overline{u_{*w}}$ = 0.037–0.053 m/s. b) The Yangtze Delta has an intermediate-depth rollover corresponding to $\overline{u_{*w}}$ = 0.026–0.034 m/s. c) The Amazon, Ayeyarwady, Ganges-Brahmaputra, Gulf of Papua, and Indus deltas have deeper rollovers corresponding to $\overline{u_{*w}}$ = 0.013–0.026 m/s. Overall $\overline{u_{*w}}$ are greater for the deeper systems in (c), but $\overline{u_{*w}}$ at rollover depths are smaller because of the location of the rollover in deeper water. Modeled $\overline{u_{*w}}$ at rollover depths exceed the threshold of motion for sand in the deeper systems (c). The clinoforms at right are more likely to offer a wave-current stress refuge for fine-grained sediment on the foreset.

channel, McLachlan et al., in press), the hypothetical clearance time of flocculated sediments from a 4-m thick plume would be ∼1.1 h, with an excursion distance of ∼1–3 km. Thus, in the high-flow season, most sediment exits the plume and enters the bottom boundary layer landward of the sites sampled here (Figure 4.3d, h). This inner-shelf (i.e., topset) delivery would be consistent with satellite observations of reduced plume SSC 20–30 km from shore (Wackerman et al., in press) and hypotheses about seasonal sediment storage on the topset (see references in Section 2.3). During the windy-monsoon season, plume concentrations were comparable to fluvial SSC but less than estuarine SSC (see McLachlan

et al., in press), consistent with hypotheses about seasonal re-import of sediment into the estuary (e.g., Wolanski et al., 1998).

4.5.2 Seasonal variability in near-bed sediment fluxes

Net across-shelf components of sediment flux were landward in both seasons (Figures 4.4, 4.5). Along-shelf components were northeastward during the high-discharge season and southwestward during the windy monsoon (Figures 4.4, 4.5). The seasonal switch in net along-shelf direction is consistent with seasonal wind and circulation patterns, and the asymmetric, along-shelf growth of the clinoform. The landward-dominant across-shelf sediment flux in both seasons may be an important factor controlling the across-shelf geometry, and is related to seasonal changes in current directions mediated by monsoon winds and river discharge. It should be noted here that the net fluxes were measured during deployments lasting 10 h 10 min to 12 h 20 min, and thus not equal to fluxes during an entire 12 h 25 min tidal cycle. For purposes of this discussion, they are assumed to represent the majority of sediment transport during similar tide and wave conditions (Figures 4.4, 4.5).

In the high-discharge season (Sep14), surface and nearbed currents peaked during ebb tide, and were directed eastward; these patterns are consistent with river-plume outflow enhanced by seasonal upwelling (Hordoir et al., 2006) and seasonal regional anticyclonic circulation (see Wyrtki, 1961 and Hu et al., 2000). Net sediment fluxes did not conform to the direction of peak current flow, however. In the cross-shelf direction, sediment fluxes were seaward for ∼3 h and landward for ∼9 h (Figure 4.4), consistent with nearbed return flow to compensate for seaward flow of the surface plume. In the along-shelf direction, sediment fluxes were northeastward for ∼7 h and southwestward for ∼5 h, consistent with the seasonal anticyclonic circulation in the East Sea (and/or weak southwest monsoon winds), as noted above. Thus, in Sep14, net sediment fluxes were landward and northeastward because of return flow under the rainy-season river plume and seasonal circulation patterns. Because seaward fluxes are limited during this period of intense delivery, sediment must be stored seasonally on the topset, as predicted for the Mekong (e.g., Wolanski et al., 1998) and measured

in other large-delta systems (e.g., Walsh et al., 2004; Ogston et al., 2008). The northeastward along-shelf fluxes are also worth noting; though the clinoform has grown asymmetrically toward the southwest, sediment does not necessarily take a direct path toward the Ca Mau Peninsula, but experiences excursions to the north during the high-discharge season. Assuming sediment remains in suspension during each tidal phase, excursion distances would be up to 3–4 km, based on the measured currents.

During the low-discharge/windy monsoon season (Mar15), net sediment fluxes were landward and southwestward (Figure 4.15a), and were driven by a very different set of seasonal forcing mechanisms. On the lower foreset and bottomset (Figure 4.5), near-bed currents and sediment fluxes were greatest during flood tides (Figure 4.4), though currents did not appear to be affected by wind-driven surface flow. The flood-dominant currents may have been produced by the large tidal prism entering the river during the low-discharge season, and/or by the regional cyclonic circulation. In large rivers feeding tidally dominated deltas, the propagation of the tidal wave into the channel can produce flood-dominant currents within the channel, i.e., flood-tide currents which are faster (but last for briefer periods) than ebb-tide currents (e.g., Geyer et al., 2000). This effect has been observed in the Dinh An channel in April, the low-discharge season (Nowacki et al., 2015; McLachlan et al., in press; Wolanski et al., 1998). It is unknown if tidal asymmetry in the river could translate directly to the foreset; however, the shift in peak flow from ebb tide (Sep14) to flood tide (Mar15) suggests a seasonal fluvial-tidal interaction that represents an important link between river dynamics and clinoform morphology.

In Mar15, sediment fluxes on the upper foreset were two orders of magnitude greater than those at the deeper sites, and were dominantly landward (related to the river-influenced current flows) with a strong southwestward component (Figure 4.15b). The southwestward/along-shelf component resulted from wind-driven surface currents and waves interacting with near-bed sediments, as proposed by Xu et al., 2010 and Loisel et al., 2014 and evidenced in water-column profiles (Figure 4.5). In Mar15, all three sites exhibited strong southwestward surface currents (Figure 4.5) consistent with the northeast windy monsoon (Wyrtki, 1961;

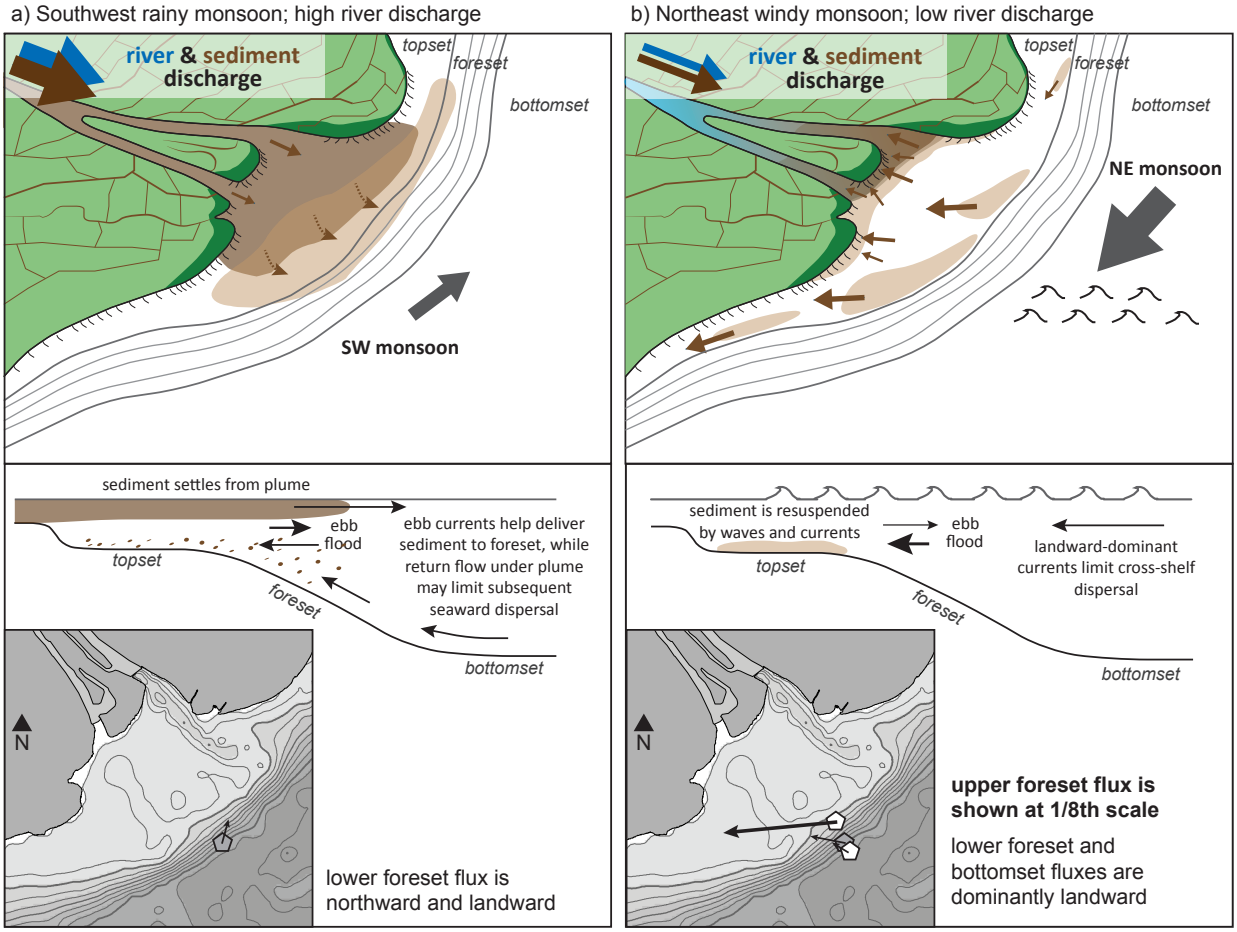

Figure 4.15: Conceptual diagrams of sediment transport patterns in two seasons, and scaled flux arrows. a) High river discharge coincides with weak southwest monsoon winds, and landward currents (return flow and/or seasonal upwelling currents) help retain sediment near-shore. b) Low river discharge and the windy northeast monsoon facilitate landward and southwestward current flow and sediment transport, especially on the topset.

Hu et al., 2000). But at the upper foreset site, these currents extended through most of the water column, and enhanced wave- and current-induced resuspension and transport, especially during the flooding tide (Figure 4.5). Thus, during the windy monsoon, sediment transport is more active, and sediments take a more direct path to distal depocenters near the Ca Mau Peninsula than in the rainy monsoon, when weak northward transport occurs.

In both seasons, near-bed SSC at water depths >12 m was small, which is unsurpris-

ing given the dominantly landward fluxes and rapid plume clearance (Figures 4.4, 4.5, 4.6). Even during ebb tides in the energetic monsoon (Mar15), near-bed SSC decreased abruptly between 8 and 12 m water depth (Figure 4.6, transect T2). Thus, in the Mekong system, sediment is not only stored on the topset during the high-discharge season, but also generally retained on the topset (albeit advected along isobath) during the energetic, windy monsoon season (Figure 4.15). This persistent retention of sediment near shore contrasts with systems like the Ganges-Brahmaputra, where sediment is transported beyond 20-m water depth during the high-flow season, possibly owing to seasonal increases in bed stresses, storms, and gravity flows (Segall and Kuehl, 1992; Barua et al., 1994; Wilson et al., 2015). For moderate-sized systems like the Gulf of Papua and Adriatic, delivery to the foreset is also common during energetic monsoons and winter storms, respectively (Martin et al., 2008; Puig et al., 2007).

It is important to note that this retention of sediment near shore appears to be primarily driven by current directions, rather than a loss in transport competency at the topset/foreset transition (i.e., the idea of a stress refuge; see section 4.1). Bed shear velocities on the lower foreset were greater in Mar15 than Sep14 (Figure 4.4), and bed shear velocities exceeded 0.02 m/s—if only briefly—at each depth sampled in Mar15 (Figure 4.5). Given a nominal critical shear velocity of ∼0.01–0.02 m/s for sand (e.g., Miller et al., 1977), sufficient energy should be available to mobilize muddy sediments at most foreset depths during the windy monsoon. The current directions, however, favor landward and southwestward transport.

4.5.3 Connections between observed sediment fluxes and the seabed

The sedimentary character of the Mekong clinoform generally reflects the observed transport dynamics. SARs are greatest at 4–16-m water depth (Figure 4.9c; see also DeMaster et al., in press), consistent with observations of decreasing SSC down-slope during the windy monsoon (Figures 4.5, 4.6). This focused deposition is common to large-river clinoforms (e.g., Pirmez et al., 1998) and consistent with the internal sigmoidal architecture of the Mekong (see Liu et al., in press) and other clinoforms. Physical laminations are prevalent at <10-m water depth

(Figure 4.8), consistent with rapid accumulation (Figure 4.9) and high bed stresses (Figure 4.5) measured on the upper foreset. Similar physical laminations exist on the topsets and upper foresets of other large-river clinoforms (Gulf of Papua, Martin et al., 2008; Amazon, Jaeger et al., 1995; Yangtze, Rhoads et al., 1985; Ganges-Brahmaputra, Segall and Kuehl, 1994), and have been attributed to wave and tidal reworking, and in some places gravity flows. Bioturbation is often suppressed in regions of energetic physical processes and/or rapid accumulation.

The progressive seaward fining of sediments from upper to lower foreset (Figure 4.7) reflects the concomitant decrease in shear velocities at the bed. Decreasing sediment sizes and shear velocities are accompanied by a transition from physical structures to mottled sediments and other evidence of bioturbation (Figure 4.8). Bioturbation is generally associated with environments where SAR is reduced (e.g., $<$2 cm/yr in general, Nittrouer et al., 1984; $\leq$4 cm/yr offshore of the Mississippi, Moore and Scruton, 1957). In the Mekong, foreset SAR is commonly $>$4 cm/yr (see also DeMaster et al., in press), but sediments lacking laminations in these zones (Figure 4.8) may be mixed by organisms between seasons of peak fluvial discharge, as on the Amazon inner shelf (see Kuehl et al., 1996). Bottomset SARs are small (Figure 4.9a, c) and may represent mixing of minor amounts of modern muddy sediment with relict sandy sediment; thus, these SARs are likely over-estimated.

In accordance with general models of clinoform growth, the Mekong topset (which was not sampled directly) is a zone of much sediment bypass over decadal timescales, and the foreset is a zone of rapid accumulation. The upper foreset is characterized by active sediment movement on tidal frequencies in all seasons, resulting in physical laminations that are preserved by rapid accumulation. In a seaward direction, the lower foreset and bottomset regions experience progressively reduced sediment delivery (Figure 4.6), decreased SARs, and increased evidence of bioturbation, as is typical of clinoforms (e.g., Amazon, Kuehl et al., 1986; Atchafalaya, Neill and Allison, 2005).

While not measured directly in this study, the role of gravity flows and storms should not be ignored for a system with such high accumulation rates and abundant physical structures.

Instrument observations (Figures 4.4, 4.5, 4.6) suggest that during fairweather conditions, most sediment flux occurs in less than ∼12 m water depth, and sufficient bed stress exists to mobilize sediments as large as sand. Under these conditions, combined wave-current effects likely produce physically laminated sediments, and accumulation rates are sufficiently great—at least to water depths of 12 m (see Figure 4.9)—to limit the effects of bioturbation. These fairweather processes may be insufficient, however, to produce the rapid accumulation observed at water depths of 12–16 m (Figure 4.9c; see also DeMaster et al., in press), as well as the apparent non-steady-state accumulation observed in some cores (Figure 4.10). Storm-generated waves are known to produce fluid muds and/or rapid seaward sediment fluxes in other large-delta systems, especially for those that lie farther from the equator than the Mekong at 9°N (e.g., Atchafalaya at 29.5°N, Jaramillo et al., 2009; Ganges-Brahmaputra at 22°N, Wilson et al., 2015). Increased transport energy related to, for example, seasonal wind patterns and spring tides (e.g., Gulf of Papua at 8°S; Martin et al., 2008) or storms (e.g., Atchafalaya; Allison et al., 2000) could produce gravity flows, physical structures, non-steady-state accumulation, and high accumulation rates on the foreset of the Mekong clinoform. Such processes can be non-uniform in space, and their signatures could be obscured by subsequent re-working, thus potentially explaining why no consistent pattern of non-steady-state accumulation was observed across the >160-km long study area.

4.5.4 Cross-shelf gradients in transport energy and the concept of a stress refuge

Bed stress is the fundamental control on clinoform rollover depth: topsets develop above the depth where available stress equals the critical stress required for sediment motion (e.g., Nittrouer et al., 1986; Pirmez et al., 1998). This simple dynamic is complicated by temporal and spatial variations in current and wave stresses, sediment size and supply, and bed properties (e.g., consolidation and armoring). In general, however, the division between topset and foreset is considered to represent a type of fairweather wave-current base, which lies above a stress refuge located on the foreset. In the Mekong system, modeled $\overline{u_*}$ values suggest that a stress refuge should only occur below depths of ∼7.5–19.5 m during the rainy monsoon, and

$\sim$17.5–19.5 m during the windy monsoon. This estimate is based on the intersection of the modeled $\overline{u_*}$ curve with a critical shear velocity of $\sim$1–2 cm/s, approximately the threshold of motion for sand ($u_{*cr,s}$; e.g., Miller et al., 1977). Thus, the Mekong clinoform should have a deeper rollover based on wave-current stresses, and so some other forcing mechanism—like current directions—must limit seaward sediment flux.

The absence of a classic stress refuge on the Mekong foreset may not be unique. A comparison of modeled $\overline{u_{*_w}}$ for the Mekong and seven other large-river clinoforms (Figure 4.14) highlights the disparity between available stresses and rollover depth for the shallow Mekong, Atchafalaya, and Yangtze clinoforms. (It is worth noting here that modeled $\overline{u_{*_w}}$ based on NWW3 is used because detailed wave and current data are not available for many of these subaqueous deltas. Using modeled $\overline{u_{*_w}}$ provides more conservative estimates of available stress that still demonstrate distinct patterns among deltas, though the estimates should not be over-interpreted since processes like wave-bed interaction may not be well-represented.) For the systems with rollovers $<$10 m (Mekong and Atchafalaya), $\overline{u_{*_w}}$ is much greater than $u_{*cr,s}$ at the rollover. For the Yangtze system with rollover at 12–15 m, $\overline{u_{*_w}}$ is moderately greater than $u_{*cr,s}$. And for the systems with rollovers at 25–40 m, $\overline{u_{*_w}}$ is nearly equal to $u_{*cr,s}$ at the rollover (Figure 4.14). Thus, for some clinoforms, high accumulation rates may occur in zones of considerable bed stress, and thus the foreset may not represent a classic stress refuge. For the Mekong example, annual sediment fluxes appear to converge between the topset and upper foreset, despite high bed stresses. Converging transport is key in this system, and is modulated by regional circulation as well as the interaction between currents and river outflow.

4.6 Conclusions

The subaqueous Mekong Delta, or clinoform, is an asymmetric, shore-hugging feature similar to the Adriatic Sea and Yangtze River clinoforms; however, it is distinguished among large-river deltas in that the topset-foreset transition occurs in shallow water depths of 4–6 m. Observations of sediment transport in Sep14 and Mar15 coupled with seabed sampling have

yielded the following key insights to sedimentary processes in this and other shallow clinoform systems.

- The river plume was observed at distances >20 km from the river mouth, with concentrations of ∼0.02 g/L; based on comparisons with fluvial SSC from other studies and estimated clearance rates, most fluvial sediment settles from the plume on the inner topset of the subaqueous delta.

- During the high-discharge season (Sep14), strong ebb-tide currents helped deliver sediment to the foreset, but long-duration flood-tide currents resulted in landward net sediment fluxes (during the brief deployment). This net flux direction is facilitated by return flow under the plume and/or seasonal circulation patterns, and helps retain sediment on the topset and make it available for re-import to the river during the low-discharge season.

- During the windy northeast monsoon (Mar15), peak sediment fluxes intensified and were dominantly landward toward the river channel and southwestward toward the Ca Mau peninsula. Southwestward fluxes were aided by wind-driven surface currents on the upper foreset, and were consistent with regional circulation patterns on the lower foreset and bottomset. Landward fluxes were likely a result of currents influenced by low river discharge.

- During both seasons, net observed fluxes (during the brief deployment periods) were landward, and SSCs seaward of the 12-m isobath were small. In general, seaward transport of sediment appears to be limited, though large foreset accumulation rates and evidence of non-steady-state accumulation suggest that seaward fluxes may be greater during more energetic periods. During windy monsoon conditions, intensified wave energy and wind-driven currents may facilitate seaward transport via gravity flows, as has been observed in other large-delta systems. Such conditions were not measured in this study due to time constraints.

- Annually averaged $\overline{u_*}$ and $\overline{u_{*_w}}$ exceeded the nominal shear velocities required for sand transport at most clinoform depths based on modeled tidal currents and wave climate, highlighting the competency of currents and waves to resuspend and erode sediment in this system.

- Maximum sediment accumulation rates occurred in 4–14-m water depth, and physical laminations were most prevalent at <10-m water depth; these patterns were predicted by the distributions of SSC and bed stress observed in the dynamical measurements, and demonstrate that the Mekong clinoform—despite having a shallow topset—fits the classic clinoform sedimentation model.

- A comparison of modeled $\overline{u_{*_w}}$ for shallow clinoforms (Mekong River and Atchafalaya River), an intermediate-depth clinoform (Yangtze), and deep clinoforms (Amazon River, Ayeyarwady River, Ganges-Brahmaputra River, Gulf of Papua, and Indus River) demonstrates that shallow topsets are not necessarily a product of weak bed stresses. Modeled stresses are greater on the topsets of shallow clinoforms, and therefore some additional forcing mechanism must be responsible for the evolution of these shallow systems. Observational data from the Mekong indicate that current directions, altered by seasonal changes in river flow and wind-driven circulation, are responsible for trapping sediment on the topset, despite the availability of sufficient bed stress for transport and erosion of silts and clays.

Though the Mekong Delta tidal range and wave climate are smaller/weaker than those of other large-river systems, current and wave stresses are sufficient to mobilize a variety of sediment sizes. In this and possibly other systems, the seasonal alteration of current directions related to river flow (both via the tidal prism entering the river during low flow and plume dynamics during high flow) appears to exert considerable control on the morphology of the subaqueous delta.

Chapter 5

SUMMARY

Sediment dispersal processes at the river-ocean transition are key to determining the ultimate marine sinks of terrestrial sediments. Because much fine-grained fluvial sediment enters the ocean through buoyant surface plumes, characterizing sediment clearance rates is an important first step in understanding and modeling coastal sediment transport. In Chapter 2, a simple 1D clearance model was applied to measurements from the Elwha River plume during dam removal. Effective and total effective settling velocities (w_e and $w_{e'}$) were calculated using a 1D clearance model applied to profiles of suspended-sediment concentrations and salinities. The results were used to evaluate the utility of the model, and to characterize the sediment-transport environment near the river mouth.

The clearance model was demonstrated to be a useful tool in this dynamic environment, especially when depth-integrated rather point measurements of SSC were used. Results obtained from estimated residence times ($t = x/u$) and modeled residence times (using streamlines) were similar, given a reasonable estimate of u for the former method. In practice, simple drifters could be used to obtain this estimate. Results also suggested that in practice, it is not critical to locate and follow a single streamline when sampling, so long as reasonable estimates of plume speed or modeled residence times are available.

Effective settling velocities were 0.041–0.66 mm/s in this system, and were comparable to or greater than values estimated for other small- and large-river plumes. Total effective settling velocities using modeled residence times were 0.13–3.5 mm/s, and were interpreted to reflect vertical gradients in sediment concentrations and mixing-induced removal that were not captured by the 1D-point method. Results were relatively insensitive to a variety of environmental parameters, except for river discharge; $w_{e'}$ tended to be greater during high-

discharge events, suggesting greater rates of sediment clearance given an increase in sediment supply.

This study adds to existing literature by suggesting that a simple 1D clearance model can be a useful tool for parameterizing clearance rates in diverse systems of different scales, including the nearfield zone of tidally forced plumes. For coastal systems where sediment plumes are to be incorporated into dispersal models, collecting a basic set of salinity and SSC measurements and calculating $w_{e'}$ seems a worthwhile effort, and an improvement on assuming a nominal settling velocity.

During extreme sediment-loading events like floods and landslides, buoyant sediment plumes from small mountainous rivers like the Elwha River may export sufficient sediment to form negatively buoyant hyperpycnal plumes or flows. Though these events are thought to be important transporters of sediment, few have been measured in situ. The event observed at the Elwha Delta between 2011 and 2014 in Chapter 3 did not fit classic models of hyperpycnal plumes or flows, insomuch as it was short-lived, transported and deposited substantial amounts of sand, was not obviously supercritical or directed downslope for more than about an hour, and had a short runout distance. The results from the Elwha study suggest that the duration and runout distance of hyperpycnal plumes or flows—and perhaps even the formation potential—may be limited by the sand content of the suspension. In other words, if a river carries sufficient suspended sediment to become negatively buoyant, but much of that suspended mass is sand, rapid deposition may lead to rapid flow extinction and a short runout distance.

The Elwha example also demonstrates that a gravity flow formed from a sand-mud mixture may yield a sorted deposit similar to deep-water massive sands observed on continental rises. This sorting may occur when the sand fraction of the suspension settles, leaving a mixture of brackish water and mud that rises upward to a point of neutral buoyancy. Signals consistent with a rising or mixing plume were observed in backscatter data from the Elwha event, in the hours after rapid bed aggradation occurred.

Though not sampled directly, the bed deposit was inferred to be dominantly sand based

on sediment-trap samples. In the three weeks after the event, this deposit was completely eroded, and the estimated τ_c needed for erosion was consistent with values used to model erosion of mixed mud/sand beds. The coarse nature of the deposit underscores the impressive capacity of tidal currents to erase the event record within just weeks of delivery. The absence of a long-term record suggests that in similarly energetic environments, interpretations of the stratigraphic record may under-estimate the frequency of gravity flows.

In larger deltaic systems, fluvial supply and dispersal tends to fluctuate on seasonal timescales, rather than in response to the type of punctuated storm events observed at the Elwha. And though waves and currents are important in re-working sediments, the supply generally overwhelms the erosion capacity of the system, allowing large subaqueous deposits to form. In the Mekong Delta example of Chapter 4, measurements of sediment fluxes on the subaqueous delta were contrasted from two seasons, and coupled with coring measurements and a simplistic wave model to evaluate sediment dispersal processes and morphologic evolution.

Based on sedimentary structures and accumulation rates observed in cores, the Mekong subaqueous delta fits the classic conceptual model of large-delta architecture and dynamics. The topset is a zone of moderate accumulation, where laminae are well-preserved. The foreset is a zone of rapid accumulation, where bioturbation destroys most of the physical structures. A simple model of wave climate was used to demonstrate that sufficient energy is available throughout the year for sand transport on the foreset; thus, it is surprising that the topset-foreset transition lies at shallow water depths of 4-6 m, relative to the 25-40-m-deep transition of many other large deltas.

During the high-discharge season, the surface plume delivers sediment to the topset and foreset, but return flow under the plume limits further seaward dispersal. During the windy northeast monsoon, currents associated with regional circulation (at greater depths) and winds (at lesser depths) drive intense southwestward and landward sediment fluxes. These monsoon-driven transport patterns help make sediment available for re-import to the river, and facilitate along-shore growth of the clinoform (see references in Chapter 4). The net

landward flux directions measured in both seasons suggests a flux convergence mechanism whereby the topset exists in dynamic equilibrium at unusually shallow depths.

Together, these observations from two contrasting fluvial-marine dispersal systems offer insights into tools for measuring sediment dispersal processes, diverse pathways of sediment transfer, and morphodynamics mediated by interrelated transport processes. This work adds to a growing and evolving body of knowledge about our coastlines, and the complex processes that shape them.

BIBLIOGRAPHY

Alexander, C.R., DeMaster, D.J., Nittrouer, C.A., 1991. Sediment accumulation in a modern epicontinental-shelf setting: The Yellow Sea. Mar. Geol. 98, 51–72. doi:10.1016/0025-3227(91)90035-3

Alexander, J., Mulder, T., 2002. Experimental quasi-steady density currents. Mar. Geol., 186, 195–210. https://doi.org/10.1016/S0025-3227(02)00313-4

Allison, M.A., Kineke, G.C., Gordon, E.S., Goni, M.A., 2000. Development and reworking of a seasonal flood deposit on the inner continental shelf off the Atchafalaya River. Cont. Shelf Res. 20, 2267–2294.

Amos, C.L., Feeney, T., Sutherland, T.F., Luternauer, J.L., 1997. The stability of fine-grained sediments from the Fraser River Delta. Estuar. Coast. Shelf Sci. 45, 507–524. doi:10.1006/ecss.1996.0193

Anderson, F.E., 1968. Seaward terminus of the Vashon continental glacier in the Strait of Juan de Fuca. Mar. Geol. 6, 419–438. https:///doi.org/10.1016/0025-3227(68)90024-8

Anikiyev, V.V., Zaytsev, O.V., Hieu, T.T., Savil'yeva, I.I., Stardodubtsev, Y.G., Shumilin, Y.N., 1986. Variation in the space-time distribution of suspended matter in the coastal zone of the Mekong River. Oceanology 26, 725–729.

Anthony, E.J., Brunier, G., Besset, M., Goichot, M., Dussouillez, P., Nguyen, V.L., 2015. Linking rapid erosion of the Mekong River delta to human activities. Sci. Rep. 5, 1–12. doi:10.1038/srep14745

Aslan, A., White, W.A., Warne, A.G., Guevara, E.H., 2003. Holocene evolution of the western Orinoco Delta, Venezuela. Bull. Geol. Soc. Am. 115, 479–498. doi:10.1130/0016-7606(2003)115<0479:HEOTWO>2.0.CO;2

Ayranci, K., Lintern, D. G., Hill, P. R., Dashtgard, S. E., 2012. Tide-supported gravity

flows on the upper delta front, Fraser River delta, Canada. Marine Geology, 326–328, 166–170. https://doi.org/10.1016/j.margeo.2012.09.007

Bainbridge, Z.T., Wolanski, E., Alvarez-Romero, J.G., Lewis, S.E., Brodie, J.E., 2012. Fine sediment and nutrient dynamics related to particle size and floc formation in a Burdekin River flood plume, Australia. Mar. Pollut. Bull. 65, 236–48. doi:10.1016/j.marpolbul.2012.01.043

Barua, D.K., Kuehl, S.A., Miller, R.L., Moore, W.S., 1994. Suspended sediment distribution and residual transport in the coastal ocean off the Ganges-Brahmaputra river mouth. Mar. Geol. 120, 41–61.

Bates, C.C., 1953. Rational theory of delta formation. Am. Assc. of Pet. Geol., 37, 2119–2162.

Blum, P., 1997. Physical properties handbook: A guide to the shipboard measurement of physical properties of deep-sea cores. ODP Tech. Note, 26. Accessed 27 Mar 2017, http://www-odp.tamu.edu/publications/tnotes/tn26/TOC.HTM

Bouma, A.H., 2000. Coarse-grained and fine-grained turbidite systems as end member models: Applicability and dangers. Mar. Pet. Geol. 17, 137–143. doi:10.1016/S0264-8172(99)00020-3

Bowen, A.J., Normark, W.R., Piper, D.J.W., 1984. Modelling of turbidity currents on Navy submarine fan, California continental borderland. Sedimentology 31, 169–185.

Brunier, G., Anthony, E.J., Goichot, M., Provansal, M., Dussouillez, P., 2014. Recent morphological changes in the Mekong and Bassac river channels, Mekong delta: The marked impact of river-bed mining and implications for delta destabilisation. Geomorphology 224, 177–191. doi:10.1016/j.geomorph.2014.07.009

Burban, P.-Y., Lick, W., Lick, J., 1989. The flocculation of fine-grained sediments in estuarine waters. Journal of Geophysical Research 94, 8323–8330.

Bursik, M.I., 1995. Theory of the sedimentation of suspended particles from fluvial plumes. Sedimentology 42, 831–838.

Caine, S., 2007. AQUAscat1000 Matlab Toolkit. Aquatec Group document 910-5000, rev.

1.01.

Carter, L., Milliman, J.D., Talling, P.J., Gavey, R., Wynn, R.B., 2012. Near-synchronous and delayed initiation of long run-out submarine sediment flows from a record-breaking river flood, offshore Taiwan. Geophys. Res. Lett. 39, 6–10. doi:10.1029/2012GL051172

Carter, L., Orpin, A.R., Kuehl, S.A., 2010. From mountain source to ocean sink - the passage of sediment across an active margin, Waipaoa Sedimentary System, New Zealand. Mar. Geol. 270, 1–10. doi:10.1016/j.margeo.2009.12.010

Cattaneo, A., Trincardi, F., Asioli, A., Correggiari, A., 2007. The Western Adriatic shelf clinoform: energy-limited bottomset. Cont. Shelf Res. 27, 506–525. doi:10.1016/j.csr.2006.11.013

Chiang, C.-S., Yu, H.-S., 2008. Evidence of hyperpycnal flows at the head of the meandering Kaoping Canyon off SW Taiwan. Geo-Marine Lett. 28, 161–169.

Clare, M.A., Hughes Clarke, J.E., Talling, P.J., Cartigny, M.J.B., Pratomo, D.G., 2016. Preconditioning and triggering of offshore slope failures and turbidity currents revealed by most detailed monitoring yet at a fjord-head delta. Earth Planet. Sci. Lett. 450, 208–220. doi:10.1016/j.epsl.2016.06.021

Coleman, J.M., Prior, D.B., 1982. Deltaic Environments of Deposition, in: Scholle, P.A., Spearing, D., Eds., Sandstone Depositional Environments. AAPG Mem., 31, 139–178.

Curran, C.A., Konrad, C.P., Higgins, J.L., Bryant, M.K., 2009. Estimates of Sediment Load Prior to Dam Removal in the Elwha River, Clallam County, Washington. USGS Scientific Investigations Report 2009-5221.

Curran, C.A., Magirl, C.S., Duda, J.J., 2014. Suspended-sediment concentration during dam decommissioning in the Elwha River, Washington: U.S. Geological Survey Data Set (http://wa.water.usgs.gov/pubs/misc/elwha/ssc/). doi:10.5066/F7M043DB.

Curran, K.J., Hill, P.S., Milligan, T.G., 2002. Fine-grained suspended sediment dynamics in the Eel River flood plume. Cont. Shelf Res. 22, 2537–2550.

Curran, K.J., Hill, P.S., Milligan, T.G., 2003. Time variation of floc properties in a settling column. J. Sea Res. 49, 1–9. doi:10.1016/S1385-1101(02)00195-8

Dagg, M., Benner, R., Lohrenz, S., Lawrence, D., 2004. Transformation of dissolved and particulate materials on continental shelves influenced by large rivers: Plume processes. Cont. Shelf Res. 24, 833–858. doi:10.1016/j.csr.2004.02.003

Darby, S.E., Hackney, C.R., Leyland, J., Kummu, M., Lauri, H., Parsons, D.R., Best, J.L., Nicholas, A.P., Aalto, R., 2016. Fluvial sediment supply to a mega-delta reduced by shifting tropical-cyclone activity. Nature 539, 276–279. doi:10.1038/nature19809

Deines, K.L., 1999. Backscatter estimation using Broadband acoustic Doppler current profilers. Proc. IEEE Sixth Work. Conf. Curr. Meas. (Cat. No.99CH36331) 249–253. doi:10.1109/CCM.1999.755249

DeMaster, D.J., Liu, J.P., Eidam, E.F., Nittrouer, C.A., Nguyen, T.T., in press. Determining rates of sediment accumulation on the Mekong Shelf: Timescales, steady-state assumptions, and radiochemical tracers. Cont. Shelf Res.

Dippner, J.W., Nguyen, K.V., Hein, H., Ohde, T., Loick, N., 2006. Monsoon-induced upwelling off the Vietnamese coast. Ocean Dyn. 57, 46–62. doi:10.1007/s10236-006-0091-0

Downing, J., 2006. Twenty-five years with OBS sensors: The good, the bad, and the ugly. Cont. Shelf Res. 26, 2299–2318. doi:10.1016/j.csr.2006.07.018

Driscoll, N.W., Karner, G.D., 1999. Three-dimensional quantitative modeling of clinoform development. Mar. Geol. 154, 383–398. doi:10.1016/S0025-3227(98)00125-X

Duda, J.J., Freilich, J.E., Schreiner, E.G., Service, N.P., Park, O.N., Avenue, E.P., Angeles, P., 2008. Baseline Studies in the Elwha River Ecosystem Prior to Dam Removal: Introduction to the Special Issue. Northwest Sci., 82, 1–12.

Eidam, E.F., Ogston, A.S., Nittrouer, C.A., Warrick, J.A., 2016. Tidally dominated sediment dispersal offshore of a small mountainous river: Elwha River, Washington State. Cont. Shelf Res., 116, 136–148.

Eisma, D., 1986. Flocculation and de-flocculation of suspended matter in estuaries. Netherlands J. Sea Res. 20, 183–199.

Eisma, D., 1993. Suspended Matter in the Aquatic Environment. Berlin: Springer-Verlag, 315 pp.

Fang, W., Fang, G., Shi, P., Huang, Q., Xie, Q., 2002. Seasonal structures of upper layer circulation in the southern South China Sea from in situ observations. J. Geophys. Res. 107. doi:10.1029/2002JC001343

Felix, M., Peakall, J., McCaffrey, W.D., 2006. Relative importance of processes that govern the generation of particulate hyperpycnal flows. J. Sediment. Res. 76, 382–387. doi:10.2110/jsr.2006.022

Fissel, D.B., and Huggett, W.S., 1976. Observations of currents, bottom pressures and densities through a cross-sections of Juan de Fuca Strait. Pacific Marine Science Report 76–6, Institute of Ocean Sciences, Patricia Bay, Victoria.

Foley, M.M., Duda, J.J., Beirne, M.M., Paradis, R., Ritchie, A., Warrick, J.A., 2015. Rapid water quality change in the Elwha River estuary complex during dam removal. Limnol. Oceanogr. 60, 1719–1732. doi:10.1002/lno.10129

Foley, M.M., Warrick, J.A., Ritchie, A., Stevens, A.W., Shafroth, P.B., Duda, J.J., Beirne, M.M., Paradis, R., Gelfenbaum, G., McCoy, R., Cubley, E.S., in press. Coastal habitat and biological community response to dam removal on the Elwha River. Ecological Monographs.

Foley, M.M., Warrick, J.A., in press. Ephemeral seafloor sedimentation during dam removal: Elwha River, Washington. Cont. Shelf Res.

Gagliano, S.M., McIntire, W.G., 1968. Reports on the Mekong River Delta. Coastal Studies Institute, Technical Report No. 57, Baton Rouge, Louisiana.

García, M.H., 1993. Hydraulic jumps in sediment-driven bottom currents. J. Hydraul. Eng. 119, 1094–1117. doi:10.1061/(ASCE)0733-9429(1993)119:10(1094)

Garvine, R.W., 1982. A steady state model for buoyant surface plume hydrodynamics in coastal waters. Tellus 34, 293–306. doi:10.3402/tellusa.v34i3.10813

Garvine, R.W., 1995. A dynamical system for classifying buoyant coastal discharges. Cont. Shelf Res. 15, 1585–1596. doi:10.1016/0278-4343(94)00065-U

Gelfenbaum, G., Stevens, A.W., Elias, E., Warrick, J.A., 2009. Modeling sediment transport and delta morphology on the dammed Elwha River, Washington State, USA. Proceed-

ings, Coastal Dynamics 2009, Paper No. 109.

Gelfenbaum, G., Stevens, A.W., Miller, I., Warrick, J.A., Ogston, A.S., Eidam, E., 2015. Large-scale dam removal on the Elwha River, Washington, USA: Coastal geomorphic change. Geomorphology, 246, 649–668. http://dx.doi.org/10.1016/j.geomorph.2015.01.002.

Geyer, W.R., Hill, P., Milligan, T., Traykovski, P., 2000. The structure of the Eel River plume during floods. Cont. Shelf Res. 20, 2067–2093. doi:10.1016/S0278-4343(00)00063-7

Geyer, W.R., Hill, P.S., Kineke, G.C., 2004. The transport, transformation and dispersal of sediment by buoyant coastal flows. Cont. Shelf Res. 24, 927–949. doi:10.1016/j.csr.2004.02.006

Geyer, W.R., Smith, J.D., 1987. Shear instability in a highly stratified estuary. J. Phys. Oceanogr. 17, 1668–1679.

Gibbs, R.J., Matthews, M.D., Link, D.A., 1971. The relationship between sphere size and settling velocity. Jour. Sed. Res. 41, 7–18.

Gibbs, R.J., 1985. Estuarine flocs: Their size, settling velocity and density. J. Geophys. Res. 90, 3249–3251. doi:10.1029/JC090iC02p03249

Gilbert, J.D., Link, R.A., 1995. Alluvium distribution in Lake Mills, Glines Canyon Project, and Lake Aldwell, Elwha project, Washington: Boise, Idaho, Bureau of Reclamation, Elwha Technical Series PN-95-459, 61 pp.

Giosan, L., Constantinescu, S., Clift, P.D., Tabrez, A.R., Danish, M., Inam, A., 2006. Recent morphodynamics of the Indus delta shore and shelf. Cont. Shelf Res. 26, 1668–1684. doi:10.1016/j.csr.2006.05.009

Girard, F., Ghienne, J.-F., Rubino, J.-L., 2012. Occurrence of hyperpycnal flows and hybrid event beds related to glacial outburst events in a late Ordovician proglacial delta (Murzuq Basin, SW Libya). J. Sediment. Res. 82, 688–708. doi:10.2110/jsr.2012.61

Gladstone, C., Pritchard, D., 2010. Patterns of deposition from experimental turbidity currents with reversing buoyancy. Sedimentology 57, 53–84. doi:10.1111/j.1365-3091.2009.01087.x

Goldfinger, C., Nelson, C.H., Morey, A.E., Johnson, J.E., Patton, J.R., Karabanov, E., Gutierrez-Pastor, J., Eriksson, A.T., Gracia, E., Dunhill, G., Enkin, R.J., Dallimore, A., Vallier, T., 2012. Turbidite Event History —Methods and Implications for Holocene Paleoseismicity of the Cascadia Subduction Zone. U.S. Geol. Surv. Prof. Pap. 170 pp.

Goodbred, S.L., Kuehl, S.A., 1999. Holocene and modern sediment budgets for the Ganges-Brahmaputra river system: Evidence for highstand dispersal to flood-plain, shelf, and deep-sea depocenters. Geology 27, 559–562. doi:10.1130/0091-7613(1999)027<0559:HAMSBF>2.3.CO;2

Goodbred, S.L., Saito, Y., 2012. Tide-Dominated Deltas, in: Davis, R.A. Jr., Dalrymple, R.W., Eds., Principles of Tidal Sedimentology. Springer, New York, pp. 129–149.

Gugliotta, M., Saito, Y., Nguyen, V.L., Ta, T.K.O., Nakashima, R., Tamura, T., Uehara, K., Katsuki, K., Yamamoto, S., in press. Process regime, salinity, morphological, and sedimentary trends along the fluvial to marine transition zone of the mixed-energy Mekong River delta, Vietnam. Cont. Shelf Res.

Hale, R.P., Ogston, A.S., Walsh, J.P., Orpin, A.R., 2014. Sediment transport and event deposition on the Waipaoa River Shelf, New Zealand. Cont. Shelf Res. 86, 52–65. doi:10.1016/j.csr.2014.01.009

Hanebuth, T.J.J., Proske, U., Saito, Y., Nguyen, V.L., Ta, T.K.O., 2012. Early growth stage of a large delta—Transformation from estuarine-platform to deltaic-progradational conditions (the northeastern Mekong River Delta, Vietnam). Sediment. Geol. 261–262, 108–119. doi:10.1016/j.sedgeo.2012.03.014

Hanebuth, T.J.J., Stattegger, K., 2003. The stratigraphic evolution of the Sunda Shelf during the past fifty thousand years, in: Sidi, F.H., Nummedal, D., Imbert, P., Darman, H., Posamentier, W., Eds., Tropical Deltas of Southeast Asia—Sedimentology, Stratigraphy, and Petroleum Geology. pp. 189–200.

Hill, P.S., Milligan, T.G., Geyer, W.R., 2000. Controls on effective settling velocity of suspended sediment in the Eel River flood plume. Cont. Shelf Res. 20, 2095–2111.

Hordoir, R., Nguyen, K.D., Polcher, J., 2006. Simulating tropical river plumes, a set of

parametrizations based on macroscale data: A test case in the Mekong Delta region. J. Geophys. Res. 111, 1–18. doi:10.1029/2005JC003392

Hori, K., Saito, Y., Zhao, Q., Wang, P.P., Quanhong, Z., 2002. Architecture and evolution of the tide-dominated Changjiang (Yangtze) River delta, China. Sediment. Geol. 146, 249–264. doi:http://dx.doi.org/10.1016/S0037-0738(01)00122-1

Hu, J., Kawamura, H., Hong, H., Qi, Y., 2000. A review on the currents in the South China Sea: Seasonal circulation, South China Sea warm current and Kuroshio intrusion. J. Oceanogr. 56, 607–624. doi:10.1023/A:1011117531252

Hughes Clarke, J.E., 2016. First wide-angle view of channelized turbidity currents links migrating cyclic steps to flow characteristics. Nat. Commun. 7:11896. doi:10.1038/ncomms 11896

Imamura, F., To, D.V., 1997. Flood and Typhoon Disasters in Viet Nam in the Half Century Since 1950. Nat. Hazards 15, 71–87.

Imran, J., Syvitski, J., 2000. Impact of Extreme River Events on the Coastal Ocean. Oceanography 13, 85–92. doi:10.5670/oceanog.2000.17

Jaeger, J.M., Nittrouer, C.A., 1995. Tidal controls on the formation of fine-scale sedimentary strata near the Amazon river mouth. Mar. Geol. 125, 259–281. doi:10.1016/0025-3227(95)00015-Q

Jaramillo, S., Sheremet, A., Allison, M.A., Reed, A.H., Holland, K.T., 2009. Wave-mud interactions over the muddy Atchafalaya subaqueous clinoform, Louisiana, United States: Wave-supported sediment transport. J. Geophys. Res. 114, 1–18. doi:10.1029/2008JC004821

Johnson, K.S., Paull, C.K., Barry, J.P., Chavez, F.P., 2001. A decadal record of underflows from a coastal river into the deep sea. Geology 29, 1019–1022. doi:10.1130/0091-7613(2001)029<1019:ADROUF>2.0.CO;2

Kao, S.J., Dai, M., Selvaraj, K., Zhai, W., Cai, P., Chen, S.N., Yang, J.Y.T., Liu, J.T., Liu, C.C., Syvitski, J.P.M., 2010. Cyclone-driven deep sea injection of freshwater and heat by hyperpycnal flow in the subtropics. Geophys. Res. Lett. 37, 1–5. doi:10.1029/

2010GL044893

Khelifa, A., Hill, P.S., 2006. Models for effective density and settling velocity of flocs. J. Hydraul. Res. 44, 390–401. doi:10.1080/00221686.2006.9521690

Kim, Y.H., Voulgaris, G., 2003. Estimation of suspended sediment concentration in estuarine environments using Acoustic Backscatter from an ADCP. Proc. Coast. Sediment 03, 1–10. doi:10.1121/1.397061

Kineke, G.C, Woolfe, K.J, Kuehl, S.A, Milliman, J.D, Dellapenna, T.M, Purdon, R.G, 2000. Sediment export from the Sepik River, Papua New Guinea: evidence for a divergent sediment plume. Cont. Shelf Res. 20, 2239–2266. doi:10.1016/S0278-4343(00)00069-8

Kineke, G.C., Sternberg, R.W., 1989. The effect of particle settling velocity on computed suspended sediment concentration profiles. Mar. Geol. 90, 159–174. doi:10.1016/0025-3227(89)90039-X

Kineke, G.C., Sternberg, R.W., Trowbridge, J.H., 1996. Fluid-mud processes on the Amazon continental shelf. Cont. Shelf Res. 16, 667–696.

Kneller, B.C, Buckee, C., 2000. The structure and fluid mechanics of turbidity currents: a review of some recent studies and their geological implications. Sedimentology 47, 62–94. doi:10.1046/j.1365-3091.2000.047s1062.x

Kneller, B.C., Bennett, S.J., McCaffrey, W.D., 1999. Velocity structure, turbulence and fluid stresses in experimental gravity currents. J. Geophys. Res. 104. doi:10.1029/1998JC900077

Komar, P.D., 1971. Hydraulic jumps in turbidity currents. Geol. Soc. Am. Bull., 82, 1477–1488.

Kondolf, G.M., Annandale, G., Rubin, Z., 2015. Sediment starvation from dams in the Lower Mekong River Basin: magnitude of the effect and potential mitigation opportunities, in: E-Proceedings of the 36th IAHR World Congress. The Hague, the Netherlands, pp. 1–7. doi:http://89.31.100.18/ iahrpapers/88661.pdf

Kondolf, G.M., Rubin, Z.K., Minear, J.T., 2014. Dams on the Mekong: Cumulative sediment starvation. Water Resour. Res. 50, 5158–5169. doi:10.1002/2013WR014910.

Kranck, K., 1980. Experiments on the significance of flocculation in the settling of fine-grained sediment in still water. Can. J. Earth Sci. 17, 1517–1526.

Kuehl, S.A., DeMaster, D.J., Nittrouer, C.A., 1986. Nature of sediment accumulation on the Amazon continental shelf. Cont. Shelf Res. 6, 209–225.

Kuehl, S.A., Hariu, T.M., Moore, W.S., 1989. Shelf sedimentation off the Ganges-Brahmaputra river system: Evidence for sediment bypassing to the Bengal fan. Geol. 17, 1132–1135. doi:10.1130/0091-7613(1989)017<1132

Kuehl, S.A., Levy, B.M., Moore, W.S., Allison, M.A., 1997. Subaqueous delta of the Ganges-Brahmaputra river system. Mar. Geol. 144, 81–96. doi:10.1016/S0025-3227(97)00075-3

Kuehl, S.A., Nittrouer, C.A., Allison, M.A., Faria, L.E.C., Dukat, D.A., Jaeger, J.M., Pacioni, T.D., Figueiredo, A.G., Underkoffler, E.C., 1996. Sediment deposition, accumulation, and seabed dynamics in an energetic fine-grained coastal environment. Cont. Shelf Res. 16, 787–815. doi:10.1016/0278-4343(95)00047-X

Kummu, M., Lu, X.X., Wang, J.J., Varis, O., 2010. Basin-wide sediment trapping efficiency of emerging reservoirs along the Mekong. Geomorphology 119, 181–197. doi:10.1016/j.geomorph.2010.03.018

Lamb, M.P., Mohrig, D., 2009. Do hyperpycnal-flow deposits record river-flood dynamics? Geology 37, 1067–1070. doi:10.1130/G30286A.1

Li, G., Wei, H., Yue, S., Cheng, Y., Han, Y., 1998. Sedimentation in the Yellow River delta, Part II: Suspended sediment dispersal and deposition on the subaqueous delta. Mar. Geol. 149, 113–131. doi:10.1016/S0025-3227(98)00032-2

Liu, J., Saito, Y., Wang, H., Yang, Z., Nakashima, R., 2007. Sedimentary evolution of the Holocene subaqueous clinoform off the Shandong Peninsula in the Yellow Sea. Mar. Geol. 236, 165–187. doi:10.1016/j.margeo.2006.10.031

Liu, J.P., DeMaster, D.J., Nittrouer, C.A., Eidam, E.F., Nguyen, T.T., in press. A seismic study of the Mekong subaqueous delta: Proximal versus distal accumulation. Cont. Shelf Res.

Liu, J.P., Li, A.C., Xu, K.H., Velozzi, D.M., Yang, Z.S., Milliman, J.D., DeMaster, D.J.,

2006. Sedimentary features of the Yangtze River-derived along-shelf clinoform deposit in the East China Sea. Cont. Shelf Res. 26, 2141–2156. doi:10.1016/j.csr.2006.07.013

Liu, J.P., Xue, Z., Ross, K., Wang, H.J., Yang, S., Li, A.C., Gao, S., 2009. Fate of sediments delivered to the sea by Asian large rivers: Long-distance transport and formation of remote alongshore clinothems. The Sedimentary Record 7, 4–9.

Liu, Z., Yang, H., Liu, Q., 2001. Regional dynamics of seasonal variability in the South China Sea. J. Phys. Oceanogr. 31, 272–284. doi:10.1175/1520-0485(2001)031<0272:rdosvi> 2.0.co;2

Lohrenz, S.E., Fahnenstiel, G.L., Redalje, D.G., Lang, G.A., Dagg, M.J., Whitledge, T.E., Dortch, Q., 1999. Nutrients, irradiance, and mixing as factors regulating primary production in coastal waters impacted by the Mississippi River plume. Cont. Shelf Res. 19, 1113–1141. doi:10.1016/S0278-4343(99)00012-6

Loisel, H., Mangin, A., Vantrepotte, V., Dessailly, D., Dinh, D.N., Garnesson, P., Ouillon, S., Lefebvre, J.-P., Mériaux, X., Phan, T.M., 2014. Variability of suspended particulate matter concentration in coastal waters under the Mekong's influence from ocean color (MERIS) remote sensing over the last decade. Remote Sens. Environ. 150, 218–230. doi:10.1016/j.rse.2014.05.006

Lønne, I., Nemec, W., 2004. High-arctic fan delta recording deglaciation and environment disequilibrium. Sedimentology 51, 553–589. doi:10.1111/j.1365-3091.2004.00636.x

Lu, X.X., Siew, R.Y., 2006. Water discharge and sediment flux changes in the Lower Mekong River. Hydrol. Earth Syst. Sci. Discuss. 2, 2287–2325. doi:10.5194/hessd-2-2287-2005

Lynch, J.F., Irish, J.D., Sherwood, C.R., Agrawal, Y.C., 1994. Determining suspended sediment particle size information from acoustical and optical backscatter measurements. Continental Shelf Research, 14, 1139–1165.

Ma, Y., Wright, L.D., Friedrichs, C.T., 2008. Observations of sediment transport on the continental shelf off the mouth of the Waiapu River, New Zealand: Evidence for current-supported gravity flows. Cont. Shelf Res. 28, 516–532. doi:10.1016/j.csr.2007.11.001

Madsen, O.S., 1994. Spectral Wave-Current Bottom Boundary Layer Flows, in: Proceed-

ings of the 24th International Conference on Coastal Engineering. Coastal Engineering Research Council/ASCE, Kobe, Japan. pp. 384–398. doi:10.9753/icce.v24.

Magirl, C.S., Hilldale, R.C., Curran, C.A., Duda, J.J., Straub, T.D., Domanski, M., Foreman, J.R., 2015. Large-scale dam removal on the Elwha River, Washington, USA: Fluvial sediment load. Geomorphology 246, 669–686. http://dx.doi.org/10.1016/j.geomorph.2014.12.032.

Manh, N. V., Dung, N.V., Hung, N.N., Kummu, M., Merz, B., Apel, H., 2015. Future sediment dynamics in the Mekong Delta floodplains: Impacts of hydropower development, climate change and sea level rise. Glob. Planet. Change 127, 22–33. doi:10.1016/j.gloplacha.2015.01.001

Mantovanelli, A., Ridd, P.V., 2006. Devices to measure settling velocities of cohesive sediment aggregates: A review of the in situ technology. J. Sea Res. 56, 199–226. doi:10.1016/j.seares.2006.05.002

Martin, D.P., Nittrouer, C.A., Ogston, A.S., Crockett, J.S., 2008. Tidal and seasonal dynamics of a muddy inner shelf environment, Gulf of Papua. J. Geophys. Res. 113, 1–18. doi:10.1029/2006JF000681

McCool, W.W., Parsons, J.D., 2004. Sedimentation from buoyant fine-grained suspensions. Cont. Shelf Res. 24, 1129–1142. doi:10.1016/j.csr.2004.03.009

McKee, B.A., Nittrouer, C.A., DeMaster, D.J., 1983. Concepts of sediment deposition and accumulation applied to the continental shelf near the mouth of the Yangtze River. Geology 11, 631–633. doi:10.1130/0091-7613(1983)11<631

McLachlan, R.L., Ogston, A.S., Allison, M.A., in press. Implications of tidally varying bed stress and intermittent estuarine stratification on fine-sediment dynamics through the Mekong's tidal river to estuarine reach. Cont. Shelf Res.

Middleton, G., 1993. Sediment deposition from turbidity currents. Annu. Rev. Earth Planet. Sci. 21, 89–114.

Mikkelsen, O.A., Hill, P.S., Milligan, T.G., 2006. Single-grain, microfloc and macrofloc volume variations observed with a LISST-100 and a digital floc camera. J. Sea Res. 55,

87–102. doi:10.1016/j.seares.2005.09.003

Mikkelsen, O.A., Hill, P.S., Milligan, T.G., 2007. Seasonal and spatial variation of floc size, settling velocity, and density on the inner Adriatic Shelf (Italy). Cont. Shelf Res. 27, 417–430. doi:10.1016/j.csr.2006.11.004

Miller, M.C., McCave, I.N., Komar, P.D., 1977. Threshold of sediment motion under unidirectional currents. Sedimentology 24, 507–527.

Milligan, T.G., 1995. An examination of the settling behaviour of a flocculated suspension. Netherlands J. Sea Res. 33, 163–171. doi:10.1016/0077-7579(95)90003-9

Milligan, T.G., Hill, P.S., 1998. A laboratory assessment of the relative importance of turbulence, particle composition, and concentration in limiting maximal floc size and settling behaviour. J. Sea Res. 39, 227–241. doi:10.1016/S1385-1101(97)00062-2

Milligan, T.G., Hill, P.S., Law, B.A., 2007. Flocculation and the loss of sediment from the Po River plume. Cont. Shelf Res. 27, 309–321. doi:10.1016/j.csr.2006.11.008

Milliman, J.D., Farnsworth, K.L., 2011. River Discharge to the Coastal Ocean: A Global Synthesis. Cambridge University Press, Cambridge.

Milliman, J.D., Farnsworth, K.L., Albertin, C.S., 1999. Flux and fate of fluvial sediments leaving large islands in the East Indies. J. Sea Res. 41, 97–107. doi:10.1016/S1385-1101(98)00040-9

Milliman, J.D., Kao, S.J., 2005. Hyperpycnal discharge of fluvial sediment to the ocean: Impact of super-typhoon Herb (1996) on Taiwanese rivers. J. Geol. 113, 503–516.

Milliman, J.D., Meade, R.H., 1983. World-wide delivery of river sediment to the oceans. J. Geol. 91, 1–21.

Mitchener, H., Torfs, H., 1996. Erosion of mud/sand mixtures. Coast. Eng. 29, 1–25.

Moore, D.G., Scruton, P.C., 1957. Minor internal structures of some recent unconsolidated sediments. Bulletin of the American Association of Petroleum Geologists 41, 2723–2751.

Morehead, M.D., Syvitski, J.P., 1999. River-plume sedimentation modeling for sequence stratigraphy: application to the Eel margin, northern California. Mar. Geol. 154, 29–41.

MRC (Mekong River Commission), 2005. Overview of the hydrology of the Mekong basin. Mekong River Commission, Vientiane, 73 pp.

MRC (Mekong River Commission), 2017. Data and Information Services Portal. (http://portal.mrcmekong.org/index) (accessed 26 April 2017).

Mulder, T., Migeon, S., Savoye, B., Jouanneau, J.M., 2001. Twentieth century floods recorded in the deep Mediterranean sediments. Geology 29, 1011–1014. doi:10.1130/0091-7613(2001)029<1011:TCFRIT>2.0.CO;2

Mulder, T., Syvitski, J.P.M., 1995. Turbidity currents generated at river mouths during exceptional discharges to the world oceans. J. Geol. 103, 285–299. doi:10.1086/629747

Mulder, T., Syvitski, J.P.M., Migeon, S., Faugères, J.-C., Savoye, B., 2003. Marine hyperpycnal flows: initiation, behavior and related deposits. A review. Mar. Pet. Geol. 20, 861–882. doi:10.1016/j.marpetgeo.2003.01.003

Mulder, T., Zaragosi, S., Jouanneau, J.-M., Bellaiche, G., Guérinaud, S., Querneau, J., 2009. Deposits related to the failure of the Malpasset Dam in 1959. Mar. Geol. 260, 81–89. doi:10.1016/j.margeo.2009.02.002

Nayar, K.G., Sharqawy, M.H., Banchik, L.D., Lienhard, J.H.V., 2016. Thermophysical properties of seawater: A review and new correlations that include pressure dependence. Desalination, 390, 1-24. doi:10.1016/j.desal.2016.02.024

Neill, C.F., Allison, M.A., 2005. Subaqueous deltaic formation on the Atchafalaya Shelf, Louisiana. Mar. Geol. 214, 411–430. doi:10.1016/j.margeo.2004.11.002

Nguyen, A.D., Savenije, H.H., Pham, D.N., Tang, D.T., 2008. Using salt intrusion measurements to determine the freshwater discharge distribution over the branches of a multi-channel estuary: The Mekong Delta case. Est., Coast. and Shelf Sci. 77, 433–445.

Nguyen, V.L., Ta, T.K.O., Tateishi, M., 2000. Late Holocene depositional environments and coastal evolution of the Mekong River Delta, Southern Vietnam. J. Asian Earth Sci. 18, 427–439. doi:10.1016/S1367-9120(99)00076-0

Nittrouer, C.A, Kuehl, S.A, 1995. An introduction to the geological significance of sediment transport and accumulation on the Amazon continental shelf. Mar. Geol. 125, 177–192.

Nittrouer, C.A., DeMaster, D.J., 1996. The Amazon shelf setting: tropical, energetic, and influenced by a large river. Cont. Shelf Res. 16, 553–573.

Nittrouer, C.A., DeMaster, D.J., McKee, B.A., 1984. Fine-scale stratigraphy in proximal and distal deposits of sediment dispersal systems in the East China Sea. Mar. Geol. 61, 13–24.

Nittrouer, C.A., Kuehl, S.A., DeMaster, D.J., Kowsmann, R.O., 1986. The deltaic nature of Amazon shelf sedimentation. Geol. Soc. Am. Bull. 97, 444–458. doi:10.1130/0016-7606(1986)97<444:TDNOAS>2.0.CO;2

Nittrouer, C.A., Sternberg, R.W., Carpenter, R., Bennett, J.T., 1979. The use of Pb-210 geochronology as a sedimentological tool: Application to the Washington continental shelf. Mar. Geol. 31, 297–316. doi:10.1016/0025-3227(79)90039-2

NOAA (National Oceanic and Atmospheric Administration), 2016a. National Buoy Data Center. (http://www.ndbc.noaa.gov) (accessed 10.27.2016).

NOAA (National Oceanic and Atmospheric Administration), 2016b. NOAA WAVEWATCH III MMAB Operational Wave Models. (http://polar.ncep.noaa.gov/waves/index2.shtml) (accessed 20 Feb 2016).

NOAA (National Oceanic and Atmospheric Administration), 2017. National Buoy Data Center. (http://www.ndbc.noaa.gov) (accessed 01.27.2017).

Norris, R.D., Wilson, P.A., Blum, P., Fehr, A., Agnini, C., Bornemann, A., Boulila, S., Bown, P.R., Cournede, C., Friedrich, O., Ghosh, A.K., Hollis, C.J., Hull, P.M., Jo, K., Junium, C.K., Kaneko, M., Liebrand, D., Lippert, P.C., Liu, Z., Matsui, H., Moriya, K., Nishi, H., Opdyke, B.N., Penman, D., Romans, B., Scher, H.D., Sexton, P., Takagi, H., Turner, S.K., Whiteside, J.H., Yamaguchi, T., and Yamamoto, Y., 2014. Methods, in: Norris, R.D., Wilson, P.A., Blum, P., and the Expedition 342 Scientists, Proc. IODP, 342: College Station, TX (Integrated Ocean Drilling Program). doi:10.2204/iodp.proc.342.102.2014

Nowacki, D.J., Horner-Devine, A.R., Nash, J.D., Jay, D.A., 2012. Rapid sediment removal from the Columbia River plume near field. Cont. Shelf Res. 35, 16–28. doi:10.1016/

j.csr.2011.11.013

Nowacki, D.J., Ogston, A.S., Nittrouer, C.A., Fricke, A.T., Van, P.D.T., 2015. Sediment dynamics in the lower Mekong River: Transition from tidal river to estuary. J. Geophys. Res. Ocean. 120, 6363–6383. doi:10.1002/2015JC010754

Ogston, A.S., Sternberg, R.W., Nittrouer, C.A., Martin, D.P., Goñi, M.A., Crockett, J.S., 2008. Sediment delivery from the Fly River tidally dominated delta to the nearshore marine environment and the impact of El Niño. J. Geophys. Res. 113, 1–18. doi:10.1029/2006JF000669

Parsons, J.D., Bush, J.W.M., Syvitski, J.P.M., 2001. Hyperpycnal plume formation from riverine outflows with small sediment concentrations. Sedimentology 48, 465–478. doi:10.1046/j.1365-3091.2001.00384.x

Patruno, S., Hampson, G.J., Jackson, C.A.-L., 2015. Quantitative characterization of deltaic and subaqueous clinoforms. Earth-Science Rev. 142, 79–119. doi:10.1016/j.earscirev.2015.01.004

Paull, C.K., Ussler, W., Greene, H.G., Keaten, R., Mitts, P., Barry, J., 2003. Caught in the act: the 20 December 2001 gravity flow event in Monterey Canyon. Geo-Marine Lett. 22, 227–232. doi:10.1007/s00367-003-0117-2

Perry, G., Duffy, P., Miller, N., 1996. An extended data set of river discharges for validation of general circulation models. J. Geophys. Res. 101, 339–349.

Phan, L.K., van Thiel de Vries, J.S.M., Stive, M.J.F., 2015. Coastal Mangrove Squeeze in the Mekong Delta. Proceedings of the 36th IAHR World Congress, The Hague. doi:10.2112/JCOASTRES-D-14-00049.1

Piper, D.J.W., Normark, W.R., 2001. Sandy fans—from Amazon to Hueneme and beyond. Am. Assoc. Pet. Geol. Bull. 85, 1407–1438.

Piper, D.J.W., Normark, W.R., 2009. Processes that initiate turbidity currents and their influence on turbidites: A marine geology perspective. J. Sediment. Res. 79, 347–362. doi:10.2110/jsr.2009.046

Pirmez, C., Pratson, L.F., Steckler, M.S., 1998. Clinoform development by advection-

diffusion of suspended sediment: Modeling and comparison to natural systems. J. Geophys. Res. 103. doi:10.1029/98JB01516

Plink-Björklund, P., Steel, R.J., 2004. Initiation of turbidity currents: outcrop evidence for Eocene hyperpycnal flow turbidites. Sediment. Geol. 165, 29–52. doi:10.1016/j.sedgeo.2003.10.013

Prior, D.B., Bornhold, B.D., Wiseman, W.J., Lowe, D.R., 1987. Turbidity current activity in a British Columbia fjord. Science 237, 1330–1333.

Pritchard, D., Gladstone, C., 2009. Reversing buoyancy in turbidity currents: developing a hypothesis for flow transformation and for deposit facies and architecture. Mar. and Pet. Geol., 26, 1997–2010.

Puig, P., Ogston, A.S., Guillén, J., Fain, A.M.V., Palanques, A., 2007. Sediment transport processes from the topset to the foreset of a crenulated clinoform (Adriatic Sea). Cont. Shelf Res. 27, 452–474. doi:10.1016/j.csr.2006.11.005

Randle, T.J., Bountry, J.A., Ritchie, A., Wille, K., 2015. Large-scale dam removal on the Elwha River, Washington, USA: Erosion of reservoir sediment. Geomorph. 246, 709–728. doi:10.1016/j.geomorph.2014.12.045

Rhoads, D.C., Boesch, D.F., Zhican, T., Fengshan, X., Liqiang, H., Nilsen, K.J., 1985. Macrobenthos and sedimentary facies on the Changjiang delta platform and adjacent continental shelf, East China Sea. Cont. Shelf Res. 4, 189–213. doi:10.1016/0278-4343(85)90029-9

Rodolfo, K.S., 1969. Bathymetry and marine geology of the Andaman Bain, and tectonic implications for Southeast Asia. Geol. Soc. Am. Bull. 80, 1203-1230.

Ross, M.A., Mehta, A.J., 1989. On the mechanics of lutoclines and fluid mud. Journal of Coastal Research, sp5: High Concentration Cohesive Sediment Transport, 51–62. Coastal Education and Research Foundation.

Rouhnia, M., Strom, K., 2017. Sedimentation from buoyant muddy plumes in the presence of interface mixing: An experimental study. J. Geophys. Res. Ocean. 122, 2652–2670. doi:10.1002/2016JC012053.

Rubin, Z.K., Kondolf, G.M., Carling, P.A., 2014. Anticipated geomorphic impacts from Mekong basin dam construction. Int. J. River Basin Manag. 13, 105–121. doi:10.1080/15715124.2014.981193

Salahuddin, Lambiase, J.J., 2013. Sediment dynamics and depositional systems of the Mahakam Delta, Indonesia: Ongoing delta abandonment on a tide-dominated coast. J. Sediment. Res. 83, 503–521. doi:10.2110/jsr.2013.42

Schimanski, A., Stattegger, K., 2005. Deglacial and Holocene evolution of the Vietnam shelf: stratigraphy, sediments and sea-level change. Mar. Geol. 214, 315–387

Segall, M.P., Kuehl, S.A., 1992. Sedimentary processes on the Bengal continental shelf as revealed by clay-size mineralogy. Cont. Shelf Res. 12, 517–541.

Segall, M.P., Kuehl, S.A., 1994. Sedimentary structures on the Bengal shelf: a multi-scale approach to sedimentary fabric interpretation. Sediment. Geol. 93, 165–180. doi:10.1016/0037-0738(94)90003-5

Sequeiros, O.E., Naruse, H., Endo, N., Garcia, M.H., Parker, G., 2009. Experimental study on self-accelerating turbidity currents. J. Geophys. Res. Ocean. 114. doi:10.1029/2008JC005149

Sequeiros, O.E., Spinewine, B., Beaubouef, R.T., Sun, T., García, M.H., Parker, G., 2010. Characteristics of Velocity and Excess Density Profiles of Saline Underflows and Turbidity Currents Flowing over a Mobile Bed. J. Hydraul. Eng. 136, 412–433. doi:10.1061/(ASCE)HY.1943-7900.0000200

Sharqawy, M.H., Lienhard J.H.V, Zubair, S.M., 2010. Thermophysical properties of seawater: A review of existing correlations and data. Desalination and Water Treatment, 16, 354-380.

Shi, Z., Zhou, H.J., 2004. Controls on effective settling velocities of mud flocs in the Changjiang Estuary, China. Hydrol. Process. 18, 2877–2892. doi:10.1002/hyp.1500

Sommerfield, C.K., Nittrouer, C.A, 1999. Modern accumulation rates and a sediment budget for the Eel shelf: a flood-dominated depositional environment. Mar. Geol. 154, 227–241.

Sorensen, R.M., 1993. Basic wave mechanics for coastal and ocean engineers. John Wiley

and Sons, Inc., New York. 284 pp.

Soulsby, R.L., 1997. Dynamics of marine sands. HR Wallingford. Howbery Park, London 142 pp.

Stacey, M.W., Bowen, A.J., 1988. The vertical structure of density and turbidity currents: Theory and observations. J. Geophys. Res. 93, 3528–3542. doi:10.1029/JC093iC04p03528

Steel, E., Simms, A.R., Warrick, J., Yokoyama, Y., 2016. Highstand shelf fans: The role of buoyancy reversal in the deposition of a new type of shelf sand body. Bull. Geol. Soc. Am. 128, 1717–1724. doi:10.1130/B31438.1

Sternberg, R.W., 1972. Predicting initial motion and bedload transport of sediment particles in the shallow marine environment, in: Swift, D.J., Duane, D.B., Pilkey, O.H., Eds., Shelf Sediment Transport, Processes and Pattern. Dowden, Hutchison and Ross, Stroudsburg, PA, pp. 61–83.

Sternberg, R.W., Berhane, I., Ogston, A.S., 1999. Measurement of size and settling velocity of suspended aggregates on the northern California continental shelf. Mar. Geol. 154, 43–53. doi:10.1016/S0025-3227(98)00102-9

Sternberg, R.W., Cacchione, D.A., Paulso, B., Kineke, G.C., Drake, D.E., 1996. Observations of sediment transport on the Amazon subaqueous delta. Cont. Shelf Res. 16, 697–715. doi:10.1016/0278-4343(95)00045-3

Stevens, A.W., Gelfenbaum, G., Warrick, J.A., Miller, I.M., and Weiner, H.M., 2017a, Bathymetry, topography, and sediment grain-size data from the Elwha River delta, Washington, September 2013: U.S. Geological Survey data release, http://dx.doi.org/10.5066/F7SN0740.

Stevens, A.W., Gelfenbaum, G., Warrick, J.A., Miller, I.M., and Weiner, H.M., 2017b, Bathymetry, topography, and sediment grain-size data from the Elwha River delta, Washington, April and May 2014: U.S. Geological Survey data release, http://dx.doi.org/10.5066/F76T0JSP.

Stevenson, C.J., Peakall, J., 2010. Effects of topography on lofting gravity flows: Implications

for the deposition of deep-water massive sands. Mar. Pet. Geol. 27, 1366–1378. doi:10.1016/j.marpetgeo.2010.03.010

Swenson, J.B., Paola, C., Pratson, L., Voller, V.R., Murray, A.B., 2005. Fluvial and marine controls on combined subaerial and subaqueous delta progradation: Morphodynamic modeling of compound-clinoform development. J. Geophys. Res. 110, 1–16. doi:10.1029/2004JF000265

Syvitski, J.P., Skene, K.I., Nicholson, M.K., Morehead, M.D., 1998. PLUME1.1: deposition of sediment from a fluvial plume. Comput. Geosci. 24, 159–171. doi:10.1016/S0098-3004(97)00084-8

Syvitski, J.P.M., Peckham, S.D., Hilberman, R., Mulder, T., 2003. Predicting the terrestrial flux of sediment to the global ocean: A planetary perspective. Sediment. Geol. 162, 5–24. doi:10.1016/S0037-0738(03)00232-X

Ta, T.K.O., Nguyen, V.L., Tateishi, M., Kobayashi, I., Saito, Y., 2001. Sedimentary facies, diatom and foraminifer assemblages in a late Pleistocene-Holocene incised-valley sequence from the Mekong River Delta, Bentre Province, Southern Vietnam: the BT2 core. J. Asian Earth Sci. 20, 83–94. doi:10.1016/S1367-9120(01)00028-1

Ta, T.K.O., Nguyen, V.L., Tateishi, M., Kobayashi, I., Saito, Y., Nakamura, T., 2002. Sediment facies and Late Holocene progradation of the Mekong River Delta in Bentre Province, southern Vietnam: an example of evolution from a tide-dominated to a tide- and wave-dominated delta. Sediment. Geol. 152, 313–325. doi:10.1016/S0037-0738(02)00098-2

Takagi, H., Ty, T.V., Thao, N.D., Esteban, M., 2014. Ocean tides and the influence of sea-level rise on floods in urban areas of the Mekong Delta. J. Flood Risk Manag. 8, 292–300. doi:10.1111/jfr3.12094

Talling, P.J., Allin, J., Armitage, D.A., Arnott, R.W., Cartigny, M.J., Clare, M.A., Felletti, F., Covault, J.A., Girardclos, S., Hansen, E., Hill, P.R., Hiscott, R.N., Hogg, A.J., Hughes Clarke, J., Jobe, Z.R., Malgesini, G., Mozzato, A., 2015. Key Future directions for research on turbidity currents and their deposits. J. Sediment. Res. 85, 153–169.

doi:10.2110/jsr.2015.03

Tamura, T., Horaguchi, K., Saito, Y., Nguyen, V.L., Tateishi, M., Ta, T.K.O., Nanayama, F., Watanabe, K., 2010. Monsoon-influenced variations in morphology and sediment of a mesotidal beach on the Mekong River delta coast. Geomorphology 116, 11–23. doi:10.1016/j.geomorph.2009.10.003

Tamura, T., Saito, Y., Nguyen, V.L., Ta, T.K.O., Bateman, M.D., Matsumoto, D., Yamashita, S., 2012. Origin and evolution of interdistributary delta plains; insights from Mekong River delta. Geology 40, 303–306. doi:10.1130/G32717.1

Tamura, T., Saito, Y., Sieng, S., Ben, B., Kong, M., Sim, I., Choup, S., Akiba, F., 2009. Initiation of the Mekong River delta at 8 ka: evidence from the sedimentary succession in the Cambodian lowland. Quat. Sci. Rev. 28, 327–344. doi:10.1016/j.quascirev.2008.10.010

Torfs, H., Jiang, J., Mehta, A.J., 2001. Assessment of the erodibility of fine/coarse sediment mixtures, in: McAnally, W.H., Mehta, A.J., Eds., Coastal and Estuarine Sediment Processes. Vol. 3. Proceedings in Marine Science, 109–123. Elsevier.

Traykovski, P., Geyer, W.R., Irish, J.D., Lynch, J.F., 2000. The role of wave-induced density-driven fluid mud flows for cross-shelf transport on the Eel River continental shelf. Cont. Shelf Res. 20, 2113–2140. doi:10.1016/S0278-4343(00)00071-6

Traykovski, P., Wiberg, P.L., Geyer, W.R., 2007. Observations and modeling of wave-supported sediment gravity flows on the Po prodelta and comparison to prior observations from the Eel shelf. Cont. Shelf Res. 27, 375–399. doi:10.1016/j.csr.2005.07.008

Unverricht, D., Nguyen, T.C., Heinrich, C., Szczucinski, W., Lahajnar, N., Stattegger, K., 2014. Suspended sediment dynamics during the inter-monsoon season in the subaqueous Mekong Delta and adjacent shelf, southern Vietnam. J. Asian Earth Sci. 79, 509–519. doi:10.1016/j.jseaes.2012.10.008

Unverricht, D., Szczucinski, W., Stattegger, K., Jagodzinski, R., Le, X.T., Kwong, L.L.W., 2013. Modern sedimentation and morphology of the subaqueous Mekong Delta, Southern Vietnam. Glob. Planet. Change 110, 223–235. doi:10.1016/j.gloplacha.2012.12.009

USACE (United States Army Corps of Engineers), 1984. Shore protection manual. U.S.

Government Printing Office, Washington, D.C. Volumes 1 and 2.

USGS (United States Geological Survey), 2017. National Water Information System: U.S. Geological Survey database. (http://waterdata.usgs.gov/nwis) (accessed 04.10.17).

van Leussen, W., 1988. Aggregation of particles, settling velocity of mud flocs: A review, in: Physical Processes in Estuaries. pp. 347–403. doi:10.1007/978-3-642-73691-9-19

van Maren, D.S., Hoekstra, P., 2005. Dispersal of suspended sediments in the turbid and highly stratified Red River plume. Cont. Shelf Res. 25, 503–519. doi:10.1016/j.csr.2004.10.010

Wackerman, C., Hayden, A., Jonik, J., in press. Deriving spatial and temporal context for point measurements of suspended sediment concentration using remote sensing imagery in the Mekong Delta. Cont. Shelf Res.

Walling, D.E., 2008. The changing sediment load of the Mekong River. AMBIO A J. Hum. Environ. 37, 150–157.

Walsh, J.P., Nittrouer, C.A., 2009. Understanding fine-grained river-sediment dispersal on continental margins. Mar. Geol. 263, 34–45. doi:10.1016/j.margeo.2009.03.016

Walsh, J.P., Nittrouer, C.A., Palinkas, C.M., Ogston, A.S., Sternberg, R.W., Brunskill, G.J., 2004. Clinoform mechanics in the Gulf of Papua, New Guinea. Cont. Shelf Res. 24, 2487–2510. doi:10.1016/j.csr.2004.07.019

Warrick, J.A., Bountry, J.A., East, A.E., Magirl, C.S., Randle, T.J., Gelfenbaum, G., Ritchie, A.C., Pess, G.R., Leung, V., Duda, J.J., 2015. Large-scale dam removal on the Elwha River, Washington, USA: Source-to-sink sediment budget and synthesis. Gemorphology, 246, 729–750. doi:10.1016/j.geomorph.2015.01.010.

Warrick, J.A., Mertes, L.A.K., Washburn, L., Siegel, D.A., 2004. A conceptual model for river water and sediment dispersal in the Santa Barbara Channel, California. Cont. Shelf Res. 24, 2029–2043. doi:10.1016/j.csr.2004.07.010

Warrick, J.A., Stevens, A.W., 2011. A buoyant plume adjacent to a headland—Observations of the Elwha River plume. Cont. Shelf Res. 31, 85–97. doi:10.1016/j.csr.2010.11.007

Warrick, J.A., Xu, J., Noble, M.A., Lee, H.J., 2008. Rapid formation of hyperpycnal sed-

iment gravity currents offshore of a semi-arid California river. Cont. Shelf Res. 28, 991–1009. doi:10.1016/j.csr.2007.11.002

Webster, K.L., 2014. Sediment dispersal and accumulation in an insular sea: deltas of Puget Sound. PhD dissertation, University of Washington.

Wentworth, C.K., 1922. A scale of grade and class terms for clastic sediments. J. Geol. 30, 377–392.

Whitehouse, R., Soulsby, R., Roberts, W., Mitchener, H., 2000. Dynamics of Estuarine Muds. Thomas Telford Publishing, London. 210 pp.

Wiberg, P.L., Drake, D.E., Cacchione, D.A., 1994. Sediment resuspension and bed armoring during high bottom stress events on the northern California inner continental shelf: measurements and predictions. Cont. Shelf Res., 14, 1191–1219. doi:10.1016/0278-4343(94)90034-5

Wiberg, P.L., Sherwood, C.R., 2008. Calculating wave-generated bottom orbital velocities from surface-wave parameters. Comput. Geosci. 34, 1243–1262. doi:10.1016/j.cageo.2008.02.010

Wilson, C.A., Goodbred, S.L. Jr., 2015. Construction and maintenance of the Ganges-Brahmaputra-Meghna Delta: Linking process, morphology, and stratigraphy. Ann. Rev. Mar. Sci. 7, 67–88. doi:10.1146/annurev-marine-010213-135032

Winterwerp, J.C., 2002. On the flocculation and settling velocity of estuarine mud. Cont. Shelf Res. 22, 1339–1360. doi:10.1016/S0278-4343(02)00010-9

Winterwerp, J.C., van Kesteren, W.G.M., 2004. Introduction to the Physics of Cohesive Sediment Dynamics in the Marine Environment, in: Developments in Sedimentology, v.56, 559 pp., Elsevier.

Wolanski, E., Huan, N.N., Dao, L.T., Nhan, N.H., Thuy, N.N., 1996. Fine-sediment dynamics in the Mekong River estuary, Vietnam. Estuar. Coast. Shelf Sci. 43, 565–582. doi:10.1006/ecss.1996.0088

Wolanski, E., Nhan, N.H., Spagnol, S., 1998. Sediment dynamics during low flow conditions in the Mekong River Estuary, Vietnam. J. Coast. Res. 14, 472–482.

Wright, L., Wiseman, W., Yang, Z., 1990. Processes of marine dispersal and deposition of suspended silts off the modern mouth of the Huanghe (Yellow River). Cont. Shelf Res. 10, 1–40.

Wright, L.D., 1977. Sediment transport and deposition at river mouths: A synthesis. Geol. Soc. Am. Bull. 88, 857–868. doi:10.1130/0016-7606(1977)88<857

Wright, L.D., Nittrouer, C.A., 1995. Dispersal of river sediments in coastal seas: six contrasting cases. Estuaries 18, 494–508.

Wright, L.D., Yang, Z.S., Bornhold, B.D., Keller, G.H., Prior, D.B., Wiseman, W.J., 1986. Hyperpycnal plumes and plume fronts over the Huanghe (Yellow River) delta front. Geo-Marine Lett. 6, 97–105. doi:10.1007/BF02281645

Wu, J., Ametistova, L., Heron, M., Lemckert, C.J., Kalangi, P., 2006. Finite dispersal of a separative nepheloid plume by an internal hydraulic jump in a tropical mountainous river estuary. J. Geophys. Res. 111, C11004. doi:doi:10.1029/2005JC003404

Wyrtki, K., 1961. Physical oceanography of the Southeast Asian waters. NAGA report, Scientific Results of Marine Investigations of the South China Sea and the Gulf of Thailand 1959–1961. doi:10.1017/S0025315400054370

Xu, J.P., Noble, M.A., Rosenfeld, L.K., 2004. In-situ measurements of velocity structure within turbidity currents. Geophys. Res. Lett. 31. doi:10.1029/2004GL019718

Xue, Z., He, R., Liu, J.P., Warner, J.C., 2012. Modeling transport and deposition of the Mekong River sediment. Cont. Shelf Res. 37, 66–78. doi:10.1016/j.csr.2012.02.010

Xue, Z., Liu, J.P., DeMaster, D., Leithold, E.L., Wan, S., Ge, Q., Nguyen, V.L., Ta, T.K.O., 2014. Sedimentary processes on the Mekong subaqueous delta: Clay mineral and geochemical analysis. J. Asian Earth Sci. 79, 520–528. doi:10.1016/j.jseaes.2012.07.012

Xue, Z., Liu, J.P., DeMaster, D., Nguyen, L.V., Ta, T.K.O., 2010. Late Holocene Evolution of the Mekong Subaqueous Delta, Southern Vietnam. Mar. Geol. 269, 46–60. doi:10.1016/j.margeo.2009.12.005

Zu, T., Gan, J., Erofeeva, S.Y., 2008. Numerical study of the tide and tidal dynamics in the South China Sea. Deep. Res. Part I Oceanogr. Res. Pap. 55, 137–154.

Appendix A

DATA ANALYSES FOR THE MEKONG CLINOFORM STUDY

A.1 Evaluation of suspended-sediment concentrations

Suspended-sediment concentrations (SSCs), i.e., mass concentrations, were determined from in situ surface-water samples and laboratory calibration samples (see A.2). Sample volumes were measured and then samples were filtered through pre-dried and pre-desiccated 0.45 μm nitrocellulose membrane filters. Filters were then re-dried and re-weighed to determine to the change in mass. An ionizer was used during weighing to reduce errors related to static effects. Mass concentrations were determined by dividing the change in filter mass by the total volume filtered. Weights were adjusted according to the apparent concentrations of filtered distilled water calibration blanks.

A.2 Calibrations of OBS and ADCP backscatter data

Water-column OBS responses were converted to SSCs using a linear regression created from mass concentrations of filtered, in situ water samples (Figure A.1a). Boundary-layer tripod OBS responses were converted to SSC via lab calibrations. Sensors were submerged in mixtures of water and incrementally greater amounts of sediment. The mixtures were then subsampled and filtered to obtain SSC. The equation of the best-fit line between the instrument responses and SSC was used to convert the instrument data to mass concentrations (Figure A.1; see Downing, 2006). Four separate calibrations were made for the tripod OBSs mounted at 100 cm above bed (cmab) and 47/36 cmab (Sep14/Mar15), using four different kasten-core subsamples. These replicate calibrations were performed in order to evaluate the range of instrument responses to suspensions of varying grain-size compositions, because OBS responses have been shown to be sensitive to sediment grain-size (e.g., Downing, 2006).

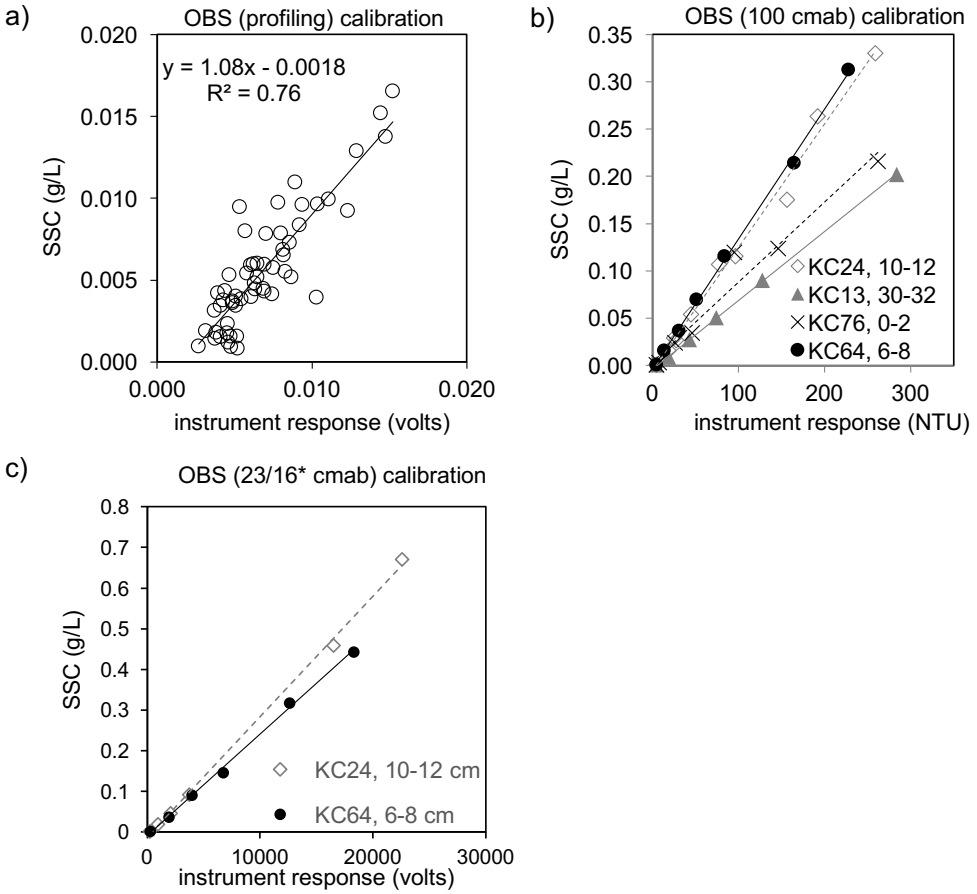

d)

Core	Interval	Equation	R^2	% sand	% c/m silt	% f/vf silt	% clay
KC24	10-12 cm	y = 0.0014x ¯ 0.0032 (100 cmab)	1.0	13	33	17	38
		y = (2.97e-5)x ¯ 0.013 (23/16 cmab)	1.0				
KC13	30-32 cm	y = 0.0008x + 0.0037 (100 cmab)	0.96	5	4	21	70
KC76	0-2 cm	y = 0.0013x ¯ 0.0054 (100 cmab)	0.99	43	10	11	37
KC64	6-8 cm	y = 0.0007x ¯ 0.0038 (100 cmab)	1.0	9	32	17	42
		y = (2.49e-5)x ¯ 0.0083 (23/16 cmab)	1.0				

Figure A.1: Profiling and tripod-mounted OBS calibration data. a) Field calibration for the profiling OBS; calibration samples were surface water samples collected with a Niskin bottle and filtered (see text). b) Six-point OBS lab calibration datasets for the 100 cmab RBR sensor, using mixtures of four different kasten-core sediment subsamples in fresh water. C) Six-point OBS lab calibration datasets for the 23/16 cmab OBS (*elevation was 23 cmab in Sep14 and 16 cmab in Mar15). c) Grain-size data and calibration equations associated with the sediment subsamples used for the OBS calibrations in (b) and (c). For the 100 cmab OBS, the equations from KC13 and KC64 were used to calculate a range of OBS values, because these represented the maximum and minimum calibrated instrument responses to suspensions of varying grain-size distributions. For the 23/16 cmab OBS, the equation from KC24 was used to calculate a maximum measured SSC for that sensor.

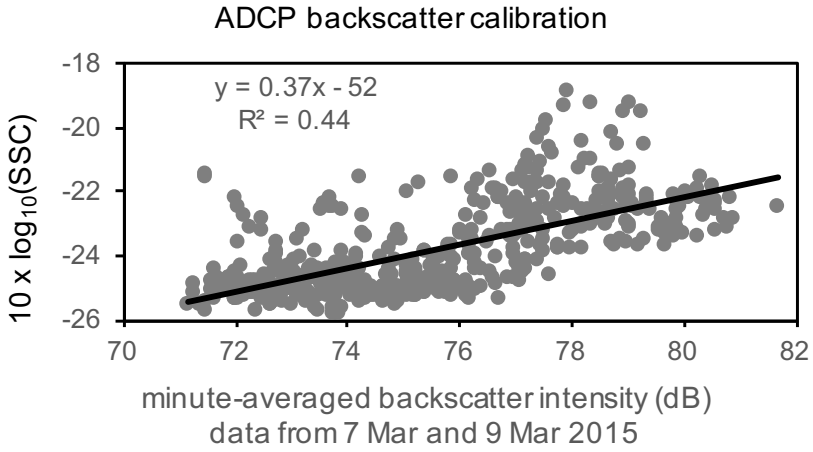

Figure A.2: Backscatter calibration data for the ship-mounted 600 kHz ADCP, from 7 Mar and 9 Mar 2015. SSC measurements were obtained from calibrated profiling OBS data collected every half hour while on each anchor station.

As expected, instrument responses were different for each sediment subsample, and four separate regression equations were obtained (Figure A.1). Responses were positively correlated with percent of coarse/medium silt. Thus, a range of SSC values was computed using the regression equations with maximum and minimum slope (Figure A.1, equations obtained from KC64 and KC13). Two calibrations were also made for the tripod OBS at 23/15 cmab (Sep14/Mar15) (Figure A.1).

Backscatter data from the downward-looking ADCP were corrected for beam spreading and sound absorption per the method in Deines, 1999. Binned, minute-averaged ADCP intensity data collected at anchor stations from both cruises were compared to binned SSC profile data; the latter were collected every ∼30 min. This comparison (Figure A.2) yielded the following calibration equation:

$$SSC = 10^{(0.1)(0.374dB-52.1)} \tag{A.1}$$

where dB is the corrected backscatter value in decibels (after Kim and Voulgaris, 2003).

A.3 Calculation of sediment fluxes

Boundary-layer sediment fluxes were calculated by multiplying high-resolution ADCP current data at a single elevation and converted OBS data. For Sep14, current and OBS measurements from 23 cmab were used, and for Mar15, current and OBS measurements 15 cmab were used as shown in Figure 4.4 and Figure 4.5. The resulting fluxes allow for comparison of transport directions between seasons and relative magnitudes within a given season.

A.4 Grain-size analyses

Sediment subsamples from kasten cores were processed for sand/silt/clay fractions and whole-phi size distributions of the mud (silt plus clay) fraction. Samples were first separated into sand and mud fractions by sieving through a 4-ϕ (63-μm) sieve using a 0.05% NaO_3P (dispersant) solution. Mud fractions were then sonicated. (Both dispersion and sonication facilitate floc break-up, to ensure accurate measurements of disaggregated sizes). Mud was processed in a Micromeritics Sedigraph x-ray particle sizer to 10 ϕ (1 μm), dried, and weighed. Sand fractions were dried and weighed. Clay fractions were determined from combined Sedigraph data and sand weights, and used in accumulation-rate analyses. Sand fractions from select subsamples were processed in a settling column to determine characteristic sand sizes.

A.5 Apparent accumulation rate analyses

Apparent linear sediment accumulation rates (SARs) were determined for a subset of cores following a method similar to that given in Nittrouer et al. (1979). Out of 32 cores collected in this study, 21 were processed for ^{210}Pb activities at the University of Washington sediment lab, and 21 were processed for ^{210}Pb activities at the North Carolina State University sediment lab. The 10 cores that were processed by both labs were used for comparison and validation of SARs. Further details are available in DeMaster et al. (in press).

Sediments were spiked with a 1-ml solution of ^{209}Po diluted in HCl, and then digested

in HNO_3 and HCl. Digested samples were centrifuged, and the isotopes were electroplated for 22–24 h from the supernatant onto silver planchets. Planchets were counted for at least 24 hours in alpha detectors. Total ^{210}Pb activities were determined from the ratio of ^{209}Po to ^{210}Pb after correcting for decay of the spike and the sample since time of manufacture/collection, respectively, per the standard decay equation:

$$A(t) = A_0 e^{-\lambda t} \tag{A.2}$$

Excess activities were calculated by subtracting an assumed supported level of 0.8 dpm/g from the total activities. This value represented the 2nd percentile of measured total activities from 378 core subsamples collected in this study, i.e., 98% of measured values were >0.8 dpm/g. SAR (or S) was then determined from the region of radioactive decay according to the equation:

$$S = -\lambda \times m = \lambda \frac{z_0 - z}{ln(\frac{A_0}{A_z})} \tag{A.3}$$

where λ is the decay constant of the ^{210}Pb radionuclide (0.0311 yr^{-1}) and m is the slope of the best-fit line between A_0, the excess activity at depth z_0 (the base of the surface mixed layer), and A_z, the excess activity at depth z, the lower limit for the region of radioactive decay (see McKee et al., 1983). This model assumes steady-state deposition within the region of radioactive decay, and also assumes constant supported ^{210}Pb activity.

The effects of varying grain size on apparent SARs were evaluated by re-computing SARs using clay-normalized activities, i.e., dpm/g_{clay} instead of dpm/$g_{sediment}$ (see Figure A.3 and Figure A.1). These activities were calculated by dividing each excess activity value by the clay fraction of the subsample. The apparent clay-normalized sediment accumulation rates, or SARc, were ∼18% greater than the un-normalized values (Figure A.4).

Dry bulk densities were computed for each subsample presented in Figure A.3 per the following equations (see Blum, 1997 for A.4 through A.8):

$$M_{pw} = \frac{M_b - M_d}{1 - s*} \tag{A.4}$$

$$M_s = M_b - M_{pw} \tag{A.5}$$

$$V_{pw} = \frac{M_{pw}}{\rho_{pw}} \tag{A.6}$$

$$M_{salt} = M_{pw} - (M_b - M_d) \tag{A.7}$$

$$V_{salt} = \frac{M_{salt}}{\rho_{salt}} \tag{A.8}$$

$$V_s = \frac{M_s}{\rho_s} \tag{A.9}$$

$$V_B = V_s + V_{salt} + V_{pw} \tag{A.10}$$

$$\rho_{db} = \frac{M_s}{V_b} \tag{A.11}$$

where M, V, and ρ denote mass, volume, and density, respectively; subscripts b, d, pw, and s denote bulk, dry, porewater, and solids, respectively; and $s*$ represents the salt fraction. Based on measured salinities of ∼33 psu, temperatures of 27-29°C, and a depth of 15 m, ρ_{pw} was assumed to be 1.021 g/cm^3, and 0.033 was used as the salt fraction. Constant values of 2.65 g/cm^3 and 2.20 g/cm^3 were assumed for ρ_s and ρ_{salt}, respectively.

Mass accumulation rates (MARs) were computed by two methods. First, MARs were computed according to the following equation (e.g., Norris et al., 2014):

$$MAR = \overline{\rho_{db}} S \tag{A.12}$$

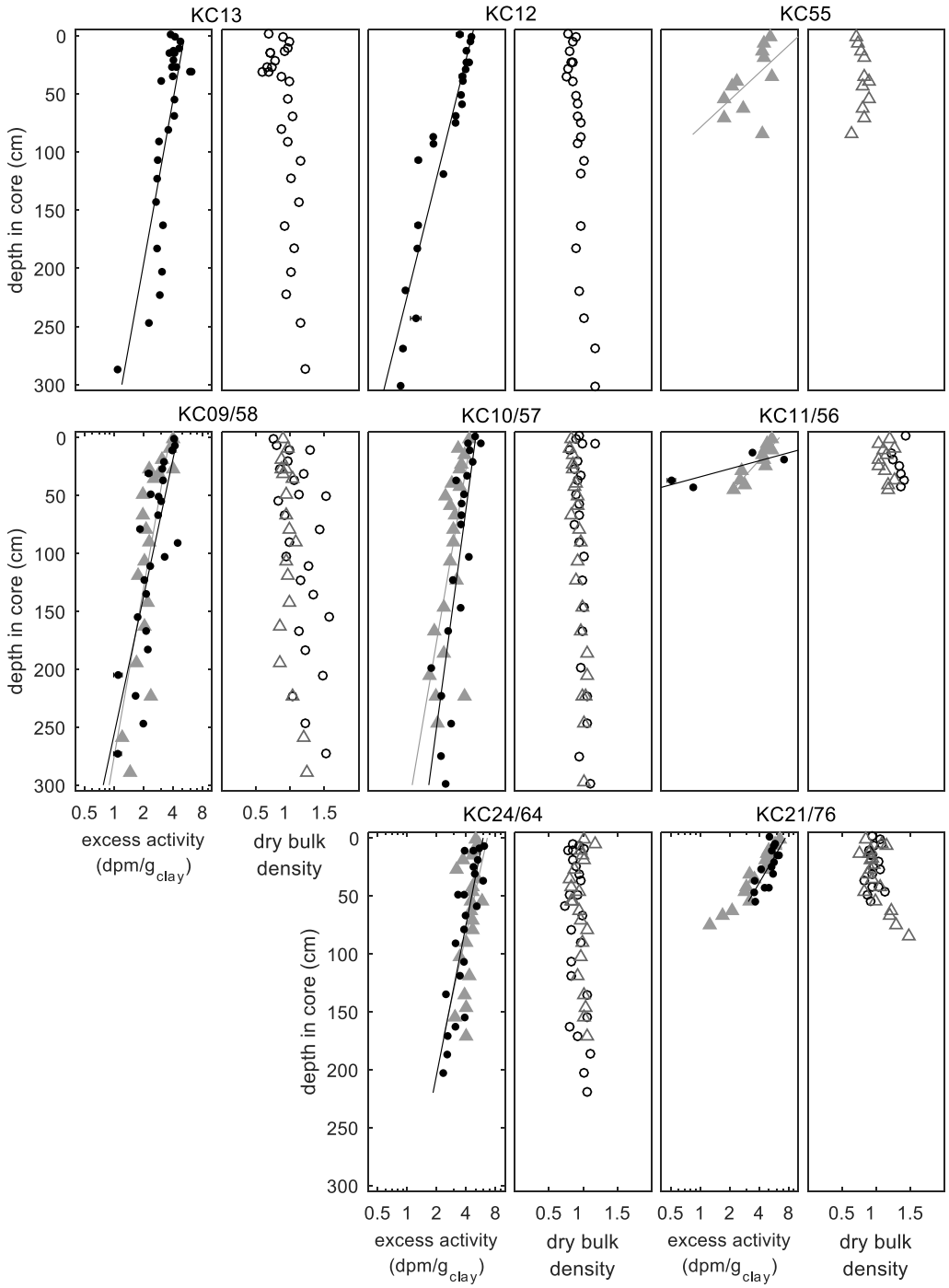

Figure A.3: Clay-normalized excess activities and dry bulk densities for cores. Cores collected in Sep14 are shown as black circles (filled, excess activity; open, dry bulk density) and are denoted by KC numbers up to KC24. Cores collected in Mar15 are shown as gray triangles (filled, excess activity; open, dry bulk density). Regression lines used for SAR (and MAR) calculations are shown.

where $\overline{\rho_{db}}$ is the mean dry bulk density for the entire core and S is SAR (see Figure A.3 for down-core profiles of ρ_{db}). Values are denoted as MAR_1 in Figure A.1. Second, MARs were computed according to equation A.3, but using cumulative mass (in units of $\mathrm{g/cm^2}$) instead of depths for z and z_0 (e.g., Sommerfield and Nittrouer, 1999). Cumulative masses were calculated by multiplying the bulk density of a given subsample by the thickness of sediment between that subsample and the next. The resulting MARs are denoted as MAR_2 (Figure A.1). Clay-normalized MAR_1 and MAR_2 were also calculated, in the same fashion as SARc (Figure A.1). MAR_2 values are reported in the main text of the paper. Detailed down-core plots of clay-normalized excess ^{210}Pb activity, ρ_{db}, and sand/silt/clay fractions are given in Figure A.5.

Table A.1: Accumulation rate data for 14 cores highlighted in this study. (Data for 18 additional cores collected in Sep14/Mar15 are presented in DeMaster et al., in press.) Locations are as follows: UF = upper foreset; LF = lower foreset; BS = bottomset. Value ρ_{d} is the mean dry bulk density for each core from all intervals shown in Figure A.3. SAR is the apparent sediment accumulation rate. R^2 is the regression coefficient of the best-fit line used to determine SAR. MAR is the mass accumulation rate (= SAR x ρ_{d}). SARc and MARc are clay-normalized values.

				Apparent AR			Apparent clay-normalized AR		
Core	Loc	Water depth (m)	ρ_{db} ($\mathrm{g/cm^3}$)	SAR (cm/yr)	$\mathrm{MAR_1}$ ($\mathrm{g/cm^2/yr}$)	$\mathrm{MAR_2}$ ($\mathrm{g/cm^2/yr}$)	SARc (cm/yr)	$\mathrm{MARc_1}$ ($\mathrm{g/cm^2/yr}$)	$\mathrm{MARc_2}$ ($\mathrm{g/cm^2/yr}$)
KC13	UF	6.0	0.91	4.1	3.7	4.0	8.0	7.3	7.8
KC12	LF	10.0	0.92	4.2	3.8	3.9	4.6	4.2	4.3
KC55	LF/BS	17.0	0.79	1.7	1.3	1.4	1.9	1.5	1.5
KC09	UF	7.0	1.14	4.3	4.9	4.8	5.3	6.1	6.2
KC58	UF	10.0	0.98	5.3	5.2	5.4	6.3	6.1	6.8
KC10	LF	12.7	0.97	7.9	7.6	7.9	8.1	7.9	8.0
KC57	LF	14.2	0.93	5.5	5.1	6.7	8.2	7.6	7.7
KC11	BS	19.8	1.34	0.47	0.63	0.59	0.38	0.51	0.50
KC56	BS	21.2	1.14	1.1	1.3	1.2	1.3	1.4	1.4
KC24	LF	18.3	0.92	4.5	4.1	4.2	5.9	5.4	5.5
KC64	LF	18.0	0.97	3.3	3.2	3.4	4.9	4.7	4.7
KC21	LF/BS	20.0	0.97	1.7	1.6	1.5	2.2	2.1	2.2
KC76	LF/BS	21.0	1.01	1.0	1.0	1.1	1.5	1.5	1.5

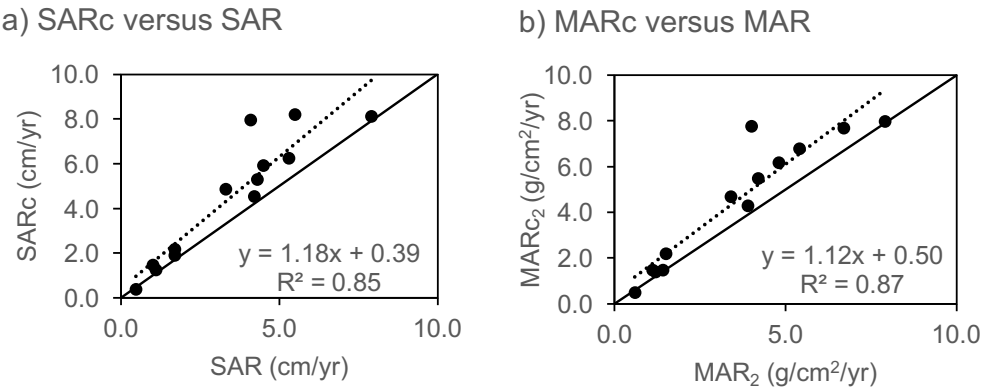

Figure A.4: Relationships between accumulation rates and clay-normalized accumulation rates. a) SAR_c versus SAR. b) MAR_{c2} versus MAR_2 (see Figure A.1). Clay-normalized accumulation rates were generally greater than non-clay-normalized rates. Bold lines are 1:1 lines.

A.6 Shear velocity modeling for the Mekong and seven other deltas

Monthly wave climatologies for the Mekong (Figure A.5) and seven other fluvial dispersal systems were obtained from the NOAA WAVEWATCH III (NWW3) global half-minute grid model (NOAA, 2016b) for a 10-yr period from Jul 2005 to Jun 2015. Mean annual significant wave heights ($\overline{H_{sig}}$) were extrapolated from model output at a single water depth to a range of water depths using linear wave theory for transitional waves (Sorensen et al., 1993; USACE, 1984). Mean annual wave-orbital velocities ($\overline{u_{br}}$) were then calculated from $\overline{H_{sig}}$ and wave period ($\overline{T}$) using the method of Wiberg and Sherwood (2008) with the default wave spectrum. The 10-yr time series of H_{sig}, T, and u_{br} for the Mekong are shown in Figure A.5.

For the Mekong Delta, tidal currents were modeled for the same 10-y time span and depth range as the wave climatology. Second-order polynomial curves were applied to anchor-station tidal-current measurements (at 0.51 meters above bed) and the Dinh An water level curve to obtain times-series of predicted currents. Currents at a range of clinoform depths were then interpolated from these three anchor-station locations using an additional polynomial best-fit curve.

Mean wave, current, and total shear velocities ($\overline{u_*}$, $\overline{u_{*c}}$, and $\overline{u_{*w}}$) were modeled for a

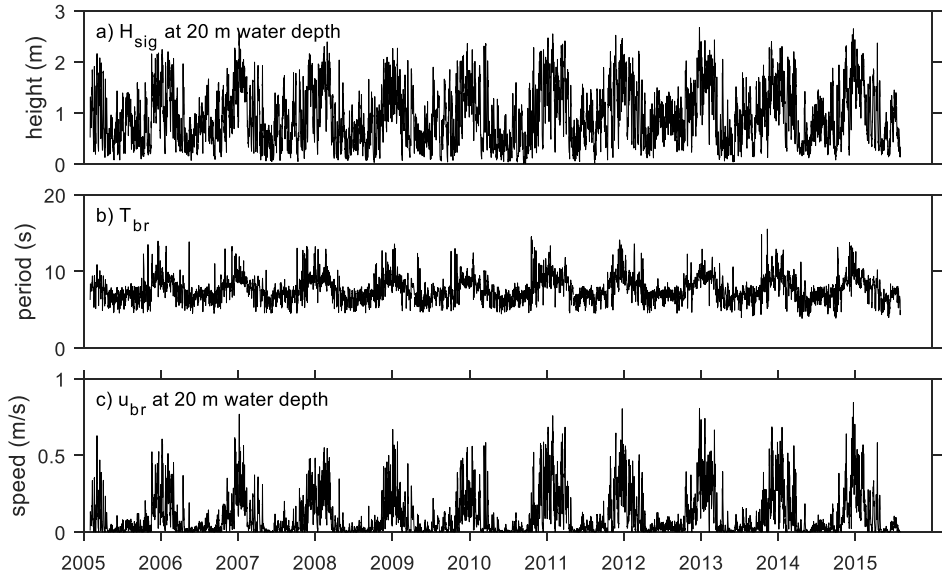

Figure A.5: Wave parameters for the Mekong extrapolated from NWW3. Ten-year time-series of modeled a) significant wave height (H_{sig}) at 20 m water depth, b) wave period (T), and c) wave-orbital velocity (u_{br}) at 20 m water depth based on NWW3 model output (see text).

range of water depths offshore of the Song Hau by inputting modeled current speeds (above), modeled $\overline{u_{br}}$ (derived from NWW3), and a Nikuradse bed roughness (k_N) into the Madsen (1994) wave-current interaction model. For this study, k_N = 0.014 mm, following $k_N = 2.5d_{50}$ (where d_{50} is the mean grain-size of the seabed; see Whitehouse et al., 2000), and d_{50} = 0.0057 mm (or 7.46 ϕ), the mean grain-size of surface samples from upper foreset (KC09, KC58) and lower foreset (KC10, KC57, KC24, KC64) cores presented in this study.

Mean wave shear velocities ($\overline{u_{*w}}$) in the absence of currents were also modeled at a range of water depths for the Mekong River delta and six other deltas: Atchafalaya River, Amazon River, Ayeyarwady River, Ganges-Brahmaputra River, Gulf of Papua/Fly River, and Yangtze River. The $\overline{u_{br}}$ extrapolated from NWW3 were evaluated using a wave friction factor. Because k_N varies among systems and at various depths, a small bed roughness of k_N = 0.0001 m was assumed to emulate a relatively smooth bed.